Permanent deactivation of boron-oxygen-related recombination centres in crystalline silicon

Von der Fakultät für Mathematik und Physik

der Gottfried Wilhelm Leibniz Universität Hannover

zur Erlangung des Grades

Doktor der Naturwissenschaften

Dr. rer. nat.

genehmigte Dissertation

von

Dipl.-Phys. Dominic Christof Walter

geboren am 29.12.1983 in Freiburg im Breisgau

Dezember 2016

Referent: Prof. Dr. Jan Schmidt
Korreferenten: Prof. Dr. Herbert Pfnür, Prof. Dr. Daniel Macdonald
Tag der Promotion: 05.12.2016

"I can live with doubt and uncertainty and not knowing. I think it is much more interesting to live not knowing than to have answers that might be wrong."

Richard P. Feynman (1918-1988)

Kurzzusammenfassung

In dieser Arbeit werden Bor- und Sauerstoff-korrelierte Defektzentren (BO-Defekte) in sauerstoffreichem, bordotiertem Silicium untersucht, das nach dem Czochralski-Verfahren hergestellt wurde. Im Fokus stehen die Bildung und die Deaktivierung der Defekte.
Es zeigt sich, dass die maximale Defektkonzentration weder von den Kristallwachstumsbedingungen noch von den vorherrschenden Punktdefekten (Leerstellen / Eigenzwischengitteratome) innerhalb des Siliciums abhängt. Stattdessen ist die Kühlkurve nach dem letzten Hochtemperaturschritt für die Defektkonzentration von entscheidender Bedeutung. Temperaturbehandlungen zwischen 200 °C und 300 °C führen zu einer Änderung der maximalen Defektkonzentration bis zu einem temperaturabhängigen Sättigungswert. Unter der Annahme einer mobilen Spezies im Volumen des Siliciums kann dieser Effekt als eine Ausgleichsreaktion aufgefasst werden. Dabei kann die Spezies sich an zwei unterschiedliche Senken anlagern. Mit einer Senke bildet sie den rekombinationsaktiven BO-Defekt. Die andere Senke zeigt nur sehr schwache Rekombinationseigenschaften.
Zusätzlich wurden in dieser Arbeit Einflussgrößen auf den Deaktivierungsprozess untersucht. Auch hier zeigt sich, dass der letzte Hochtemperaturschritt entscheidend für die Deaktivierungskinetik ist: Es wurde ein linearer Zusammenhang zwischen der Abkühlrate bei 600 °C und der Deaktivierungsrate beobachtet. Der Einfluss von Wasserstoff auf die Deaktivierungskinetik ist hingegen nicht signifikant. Diese Beobachtungen können innerhalb des oben erwähnten Modells einer mobilen Spezies mit zwei Senken so erklärt werden, dass sich der rekombinationsaktive BO-Defekt bei erhöhter Temperatur in Gegenwart von freien Ladungsträgern aufspaltet. Die freiwerdende mobile Spezies lagert sich dann an die nicht-rekombinationsaktive Senke an. Wird nun eine schnelle Abkühlrate mit einer Deaktivierungstemperatur von 230 °C und einer Beleuchtungsintensität von knapp 250 mW/cm^2 kombiniert, so läuft der gesamte Deaktivierungsprozess innerhalb von 10 Sekunden ab, was die industrielle Relevanz unterstreicht.
Lebensdaueruntersuchungen an verschiedenen Materialien nach Deaktivierung des BO-Defekts lieferten im Vergleich zu früheren Untersuchungen deutlich höhere Lebensdauern. Daher wurde eine Parametrisierung dieser Lebensdauern abhängig von der Dotierkonzentration und des Injektionsniveaus durchgeführt. Unter Berücksichtigung der neuen Parametrisierung zeigen 2D-Solarzellsimulationen, dass Wirkungsgrade von bis zu 23.4% mit der heutigen Prozesstechnologie für passivierte Emitter- und Rückseiten (PERC) Solarzellen mit selektivem Emitter möglich sind.
Bei Stabilitätsuntersuchungen zeigte sich, dass nach Deaktivierung des Defektkomplexes auch nach anschließender Beleuchtung für 1000 h bei Raumtemperatur, Lebensdauern im Bereich von 1 ms auf 1 Ω cm-Material möglich sind. Bauelementsimulationen bestätigen, dass diese geringe Degradation den Wirkungsgrad heutiger PERC-Zellen nicht beeinflusst.

Abstract

This work investigates boron-oxygen-related (BO) defect centres in oxygen-rich, boron-doped Czochralski-grown silicon with a focus on its formation and deactivation.
To identify the influence of different growth conditions, the formation of the BO defect is studied on various crystals. No influence of the growth conditions and the predominant point defect type (vacancies/self-interstitials) on the defect concentration is found. However, the defect concentration depends on the cooling curve after the last high-temperature step. It is shown that a prolonged annealing at temperatures between 200 °C and 300 °C changes the maximum defect concentration up to a temperature dependent saturation value. This observation is explained within the framework of a recent defect model via an equilibration process. It is assumed that a mobile species in the silicon bulk can bind to two different sinks. With one of the sinks the recombination-active BO defect is formed. The other sink shows only negligible recombination properties.
In this work, different parameters that influence the deactivation process are studied. Again, the last high-temperature treatment is proven to be of utmost importance for the deactivation kinetics. The cooling rate at 600 °C determines the deactivation rate constant. At this temperature, a linear correlation between the recovery rate constant and the cooling rate is observed for various materials. This can be explained within the same defect model assuming that under deactivation conditions the defect complex dissociates and the remaining mobile species is captured by the non-recombination-active sink. Hence, the overall defect concentration is reduced over the course of the deactivation process and the carrier lifetime increases. Investigations regarding the necessity of hydrogen for the deactivation process revealed no direct impact of hydrogen. Combining a fast sample cooling with a recovery temperature of 230 °C and a light intensity of almost 250 mW/cm^2, the deactivation process can proceed in a time frame of 10 s, which makes it industrially feasible.
After deactivating the BO complex in different materials, lifetimes significantly exceeding previous results were obtained. Hence, a lifetime parameterization depending on the doping concentration and the injection level was performed. Implementing these lifetimes into 2D solar cell simulations, it is shown that a stable conversion efficiency of passivated emitter and rear cells (PERC) with selective emitter reaching 23.4% is achievable with today's state-of-the-art process technologies.
The stability of the lifetime after deactivation of the BO complex was tested. At room temperature the lifetime degrades under illumination only marginally over the course of 1000 h. After this time span, lifetimes in the range of 1 ms were achieved on 1 Ω cm material. Device simulations revealed that this minor degradation has no impact on today's PERC solar cell performance.

Schlagworte:
Bor-Sauerstoff-korrelierte Defektzentren, Deaktivierung, Ladungsträgerlebensdauer
Keywords:
boron-oxygen-related defect centres, deactivation, carrier lifetime

Contents

Chapter 1

Introduction

Photovoltaics (PV) is a fast growing market. Between 2000 and 2015 the worldwide compound annual growth rate (CAGR) of PV installations was 41%, reaching a cumulative worldwide installed PV capacity of 242 GWp in 2015, according to the Fraunhofer ISE: Photovoltaics Report [1]. In the same year, silicon-wafer-based PV technology accounted for 93% of the total PV production [1]. Because of the predominant fraction of Si-PV technology and as, additionally, the solar cell efficiencies in production are far below the maximum efficiency of 29% [2], further improvements in this sector have a great impact. Over the last years, Si-PV technology developed rapidly with regard to device fabrication, i.e. improving individual processing steps like metallization or surface passivation of the silicon solar cell, and, hence, the quality of the silicon base material gained importance.

The demand for high-quality wafer material is presumably more easily met with mono-crystalline silicon than with multi-crystalline silicon, as it features less crystallographic defects and typically less metallic impurities. However, there is also one distinct drawback. For economical reasons, mono-crystalline silicon is typically grown via the Czochralski process (Cz-Si). A characteristic of this process is the high concentration of oxygen which is incorporated into the crystal during the growth. For microelectronic applications, where only the surface-near region of the wafer is used, the high oxygen concentration is beneficial. For PV applications, which require a high quality of the entire bulk, however, the high oxygen concentration can be detrimental. For example, when boron is used as dopant, the bulk material quality, characterized by the carrier lifetime, can be limited by the formation of a defect complex which forms in the silicon in the presence of boron and oxygen. The detrimental properties of this boron-oxygen-related defect complex were first observed more than 40 years ago by Fischer and Pschunder [3]. They observed a decrease in the output power of a silicon solar cell upon illumination at room temperature. In the same study, they could attribute the power decrease to a degradation of the bulk lifetime. For more than 30 years, this property of the BO defect limited the bulk lifetime in B-doped Cz-Si. However, in 2006, Herguth et al. [4] observed that the performance of such a solar cell can be permanently recovered into its initial state, if the cell is exposed to illumination at elevated temperature. Again, this is due to an increase of the bulk lifetime.

In this thesis, the BO defect formation as well as its permanent deactivation, which is accompanied by the permanent recovery of the lifetime, is investigated:

Chapter 2 presents two crystallization techniques to grow mono-crystalline silicon. As real crystals deviate from the ideal crystal structure, the chapter focusses on common defects, such as intrinsic point defects, oxygen-related defects and boron-oxygen-related (BO) defects. A review of published work on the subject of BO-related defects is given. The chapter concludes with a discussion of three different BO defect models.

In Chapter 3, a short introduction to the carrier lifetime in crystalline silicon and the related recombination processes is given. In the second part of this chapter, two lifetime measurement techniques which are mainly used within this thesis are presented, first a photoconductance-based technique and second a technique which combines photoconductance and photoluminescence measurements.

In Chapter 4, the defect formation of the BO defect is investigated in detail. In the first part, the influence of the crystal growth conditions is studied on three differently grown Cz crystals. Apart form differences along the crystal axis, i.e. seed end, centre and tail end, also the lateral differences over the dimension of a wafer are studied. In the second part, the equilibrium of the defect concentration at a defined temperature is examined. The equilibrium is reached upon annealing the sample at intermediate temperatures between 200 °C and 300 °C for several hours. The chapter concludes with an investigation of lifetime limitations in oxygen-rich, phosphorus-doped silicon, which does not suffer from the BO defect. Nevertheless, oxygen and its ability to form precipitates can strongly influence the lifetime.

Chapter 5 is divided into three different subsections related to the permanent deactivation of the BO defect. The first subsection focuses on the deactivation kinetics with regard to the influence of rapid thermal annealing, the recovery temperature, and the illumination intensity during recovery. Finally, all these findings are combined to realize a very fast, industrially feasible deactivation process. In the second subsection, the impact of hydrogen, introduced during sample processing, on the deactivation process is investigated in a series of different experiments. The third part deals with achievable lifetimes after a successful deactivation of the BO defect. A parameterization of the lifetime depending on the doping concentration and the injection density is presented. Additionally, the influence on the performance of today's state-of-the-art silicon solar cells is analysed by 2D device simulations.

In Chapter 6, the stability of the lifetime after deactivation of the BO defect is studied. First, the stability at room temperature and at elevated temperature is tested on lifetime samples. In particular, the influence of the recovery temperature, the rapid thermal annealing, the surface passivation type, and the base material are studied. The measured lifetimes are then inserted into a device simulation to evaluate the impact on solar cell level. Additionally, the stability of a real solar cell is tested.

In Chapter 7, the results of this thesis are summarized.

Chapter 2

Boron- and oxygen-related defects in crystalline silicon

Within the microelectronics industry, very highly purified silicon wafers are the most widely used starting point for the manufacturing of electronic devices. Unfortunately, silicon is not found as a pure element or a single crystal in the Earth's crust, but exists in the form of silicon dioxide and other silicates. Therefore, an intensive refining is required for the fabrication of high purity-silicon.
The so-called metallurgical silicon is commercially prepared within an electric arc furnace and is at least 98 % pure. However, for microelectronic applications much higher purities are needed. Traditionally, this purification is performed by applying the Siemens process. This process includes the transformation of the silicon into a gaseous phase of trichlorosilane which is followed by a CVD (chemical vapour deposition) process onto a high purity silicon seed rod. The silicon produced via this process may feature a purity of up to 99.999999999 % (11N) which makes it suitable for microelectronic applications.

In another processing step, a silicon single crystal is grown from the polysilicon rod, obtained from the Siemens process. Two different methods, the float-zone (FZ) as well as the Czochralski (Cz) growth methods, exist which allow the fabrication of large single crystals. In the following section, these two growth methods will be briefly discussed. Additionally, common defects which are related to oxygen and boron will be summarized.

2.1 Crystallization techniques

2.1.1 Float-zone silicon

The float-zone (FZ) crystal growth method is based on the zone-melting principle [5]. To grow a single crystal, a polysilicon rod, obtained from the Siemens process, is mounted vertically into a growth chamber which holds a vacuum if an un-doped crystal is grown or an inert gas atmosphere with an admixture of doping gases such as phosphine (PH_3) or diborane (B_2H_6) for n- or p-type doping, respectively. A needle-eye coil is used to melt a narrow zone of the crystal which is moved along the rod. During the process, the molten silicon solidifies into a single crystal with the predefined crystal orientation of the bottom-seed crystal. Unlike the Czochralski growth method, the molten silicon has no contact to other substances apart from the ambient gas, hence, FZ silicon can achieve a much higher purity than Cz silicon. Especially the oxygen concentration is with values in the range of 10^{16} atoms/cm^3 orders of magnitude smaller than in Cz silicon. Due to the lack of oxygen, the application of FZ-Si in microelectronic integrated-circuit (IC) fabrication is limited.

Compared to IC fabrication, in photovoltaic applications a high material quality of the bulk silicon wafer is necessary to obtain high conversion efficiencies of the finished device. However, higher costs and smaller capacity of FZ-Si in production lead to the fact that FZ-Si wafers are typically only used in laboratory devices and less commonly in commercial applications. However, the high material quality of FZ-Si allows to use it as ideal substrate for the analysis of dielectric layers deposited onto the material to passivate the surfaces. In this thesis, FZ-Si is mainly used for this purpose.

2.1.2 Czochralski-silicon

Czochralski-silicon (Cz-Si) is named after the Polish chemist Jan Czochralski (1885-1953) who, accidentally observed (1918) [6] that a single crystal can be grown from the liquid phase of a material by introducing a seed crystal to the surface and slowly pulling the crystal from the melt. In 1950, this pull-from-melt method was first applied by Teal and Little [7] to grow a germanium single crystal. Today, over 95% of all silicon single crystals are grown using this technique [8], as the resulting dislocation-free crystal fulfils the strict requirements of the microelectronic industry regarding the extremely low impurity concentrations. An even more important reason for using Cz-Si in microelectronics is the very high oxygen concentration. During device processing the ability to form oxygen precipitates and to generate lattice defects can be used in a controlled manner for impurity gettering. Moreover, the high oxygen concentration additionally strengthens the material which prevents breakage during high temperature processing.

2.1.2.1 Czochralski-silicon growth

Figure 2.1 shows a schematic of a modern Cz-Si pulling setup. In the centre, the quartz glass crucible is shown, containing silicon nuggets obtained from the Siemens process. The crucible is surrounded by a resistive heater. The crucible and the seed crystal are mounted independently so that both can be rotated in opposite directions. The entire growing chamber is filled with an inert gas atmosphere. The total dwell time and the temperatures the crystal experience in the grower constitute to the thermal history of the crystal. The thermal history has a strong impact on the state of the crystal

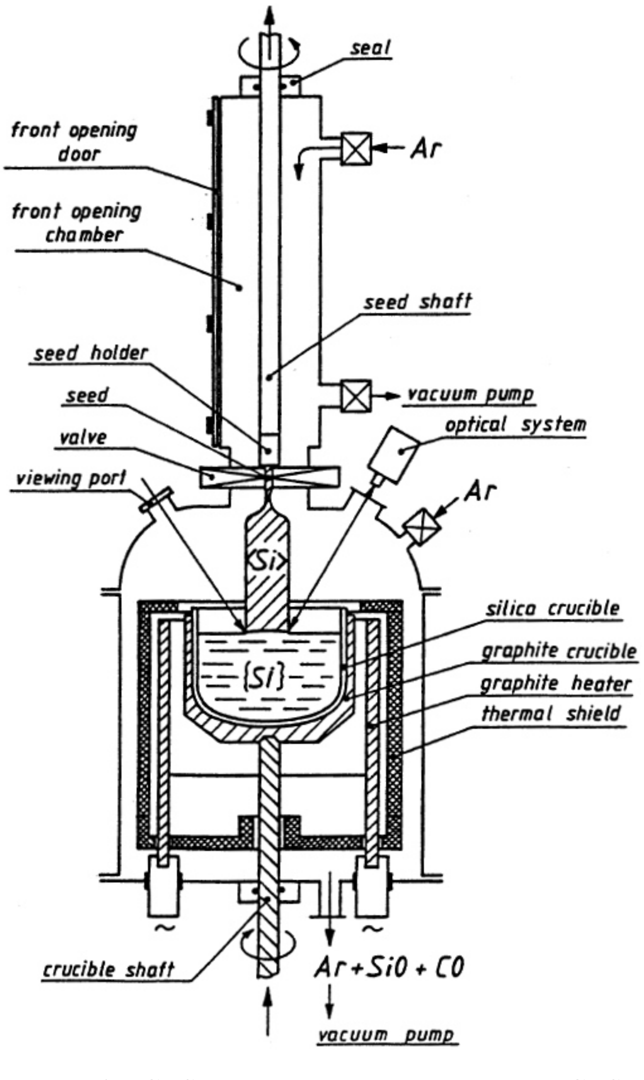

FIGURE 2.1: Schematic of a Cz-Si single crystal puller. Modern Cz-Si puller feature additional heat shields between melt and crystal. [8]

after it is grown. For example, the state of nuclei of oxygen precipitation, the oxygen concentration and the oxygen precipitation kinetics are determined by the temperature profile the crystal experienced.

2.1.2.2 Intrinsic point defects

Even without the incorporation of intended or unintended impurities, every real crystal differs from the theoretical crystal lattice due to the presence of intrinsic point defects. Intrinsic point defects basically describe crystal lattice sites which are not occupied by silicon atoms, also referred to as vacancies, or silicon atoms which are not positioned on a crystal lattice site but in-between different sites. The latter configuration is also referred to as Si self-interstitials. For thermodynamic reasons, these point defects exist at every temperature $T > 0\,\mathrm{K}$. By aggregation of vacancies or self-interstitials with the same species, micro-defects are formed, which may have a detrimental effect on the performance of ICs, especially as the size of these devices decreases. Accordingly, the minimization of the grown-in micro-defects has been of great interest in the past years in microelectronics industry.

The defect type, whether it is a vacancy or a self-interstitial, is determined by the condition under which the crystal is grown [9]. More precisely, the ratio between the growth rate V and the axial temperature gradient at the crystal-melt interface G determines the species with the highest concentration. A critical value ζ exists, which marks the transition between the vacancy-rich and the self-interstitial-rich crystal. For $V/G > \zeta$ vacancies are the remaining species, while for $V/G < \zeta$ self-interstitials are the remaining species. The value ζ has been determined experimentally and varies between $\zeta = 0.13\,\mathrm{mm}^2/(\mathrm{min}\,^\circ\mathrm{C})$ [10] and $\zeta = 0.22\,\mathrm{mm}^2/(\mathrm{min}\,^\circ\mathrm{C})$ [11]. The growth rate V can be considered constant over the complete crystal diameter, however, due to the cooling at the crystal surface, the temperature gradient G along the diameter generally strongly increases from the centre to the edge of the crystal. Hence, a transition from a vacancy-rich crystal in the centre to a self-interstitial-rich crystal at the surface is possible. Additionally, the V/G-curve also varies over the crystal length and hence the transition between vacancy- to interstitial-rich region does not occur at the same distance from the crystal centre over the whole crystal length.

Of course, as vacancies and interstitials are intrinsic point defects, these defects also exist in FZ-Si. Due to the high growth rate of FZ-Si, about 2 to 3 times larger than for Cz-Si, FZ-Si is usually dominated by grown-in vacancy-type defects.

2.1.2.3 Unintended impurities

Apart from the intended impurities, such as the doping atoms boron or phosphorus, also unintended impurities exist within a Cz-Si crystal. In general, the elements which are released from the crucible material or incorporated from the vapour above the melt can be considered as unintended impurities. The most common unintended impurities in Cz-Si are oxygen and carbon. Typical concentrations are $[\mathrm{O}_i] = 10^{18}\,\mathrm{cm}^{-3}$ and $[\mathrm{C}_s] = 10^{16}\,\mathrm{cm}^{-3}$ for oxygen and carbon [12], respectively.

The pathway of oxygen into the Cz-Si crystal is as follows: The oxygen from the crucible or its coating is dissolved by the molten silicon and the convection in the liquid phase distributes the oxygen inhomogeneously throughout the melt. At the surface, up to 90 % of the dissolved oxygen evaporates to the inert gas atmosphere of the growth chamber. The remaining part can in principle be incorporated into the crystal. However, as the distribution in the silicon melt is not homogeneous, the incorporation does not follow a normal freezing behaviour. In contrast, the incorporation is a complex interplay between the dissolution at the crucible, which depends on the contact area between the melt and the crucible, the surface evaporation, which for example also depends on the surface area and the ambient pressure, and the convection within the melt, which depends on the temperature profile as well as on the rotation of crystal and crucible. Hence, the variation of the thermal characteristics of different growers results in different amounts of incorporated oxygen.

2.2 Oxygen aggregation and precipitation

Oxygen in silicon has been studied for more than 50 years and a variety of experimental results regarding the behaviour of oxygen in silicon exist. It is accepted that oxygen is thermodynamically stable at an interstitial site. At this position one oxygen atom is covalently bonded to two neighbouring silicon atoms. In this configuration oxygen is electrically inactive.

As outlined above, oxygen is frozen-in from the silicon melt during solidification. The solubility at the silicon melting point is $C_{sol} = 2.75 \times 10^{18}\,\mathrm{atoms/cm}^3$. As the solubility strongly decreases with decreasing temperature, oxygen is within a supersaturated state for most standard processing temperatures [12] and precipitation can occur.

2.2.1 Precipitation

Because of this supersaturation, nucleation can arise spontaneously and randomly in time and space at sufficiently high temperatures. Nuclei are usually aggregates formed

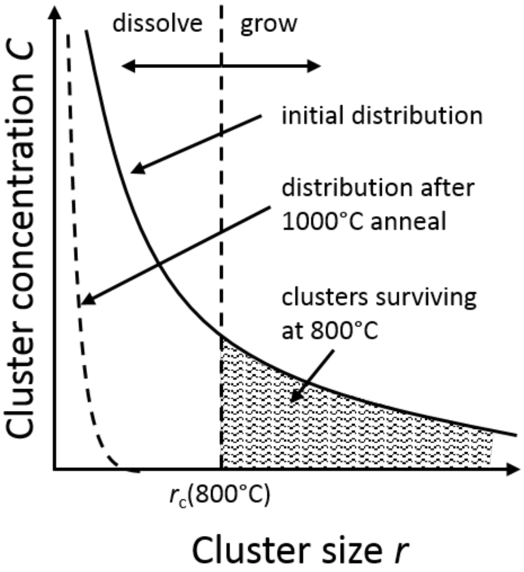

FIGURE 2.2: Schematic representation of the oxygen cluster distribution in a silicon sample. The solid black line indicates the initial cluster distribution while the dashed line indicates the approximately monomer-like distribution after a 'tabula rasa' anneal at 1000 °C. Graphic adapted from [16].

by a few oxygen atoms. According to classical nucleation theory, a critical radius r_c exists which determines whether a given nucleus under consideration will grow at a certain temperature or whether it will shrink. This critical radius is rapidly increasing with temperature. For $r < r_c$ the nucleus will tend to dissolve upon thermal treatment while a nucleus with $r > r_c$ will further grow and form an oxide precipitate. The critical radius itself depends on several characteristics of the silicon crystal like the concentration of silicon self-interstitials and vacancies as well as on impurities being present in the crystal and of course also on the temperature. Due to this large number of variables which influence oxygen precipitation, a variety of different oxygen cluster distributions can be observed in crystals featuring the same oxygen concentration. High concentrations of oxygen precipitates reduce the material quality and it becomes unsuitable for solar cell production [13, 14]. Hence, precipitation needs to be avoided.

To avoid precipitation in the silicon bulk, a brief high-temperature treatment can be applied prior to the solar cell processing sequence. This high-temperature treatment is often referred to as 'tabula rasa' [15]. This tabula rasa treatment, which leads to a precipitation-hard silicon material, benefits from the fact that nucleation and the final growth to precipitates proceed in different temperature regimes. While nucleation usually takes place at low temperatures between 400 °C and 700 °C, the precipitate growth needs higher temperatures of approximately 1000 °C. On the other hand, at growth temperatures of 1000 °C no sufficient nucleation occurs [16]. Qualitatively, the behaviour of oxygen precipitates during annealing can be explained as follows:

After crystal growth, an unknown cluster distribution $C(r)$, depending on the material composition and the thermal history, will be present in the sample under investigation (solid black line in Fig. 2.2). If the sample is then exposed to e.g. a diffusion step at around 800 °C, all clusters larger than $r_c(800\,^\circ\mathrm{C})$ (shaded area in Fig. 2.2) will survive the temperature treatment and grow upon annealing along the x-axis to larger precipitates. All clusters smaller than r_c, on the other hand, will dissolve during the treatment. As indicated, a large part of the initial cluster distribution will survive the annealing step and may reduce the material quality if a significant number of precipitates reach a relevant size.

During the tabula rasa treatment, the sample is exposed to a temperature higher than the typical processing temperatures in the range of 1000 °C. As $r_c(800\,^\circ\mathrm{C}) < r_c(1000\,^\circ\mathrm{C})$ a large part of the clusters, which would have survived the annealing at 800 °C in the previous example, will now tend to dissolve during the annealing. Depending on the initial distribution, only a negligible concentration of clusters is larger than $r_c(1000\,^\circ\mathrm{C})$ and therefore survives this annealing step. Hence, an approximately monomeric-like cluster distribution is realized (as indicated by the black dashed line in Fig. 2.2). Apart from the maximum temperature during the anneal, also the heating and the cooling before and after the process is very important. Ideally, the heating and cooling is performed instantaneously with infinite heating and cooling rates, as in this case, the oxygen clusters cannot grow to larger sizes, with $r > r_c(max)$, during the heating which would hamper the dissolution of these clusters. Also, the cooling should be sufficiently fast since in this case no nuclei can be formed during the cooling and the final cluster distribution does not deviate from the narrow high temperature distribution. When starting from such a relaxed cluster distribution, no measurable oxygen precipitation can be observed for temperatures above 750 °C [16] and the material can hence be considered as ‘precipitation-hard’.

2.3 Boron-oxygen-related defect centres

2.3.1 Generation of boron-oxygen-related recombination centres: A review of previous experimental and theoretical work

In boron-doped, oxygen-rich crystalline silicon, the carrier lifetime (see chapter 3) degrades upon illumination. This phenomenon, which has been known for more than 40 years, is often referred to as light-induced degradation (LID). As an example, in Fig. 2.3 (a) the typical degradation of the lifetime (measured using a photoconductance decay method (see section 3.2.1) and extracted at a fixed injection density of

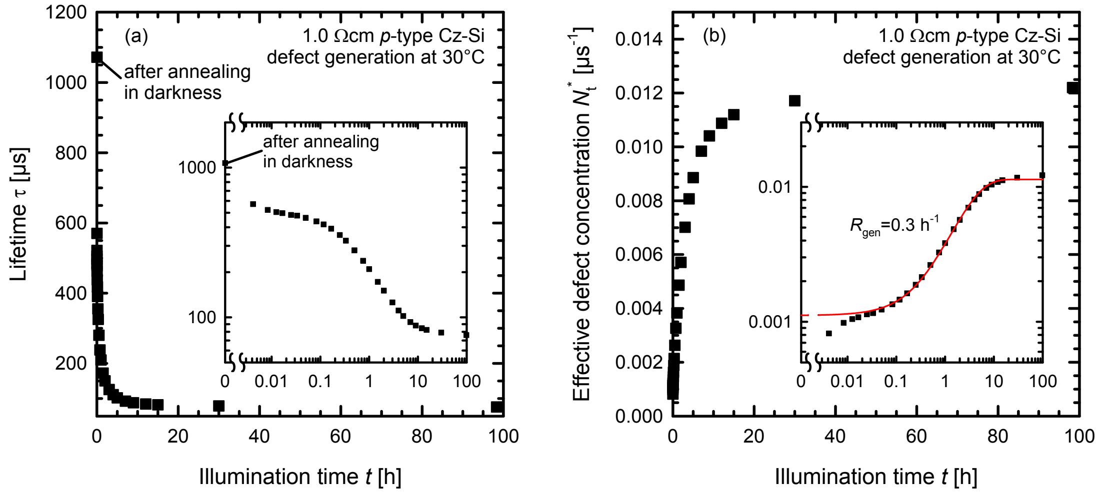

FIGURE 2.3: (a) Typical degradation behaviour of the lifetime τ of a 1.0 Ω cm boron-doped p-type Cz-Si sample under illumination at 30 °C due to the formation of the boron-oxygen defect. The lifetime is measured using the photoconductance decay method and is extracted at a fixed injection density of $\Delta n = 1.5 \times 10^{15}\,\mathrm{cm}^{-3}$. (b) Effective defect concentration N_t^* determined from the lifetime data in (a). The insets in both plots show the corresponding quantities in a double logarithmic scaling. The defect generation in (b) can be fitted with an exponential rise to maximum function (red line) with a generation rate constant $R_{gen} = 0.3\,\mathrm{h}^{-1}$. Within the first seconds N_t^* deviates from the exponential fit due to the influence of the fast forming centre.

$\Delta n = 1.5 \times 10^{15}\,\mathrm{cm}^{-3}$) is shown for a typical 1.0 Ω cm boron-doped Cz-Si sample. After annealing in darkness, when the boron-oxygen defect is not limiting the lifetime, a lifetime well above 1000 µs is measured. Upon illumination with a halogen lamp at a light intensity of 10 mW/cm^2 at 30 °C, the lifetime decreases within approximately 100 hours to a saturation value of 76 µs. As can be seen in the double logarithmic scaling, the lifetime degradation proceeds via two stages, a fast initial degradation which is followed by a slower second degradation. The decreasing lifetime corresponds to an increase of recombination-active defects, which are accordingly divided into fast-forming and slow-forming defect centres. Assuming that all other recombination channels remain unchanged upon illumination, an effective defect concentration N_t^* of the boron-oxygen-related defect centre can be calculated according to

$$N_t^* \equiv \frac{1}{\tau(t)} - \frac{1}{\tau_0}. \tag{2.1}$$

τ_0 refers to the lifetime measured directly after annealing in darkness, when the boron-oxygen defect does not limit the lifetime. In Figure 2.3 (b) the defect concentration is plotted versus the illumination time. The increase of the defect concentration for one degradation stage can be described by an exponential function of the form: $y = y_0 + a[1 - \exp(-R_{gen} \times t)]$, where R_{gen} is the generation rate constant. In case of the example in Fig. 2.3 (b), fitting this equation to the data results in a generation rate constant of $R_{gen} = 0.3\,\mathrm{h}^{-1}$ for the slow-forming defect centre. Please note that it is not a direct interaction of the defect centres with photons that causes the observed degradation of the lifetime but the presence of excess charge carriers [17].

In the following, a survey of the main experimental and theoretical results on the boron-oxygen-related defect generation, which has been published prior to this work, is briefly presented.

More than 40 years ago, in 1974, Fischer and Pschunder [3] observed “photon and thermal induced” changes in silicon solar cells. Upon illuminating a solar cell for 12 hours with an AM0 spectrum, they observed a reduced red spectral response. They concluded that this was due to a photon-induced decay of the lifetime in the solar cell base. A subsequent temperature treatment between 80 °C and 200 °C restored the initial performance of the cell. Consequently, they introduced two different levels, describing the physical state of the high and low performance of the solar cell. Applying the proper treatments, they observed that the state of the solar cell can be reversibly changed between the two levels. Direct measurements of the lifetime additionally supported the interpretation of a degrading bulk lifetime upon illumination.

More than 20 years later, in 1997, Schmidt el al. [18] investigated various Cz-Si materials doped with boron, gallium and phosphorus. While the lifetime in gallium- and phosphorus-doped material remained stable upon illumination, boron-doped material showed a pronounced degradation of the lifetime. Additionally, the extent of degradation increased with increasing boron concentration. Hence, it was concluded that boron is directly participating in a recombination-active defect centre responsible for the reduction in lifetime. Since this defect behaves similar to the annealing behaviour of the well-known $\mathrm{B}_i\mathrm{O}_i$ pairs, it was proposed that the defect responsible for LID is in fact the $\mathrm{B}_i\mathrm{O}_i$ pair.

Within further investigations, Glunz et al. [19] introduced the effective defect concentration, calculated by subtracting the inverse lifetime after annealing in darkness from the inverse lifetime after light-induced degradation, i.e. $1/\tau_d - 1/\tau_0$, and observed a linear increase of the defect concentration with the boron concentration N_A. Additionally, they observed a strong dependence on the interstitial oxygen concentration.

In 1999, Schmidt and Cuevas [20] performed a detailed analysis of the electrical properties of the defect centre by analysing the injection-dependent lifetime curves of various samples after annealing in darkness and after illumination. Using Shockley-Read-Hall theory, they localized the energy level of the defect in the middle of the band gap between $E_v + 0.35\,\mathrm{eV}$ and $E_c - 0.45\,\mathrm{eV}$. The ratio of the capture cross sections was found to be $\sigma_n/\sigma_p = 10$. As these electrical properties contradict the hypothesis of $\mathrm{B}_i\mathrm{O}_i$ being the relevant complex, Schmidt and Cuevas proposed the defect to consist of a substitutional boron atom B_s and an agglomerate of n interstitial oxygen atoms O_{ni}.

One year later, Glunz et al. [21], further examined the defect formation. Within this study, they observed a quadratic increase of the generation rate constant on the doping concentration, $R_{gen} \propto N_A^2$. Based on this finding, they proposed that the defect formation proceeds via a recombination-enhanced defect reaction.

Investigations on thermal-donor-compensated boron-doped, n-type, oxygen-rich silicon by Bothe et al. [22] in 2002 revealed that light-induced degradation can also be observed in n-type silicon, if boron is present.

Later that year, Rein and Glunz [23] performed an unambiguous determination of the electronic properties of the defect centre by combining data from temperature-dependent and injection-dependent lifetime spectroscopy (TDLS and IDLS). This combination showed that the energy level of the boron-oxygen-related defect centre is located 0.41 eV below the conduction band edge and the ratio of the capture cross sections is $\sigma_n/\sigma_p = 9.3$.

In 2003, Schmidt et al. [24] showed that the degradation proceeds independently of the light intensity for illumination intensities above $1\,\mathrm{mW/cm^2}$. Below this intensity, a linear increase of the degradation rate constant with the illumination intensity was observed. At the same conference in 2003, Hashigami et al. [25] presented time-resolved measurements of the open-circuit voltage of solar cells upon current injection. These measurements showed that the defect formation proceeds via two stages, a fast stage which proceeds in the range between seconds and minutes and a slow stage which proceeds in the range of several hours. Additionally, they observed the independence of the degradation process for light intensities above $1\,\mathrm{mW/cm^2}$. Furthermore, they observed both degradation stages to be thermally activated with an activation energy for the fast stage $E_{a,fast} = 0.19\,\mathrm{eV}$ and for the slow stage between $E_{a,slow} = 0.40\,\mathrm{eV}$ and $E_{a,slow} = 0.46\,\mathrm{eV}$.

One year later, in 2004, Schmidt and Bothe [26] proposed a new defect model based on their experimental findings that the effective defect concentration depends linearly on the doping concentration N_A and quadratically on the interstitial oxygen concentration $[\mathrm{O}_i]$ [24]. In this model, the defect complex consists of a substitutional boron atom B_s and an oxygen dimer O_{2i}. It is assumed that this defect complex is formed under illumination due to the recombination-enhanced diffusion of the oxygen dimer. In 2005, Bothe and Schmidt [27] presented a detailed study on the fast-forming component of the defect complex. Their analysis revealed the energy level of the fast-forming centre to be $E_t = E_v + 0.60\,\mathrm{eV}$ and the ratio of capture cross sections to be $\sigma_n/\sigma_p = 100$, i.e. one order of magnitude larger than the ratio for the slowly forming component. They reported an activation energy of this process of $E_{a,fast} = 0.23\,\mathrm{eV}$. Later, in 2006, they also determined the activation energy for the slowly forming component to be $E_{a,slow} = 0.475\,\mathrm{eV}$ [28]. Based on their experimental results, Bothe and Schmidt suggested that the fast-forming centre is formed via a reconstruction process of the latent $\mathrm{B}_s\mathrm{O}_{2i}$ into its recombination-active form. This reconstruction is assumed to proceed via three steps: first the latent B_sO_{2i} complex changes its charge state C, $C^+ \rightarrow C^0$, second a thermally activated structural transition to a new structure D occurs, $C^0 \rightarrow D^0$, and at last another change of the charge state, $D^0 \rightarrow D^+$, takes place [28].

A refined version of the B_sO_{2i} model was presented in 2007 by Palmer et al. [29]. Within this model it was assumed that the positively charged defect complex $B_sO_{2i}^+$, responsible for the slowly forming component of the LID, is formed by the diffusion of a positively charged oxygen dimer O_{2i}^{++} interacting with the negatively charged, fixed substitutional boron atom B_s^-. The diffusivity of the dimer within the model is thought to be increased under illumination by a recombination-enhanced process referred to as 'Bourgoin mechanism' [30]. This process would allow the migration of the oxygen dimer at room temperature [31]. Theoretical analysis within the model led to predictions for the defect formation kinetics. It was concluded that the generation rate constant R_{gen} is proportional to the product of the hole concentration p_0 and the total boron concentration N_A, i.e. $R_{gen} \propto p_0 \times N_A$. This was found to be in excellent agreement to the existing experimental results for exclusively boron-doped Cz-Si.

In 2008, Kopecek et al. [32] observed on solar cells made of phosphorus-compensated boron-doped, p-type silicon that the degradation of the open-circuit voltage V_{oc} is more pronounced for lower boron concentrations compared to higher boron concentrations, which was in contradiction to the experimental results on boron-only doped Cz-Si.

One year later, in 2009, Macdonald et al. [33] presented a lifetime study on P-compensated p-type Cz-Si in which the defect concentration as well as the defect generation were examined. In both cases, the defect concentration and the defect generation rate was found to depend on the net doping concentration $p_0 = N_A - N_D$ rather than on the boron concentration N_A, i.e. $N_t^* \propto p_0$ and $R_{gen} \propto p_0^2$. It was assumed that the compensated boron is not able to bond to oxygen dimers and thus prohibits the defect formation. The authors hypothesized that boron-phosphorus pairs, which form at very high temperatures during ingot growth, could be responsible for this effect.

Voronkov and Falster [34] presented in 2010 a new defect model which attributed the observed degradation of the lifetime to a defect complex consisting now of an interstitial boron atom B_i and an interstitial oxygen dimer O_{2i}, i.e. B_iO_{2i}. This defect complex was assumed to be formed at elevated temperatures during crystal cooling and hence is assumed to be present within the silicon in a latent (recombination-inactive) or in a recombination-active form. The interstitial boron, and consequently the defect concentration, was proposed to be proportional to the net doping concentration p_0 which was in agreement to the existing experimental data on boron-doped Cz-Si and on compensated p-type Cz-Si. Apart from that, the model also explained the quadratic dependence of the generation rate constant R_{gen} on p_0. This dependence was explained by a recharging mechanism of the latent centre, which requires two holes, to be transferred to the recombination-active centre in the presence of excess electrons.

2.3.2 Permanent deactivation of boron-oxygen-related recombination centres: A review of previous experimental and theoretical work

The carrier lifetime in boron-doped oxygen-rich crystalline silicon can be permanently recovered under illumination at elevated temperatures. Figure 2.4 (a) shows the typical evolution of the lifetime of a 1.0 Ω cm *p*-type Cz-Si sample (measured using a photoconductance decay method (see section 3.2.1) and extracted at a fixed injection density of $\Delta n = 1.5 \times 10^{15}\,\mathrm{cm}^{-3}$) exposed to the recovery conditions at 185 °C and $100\,\mathrm{mW/cm}^2$ light intensity using a halogen lamp as light source. The sample is exposed to these conditions after it has been annealed in darkness. Accordingly, the lifetime shows an accelerated degradation due to the elevated temperatures, which is followed by a recovery of the lifetime. In Fig. 2.4 (b), the lifetime values are transformed into an effective defect concentration using to Eqn. 2.1. The evolution can be described by an exponential decay function: $y = y_0 + a \exp(-R_{de} \times t)$. In Fig. 2.4 (b) this function is fitted to N_t^* (red line) and a recovery rate constant of $R_{de} = 83\,\mathrm{h}^{-1}$ is obtained.

In the following, the main experimental and theoretical results on the permanent deactivation of the boron-oxygen related defect centre published before the beginning of this work will be briefly summarized:

In 2006, Herguth et al. [4] observed that the open-circuit voltage of solar cells, made of boron-doped, oxygen-rich Cz-Si, can be recovered after LID if the cell is exposed to illumination at elevated temperatures. They also showed that the reached new state of the solar cell is stable upon further illumination at room temperature as well as under the application of a forward bias voltage for more than 100 hours. Additional temperature-dependent measurements revealed that this recovery process is thermally activated with an activation energy between $E_a = 0.62\,\mathrm{eV}$ and $E_a = 0.92\,\mathrm{eV}$. One year later, in 2007, they presented further results which revealed that the recovery process is induced in the presence of free charge carriers and hence no photons are involved [35]. An investigation of the recovery rate constant depending on the illumination intensity showed that an increasing illumination intensity as well as an increasing forward bias voltage result in an increasing recovery rate constant [35]. The exact functional dependence, however, remained unclear.

Lim et al. [36] presented lifetime investigations of the permanent deactivation process at various temperatures between 135 °C and 212 °C. They confirmed that the process is thermally activated with an activation energy of $E_a = 0.7\,\mathrm{eV}$. Within the study of Lim et al. [36], different sample groups were investigated: one group of as-grown samples and one group of samples which underwent an additional P-diffusion step. For all investigated temperatures the latter group revealed higher recovery rate constants than the

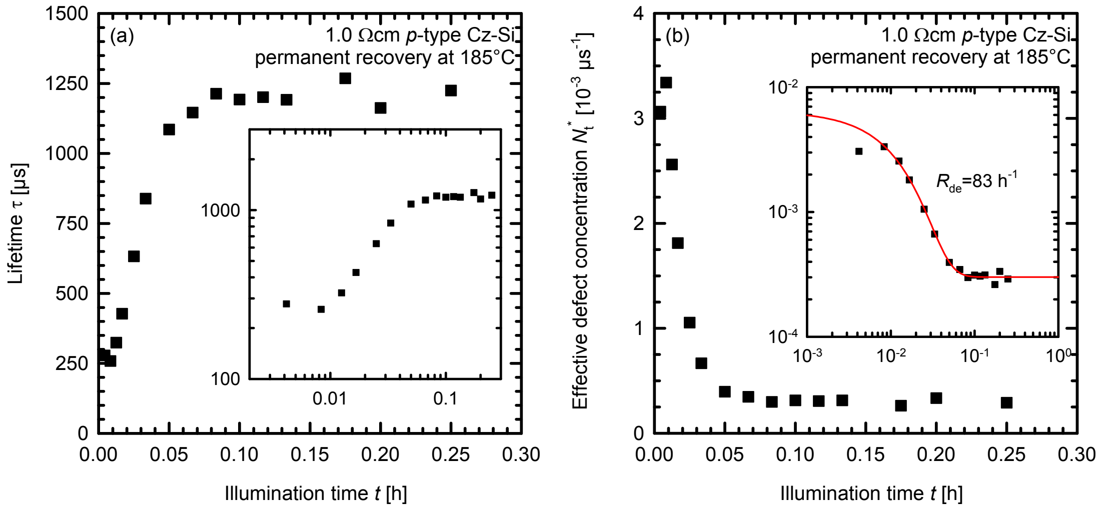

FIGURE 2.4: (a) Typical permanent recovery behaviour of the lifetime τ, determined using a photoconductance decay method (see section 3.2.1) and extracted at a fixed injection density of $\Delta n = 1.5 \times 10^{15}\,\mathrm{cm}^{-3}$, of a $1.0\,\Omega\,\mathrm{cm}$ boron-doped p-type Cz-Si sample under illumination at 185 °C due to the permanent deactivation of the boron-oxygen defect. (b) Effective defect concentration N_t^* determined from the lifetime data in (a). The insets in both plots show the corresponding quantities in a double-logarithmic scaling. The reduction of the defect concentration in (b) can be fitted with an exponential decay function (red line) with a recovery/deactivation rate constant $R_{de} = 83\,\mathrm{h}^{-1}$. Within the first seconds N_t^* deviates from the exponential fit as the deactivation was performed directly after annealing in darkness. The first data point shows the influence of the accelerated defect formation at elevated temperatures.

first group. However, the extracted recovery rate constants were considerably lower compared to the results of Herguth et al.. Additionally, a first model to physically describe the observed lifetime recovery was presented. Within this model the influence of an additional defect complex XY was postulated which dissociates under the deactivation conditions and forms a sink for the oxygen dimers, e.g. XO_{2i}. Since the concentration of O_{2i} is reduced, the concentration of $\mathrm{B}_s\mathrm{O}_{2i}$ is also reduced.

In 2009, Münzer [37] presented a study which compared the permanent recovery behaviour of solar cells treated with different dielectric layers. Only solar cells which were coated with a hydrogen-rich silicon nitride layer showed a recovery of the solar cell performance. Hence, it was speculated that hydrogen introduced from the dielectric layer has a major influence on the recovery process. In the same year, Lim et al. [38] presented results on P-compensated Cz-Si. They showed that the recovery rate constant is inversely proportional to the boron concentration, i.e. $R_{de} \propto N_A^{-1}$. Together with the experimental result that the activation energy of the deactivation process depends linearly on N_A they concluded that boron atoms are directly involved in the deactivation mechanism.

One year later, in 2010, Lim et al. [39] investigated the dependence of the permanent BO deactivation on the interstitial oxygen concentration. They observed the correlation:

$R_{de} \propto [\mathrm{O}_i]^{-1.5\pm0.2}$. Additionally, their study revealed that the hydrogen concentration in the dielectric layer does not influence the deactivation behaviour.

2.3.3 BO defect models

In the following section, a short summary of three important defect models describing the physical origin for the observed BO-related lifetime degradation and recovery will be presented. At first, a model which associates the recombination-active centre with the $\mathrm{B}_s\mathrm{O}_{2i}$ complex will be explained. Afterwards, a defect model is discussed which assumes the participation of an interstitial instead of a substitutional boron atom and, hence, assumes the $\mathrm{B}_i\mathrm{O}_{2i}$ complex to be the relevant defect centre. Finally, a model in which the involvement of an oxygen dimer is omitted will be discussed. In the recent model, the recombination-active centre is assumed to be a $\mathrm{B}_i\mathrm{B}_s\mathrm{O}_i$ complex.

2.3.3.1 The $\mathrm{B}_s\mathrm{O}_{2i}$ model

One of the earliest models describing the physical mechanisms behind the observed light-induced degradation in boron-doped oxygen-rich silicon was proposed by Schmidt et al. [40] in 2002 and later further refined by Palmer, Bothe and Schmidt [29]. In the following, the basic principle of the model and its limitations shall be outlined.

In the model, it is assumed that the observed degradation in lifetime is due to an actual defect reaction within the silicon bulk. As the defect concentration N_t^* increases linearly with doping concentration N_A and quadratically with the interstitial oxygen concentration $[\mathrm{O}_i]$, it was suggested that a defect reaction occurs between a substitutional B_s atom and an oxygen cluster. As B_s is immobile, the oxygen cluster had to be the mobile species. In particular, Gösele et al. [41] showed that the oxygen dimer O_{2i} can be an extremely fast diffusing species. Apart from the temperature-driven diffusion, this diffusion can also proceed athermally via a charge-enhanced migration mechanism as proposed by Bourgoin and Corbett [30]. Figure 2.5 shows a configuration-coordinate diagram of the diffusion of the oxygen dimer via a Bourgoin-Corbett mechanism as presented by Adey et al. [31]. According to Ref. [31], the oxygen dimer exists in two configurations, the squared configuration (O_{2i}^{sq}) and the staggered configuration (O_{2i}^{st}). In *p*-type silicon oxygen is double-positively charged. At this charge state, the energy barrier for the transition from the squared to the staggered configuration is 0.86 eV and, hence, too high to enable diffusion at room temperature. However, if the material is illuminated the oxygen dimer is assumed to capture an electron ($\mathrm{O}_{2i}^{sq,++} \rightarrow \mathrm{O}_{2i}^{sq,+}$) which reduces the energy barrier for this transition significantly to 0.2 eV. After the reconfiguration into the staggered form, it is assumed that the oxygen dimer is recharged again

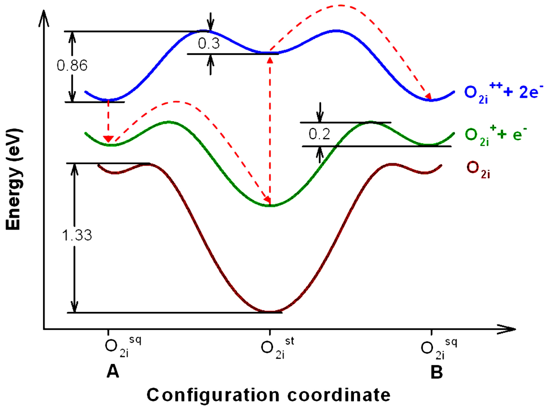

FIGURE 2.5: Configuration-coordinate diagram of the oxygen dimer diffusion. The dashed red arrows indicate the diffusion via a Bourgoin-Corbett mechanism [42].

to its double-positive state ($O_{2i}^{st,+} \rightarrow O_{2i}^{st,++}$) by emitting an electron. From this point, the energy barrier for the transition from the staggered to the squared configuration is 0.3 eV. Accordingly, following the proposed mechanism, the energy barrier for the dimer diffusion is reduced from 0.86 eV to 0.3 eV which enables the dimer diffusion at room temperature. As the oxygen dimer O_{2i} is the mobile species within this model, it was consequently assumed that the oxygen dimer is captured by the substitutional, immobile boron atom B_s.

Within this model, the defect concentration N_t^* is naturally proportional to the boron concentration N_A. The defect generation rate constant R_{gen}, according to the model, is defined by two capturing processes required for the defect formation: the capturing of a hole by the oxygen dimer in order to enhance its diffusivity (see Fig. 2.5) and the capturing of the oxygen dimer by the immobile boron atom. Hence, the defect generation rate R_{gen} is proportional to the hole concentration and the boron concentration, i.e. $R_{gen} \propto p_0 \times N_A$ (see Fig. 2.6), which is in very good agreement to the results published on boron-only doped Cz-Si at that time.

With regard to the quadratic dependence of N_t^* on the interstitial oxygen concentration $[O_i]$, it was shown by Murin et al. [43] that indeed the concentration of oxygen dimers is proportional to $[O_i]^2$. Hence, the dependence $N_t^* \propto [O_i]^2$ follows from the reasonable assumption that $[O_{2i}] << N_A$ and that the defect generation ceases when all oxygen dimers are captured by the boron atoms.

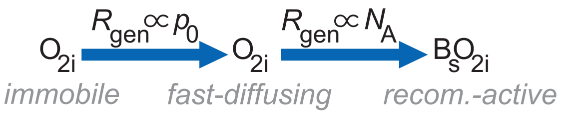

FIGURE 2.6: Schematic of the defect generation mechanism in the B_sO_{2i} defect model as proposed in [29].

The model describing the permanent deactivation of the defect centre presented by Lim et al. [36], mentioned above, can be considered as an extension to the B_sO_{2i} model, since their deactivation model is based on the same defect centre.
Although the model is in good agreement with the results obtained from boron-only doped Cz-Si, the results obtained on compensated boron-doped Cz-Si brought the accuracy of this model into question. As it was shown by Macdonald et al. [33] and Lim et al. [39], the defect concentration in these materials does not depend on the boron concentration but on the net doping concentration p_0, i.e. $N_t^* \propto p_0$. The observed dependence of the defect generation rate constant also deviates from the predictions within the model, as the dependence $R_{gen} \propto p_0^2$ was observed. Thus, these experimental findings called for a reassessment of the B_sO_{2i} model.

2.3.3.2 The B_iO_{2i} model

In contrast to the previous model, the B_iO_{2i} model, introduced by Voronkov and Falster [34] in 2010, is not based on a direct defect reaction upon illuminating the silicon material. Contrarily, it is assumed that the illumination induces an electron-driven reconstruction of a latent defect complex into its recombination-active form. Please note that the B_iO_{2i} model mainly discusses the physical origin of the slow component of the defect formation, however, as the authors point out, the fast component of the defect formation may just be another configuration of the B_iO_{2i} complex.
During the cooling of the ingot after crystal growth, the incorporated interstitial oxygen starts to nucleate. The growth of the nuclei emits self-interstitials, which to some fraction also consist of doping atoms, i.e. B_i. Upon lowering the temperature, the free interstitial boron atoms start to form small B_i clusters (sometimes also referred to as 'boron nano-precipitates' (B-NPs)) and an equilibrium between the free B_i and the B-NPs is established. Since B_i is a single positively charged defect in *p*-type silicon, the frozen-in equilibrium concentration of B_i depends on the hole concentration p. Once the material is no longer intrinsic, typically at $\vartheta < 350\,^\circ\mathrm{C}$, the equilibrium concentration becomes proportional to p_0. The highly mobile B_i migrates through the crystal and forms complexes with possible traps. Possible candidates for these traps are O_{2i}, O_i or B_s. It is reasonable to assume that all these complexes, i.e. B_iO_{2i}, B_iB_s and B_iO_i exist in parallel and are in equilibrium with $[B_i]$. From the mentioned complexes, the B_iO_{2i} shows naturally the experimentally observed dependence since $[B_iO_{2i}] \propto [B_i] \times [O_i]^2$. Below some freeze-in temperature the exchange between the B_i-clusters and the free B_i is suppressed and, hence, the concentration of the B_iO_{2i} complex is also frozen-in.

The observed degradation of the lifetime in boron-doped Cz-Si is then explained by a reconstruction from the latent form of the B_iO_{2i}, denoted as latent centre LC, into its

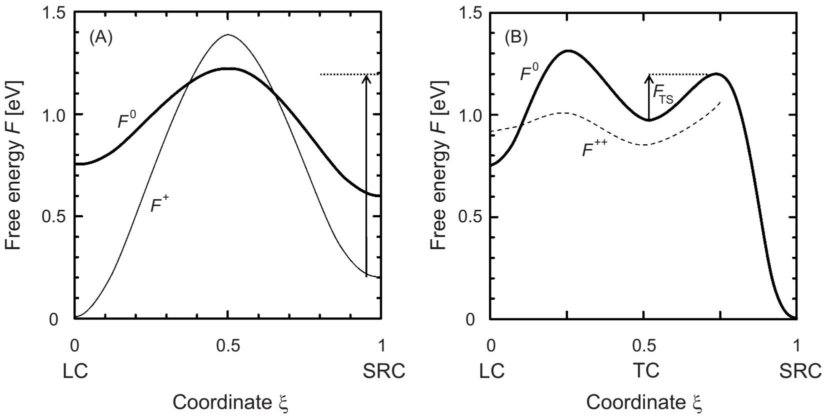

FIGURE 2.7: Free energy diagrams of the latent centre (LC) and the recombination-active slow centre (SRC) of the B_iO_{2i} defect model as proposed in Ref. [34].

recombination-active form, denoted as slow recombination centre SRC. Accordingly, the reconstruction itself cannot depend on the boron concentration $[B_s]$ or the interstitial oxygen concentration $[O_i]$. However, it can depend on the hole concentration if an exchange with charge carriers is needed for the reconstruction. In fact the experimental finding that the defect generation rate constant is proportional to the square of the hole concentration [39] suggests that the transition from LC to SRC involves the capture of two holes. On the other hand, the rate constant for the annihilation in darkness was found to depend inversely on the hole concentration [28], hence, it is assumed within the model that the B_iO_{2i} complex reconstructs under the emission of a hole from its SRC to LC form. Figure 2.7 shows two configuration-coordinate diagrams for the defect annihilation (A), i.e. the transition from SRC to LC via annealing in darkness, and the defect generation (B), i.e. the transition from LC to SRC via illumination (carrier injection) at room temperature. In darkness it is assumed that SRC^+ is single-positive and the energy minimum for this charge state is the single positive LC^+. As shown in Fig. 2.7 (A), an energy barrier between the two configurations, depicted by the black arrow, needs to be overcome. During the transition, the defect centre remains in the charge state with the lowest free energy, hence, SRC^+ moves along the free energy curve of the single-positive state F^+ until the intersection with the neutral state curve F^0 is reached. At this point, SRC^+ changes its charge state to SRC^0 by emitting a hole. This way the energy barrier for the transition to LC^0 is considerably reduced and can now be overcome via thermal activation. At the next intersection LC^0 is recharged again by capturing of a hole to LC^+. As the transition from SRC^+ to LC^+ involves the emission of a hole, the concentration of neutral B_iO_{2i} in equilibrium is proportional to $1/p_0$, which determines the dependence of the annihilation rate.

As mentioned above, the generation rate constant was found to be proportional to p_0^2, which suggests that the transition from LC to SRC involves the capture of two holes.

Hence, it is assumed within the model that the transition proceeds via a transition centre (TC) as shown in Fig. 2.7 (B). In the presence of excess carriers, LC^0 captures two holes and, hence, recharges to LC^{2+}. At this state, the energy barrier to TC^{2+} is strongly reduced. Then TC^{2+} changes its charge state to TC^0 via the emission of two holes. Finally, through overcoming the energy barrier F_{ts}, TC^0 is transformed into SRC^0.

Within the B_iO_{2i} model, the physical mechanism of the permanent lifetime recovery under illumination at elevated temperatures is described by the dissociation of the B_iO_{2i} complex into an interstitial boron atom B_i and into an interstitial oxygen dimer O_{2i}. The B_i is then either consumed by the B-NPs or captured by other traps:

$$B_iO_{2i} \rightleftharpoons B_i + O_{2i} \rightleftharpoons B_i\text{-NPs}$$

Through this process under illumination at elevated temperatures, the concentration of B_iO_{2i} complexes is permanently reduced. However, according to the model, annealing in darkness will dissolve the B-NPs and B_iO_{2i} complexes can be formed again. Hence, subsequent illumination will lead again to the reconstruction of LC into the SRC and the lifetime will degrade. Figure 2.8 shows a schematic of the permanent recovery and possible destabilization within the B_iO_{2i} model. The B_iO_{2i} model is in very good agreement with the recent results by Macdonald et al. [44] and Lim et al. [45] on boron-doped Cz-Si compensated with phosphorus. However, more recently, Forster et al. [46] observed on boron-doped Cz-Si co-doped with gallium that in this case the effective defect concentration N_t^* is not proportional to the net doping concentration p_0 but to the boron concentration $[B_s]$. This finding together with the reasoning of Voronkov et al. [47] that oxygen dimers cannot be involved in the defect reaction required a modification of the defect model.

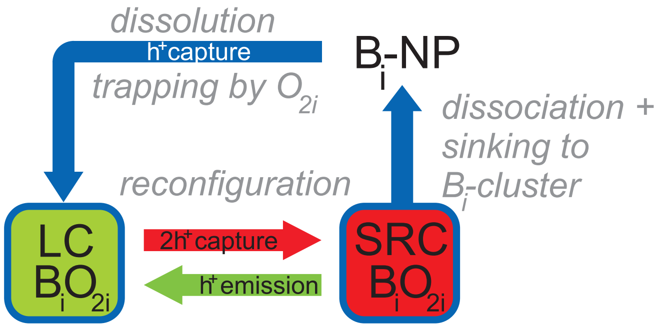

FIGURE 2.8: Schematic of the permanent deactivation of the defect complex and the destabilization within the B_iO_{2i} defect model [34].

2.3.3.3 The $\mathbf{B}_i\mathbf{B}_s\mathbf{O}_i$ model

The most recently revised model presented in 2013 by Voronkov and Falster [47], is a further modification of the model discussed in the previous section in terms of the nature of the latent centre LC. The central assumption is that the LC is formed due to two different frozen-in defects. One defect complex is frozen-in at relatively high temperatures around 600 °C and consists of a substitutional boron atom B_s and an interstitial oxygen atom O_i, i.e. B_sO_i. Naturally, the concentration of this defect complex is proportional to $[B_s]\times[O_i]$. The other defect complex is frozen-in at temperatures below 350 °C, and consists of an interstitial boron and oxygen atom, i.e. B_iO_i. This defect complex features a concentration proportional to $p_0\times[O_i]$. Upon lowering the temperature, it is assumed that the B_i component of the complex is gradually transferred from its initial trap (O_i) to other traps such as B_s and the B_sO_i complex. As it is assumed that B_iB_s is the dominant complex, its concentration is identical to the concentration of the precursor complex B_iO_i and thus proportional to $p_0\times[O_i]$.

$$[B_iB_s] \propto p_0 \times [O_i] \tag{2.2}$$

Additionally, the concentration ratio between the major complex B_iB_s and the minor complex $B_iB_sO_i$ is identical to the concentration ratio of the initial traps.

$$\frac{[B_iB_sO_i]}{[B_iB_s]} \propto \frac{[B_sO_i]}{[B_s]} \propto [O_i] \tag{2.3}$$

From these correlation one obtains for the concentration of the $B_iB_sO_i$ complex:

$$\begin{aligned} &\Rightarrow [B_iB_sO_i] \propto [B_iB_s] \times [O_i];\\ &\Rightarrow [B_iB_sO_i] \propto p_0 \times [O_i]^2 \end{aligned} \tag{2.4}$$

Hence, the $B_iB_sO_i$ complex shows the proper dependence of the effective defect concentration in the case of boron-only doped and boron- and phosphorus-doped Cz-Si. Therefore, within the model the $B_iB_sO_i$ complex is identified with LC and the subsequent SRC.

If additionally substitutional gallium atoms Ga_s are present within the material, the B_i atoms are transferred to three different traps: B_s, Ga_s and B_sO_i. Therefore, the concentration of B_iB_s is reduced compared to the case without gallium by the factor $[B_s]/([B_s]+[Ga_s])$ and as the $B_iB_sO_i$ complexes are in equilibrium with the B_iB_s complexes, their concentration is reduced by the same factor. Hence, the concentration of the $\mathrm{B}_i\mathrm{B}_s\mathrm{O}_i$ complex in boron- and gallium-doped Cz-Si is given by:

$$[B_iB_sO_i] \propto p_0 \times [O_i]^2 \times \frac{[B_s]}{[B_s]+[Ga_s]} \propto [B_s][O_i]^2 \tag{2.5}$$

since $p_0 = [\mathrm{B}_s] + [\mathrm{Ga}_s]$ in this case. The $\mathrm{B}_i\mathrm{B}_s\mathrm{O}_i$ model is therefore in agreement with the observations by Forster et al. [46].

The permanent deactivation within the $\mathrm{B}_i\mathrm{B}_s\mathrm{O}_i$ model is, as described before in the $\mathrm{B}_i\mathrm{O}_{2i}$ model, assumed to proceed via a dissociation of the SRC. In the current model, the B_i dissociates from the $\mathrm{B}_s\mathrm{O}_i$ complex. It is further assumed that the free interstitial boron-atoms B_i sink into boron nano-precipitates (B-NPs). For a diffusion-limited sinking of free B_i into the B-NPs, the rate constant γ describing the sinking process is given by:

$$\gamma = 4\pi \times D_i R_p N_p K^*/N_t, \tag{2.6}$$

with the diffusivity of the interstitial boron being D_i, the density and radius of the B-NPs being N_p and R_p, the dissociation constant K^* of the B_i from the $\mathrm{B}_s\mathrm{O}_i$ traps and N_t being the $\mathrm{B}_s\mathrm{O}_i$ trap density.

Within the model it is further assumed that the B-NPs are formed during the cooling of the ingot with a mechanism comparable to the formation of voids from vacancies. Starting from a homogeneous distribution of free B_i atoms upon cooling, the crystal nucleation and the growth to precipitates proceeds in a narrow temperature interval. Adapting the relations known from the void formation in silicon [11] one obtains for the B-NPs the following expressions:

$$R_p \propto [B_i]^{\frac{1}{2}} \times \left|\frac{d\vartheta}{dt}\right|_{\vartheta=\vartheta_n}^{-\frac{1}{2}} \tag{2.7}$$

and

$$N_p \propto [B_i]^{-\frac{1}{2}} \times \left|\frac{d\vartheta}{dt}\right|_{\vartheta=\vartheta_n}^{\frac{3}{2}}, \tag{2.8}$$

with ϑ being the temperature and $|d\vartheta/dt|_{\vartheta=\vartheta_n}$ being the cooling rate at the nucleation temperature ϑ_n. As can be seen from Eqn. 2.6, the sinking rate constant γ depends on the product of R_p and N_p. Hence, by inserting Eqns. 2.7 and 2.8 into Eqn. 2.6 we obtain:

$$\gamma \propto N_pR_p \propto \left|\frac{d\vartheta}{dt}\right|_{\vartheta=\vartheta_n} \equiv -q. \tag{2.9}$$

As the permanent recovery of the lifetime within the model is described by the sinking of the free B_i atoms into the B-NPs, the rate constant γ equals the recovery rate constant R_{de} determined from lifetime measurements. Hence, by investigating the rate constant R_{de} as a function of q we can either find further support for the model (if the linear dependence can be confirmed) or refute it. Our experimental investigation will be presented in section 5.1.

2.3.4 Impact of hydrogen

Very recent experimental results indicate, that the incorporation of hydrogen during sample processing plays an important role with regard to the permanent deactivation of the BO defect complex. Wilking et al. [48] observed that samples passivated with a hydrogen-rich SiN_x layer could only be permanently recovered, if a high-temperature step was applied. This high-temperature step was assumed to enable the diffusion of hydrogen from the dielectric layer into the silicon bulk. Within the same experiment, it was discovered that the density of the SiN_x layer and, hence, its ability to serve as a hydrogen source has also a direct impact on the deactivation rate constant. A less dense SiN_x layer releases less hydrogen into the silicon during high-temperature treatment and, accordingly, leads to a lower deactivation rate constant compared to a denser layer. Additionally, an Al_2O_3/SiN_x stack passivation with a sufficiently thick Al_2O_3 layer ($\sim$16 nm) was found to reduce the deactivation rate constant compared to a SiN_x single-layer. This observation was explained by the reduced transmissibility for hydrogen of thicker Al_2O_3 layers compared to thinner layers. Based on the experimental results, different interpretations on how the incorporated hydrogen interacts with the defect centre were presented.

Wilking et al. [49] described the interaction between the BO defect complex and hydrogen as follows:
At low temperatures, the hydrogen within the silicon is bound in molecules with impurities and other hydrogen atoms, e.g. B-H pairs [50]. These pairs split upon carrier injection [51] and free hydrogen becomes available for the defect passivation. However, at normal deactivation temperatures the main hydrogen species in *p*-type silicon is H^+, which features a very low diffusivity in oxygen-rich silicon [52]. Hence, it was concluded that H^+ cannot be the relevant species. However, if the hydrogen atoms are recharged in the presence of excess carriers to H^0, the diffusivity increases dramatically [53]. Hence, it was assumed that the deactivation of the BO defect complex is a hydrogen passivation of the complex by H^0 atoms.

Also Voronkov and Falster [54] very recently assumed that the permanent deactivation of the BO defect complex is accelerated in the presence of hydrogen, however, it occurs also in low-hydrogen silicon. According to Ref. [54] the influence of hydrogen on the defect reaction can be twofold. One explanation would be an indirect defect reaction with regard to the slow recombination centre (SRC): Hydrogen introduced into the material is assumed to partially passivate the fast recombination centre (FRC) or other defects which increases the electron concentration n during the deactivation process and, hence, increases the deactivation rate constant. Like Wilking et al., they also assumed that the main source of hydrogen at deactivation temperatures are B-H pairs which partially release some H^+ ions. As the dominating charge state of FRC is assumed to be positive (FRC^+) negative H^- ions are required to form H^-FRC^+ complexes. Accordingly, it is assumed that during deactivation, in the presence of excess carriers, H^+ ions are recharged into H^- ions. A second explanation would be a direct reaction with SRC: In that case they assumed that the negatively charged H^- ions directly bind to SRC^+ and form a H^-SRC^+ complex. The passivation would then proceed via a quick reconstitution of the defect complex into a recombination in-active form, or via a quick decomposition of the defect complex.

Within this thesis, we evaluate via a series of experiments the impact of hydrogen on the deactivation of the BO defect in detail. The results of this investigation can be found in section 5.2.

Chapter 3

Carrier lifetime in silicon

The quality of silicon material with regard to photovoltaic applications is characterized by the carrier lifetime. In this chapter, recombination processes which limit the carrier lifetime are introduced. Additionally, two lifetime measurement techniques are discussed.

3.1 Recombination mechanisms in crystalline silicon

A recombination event is a spontaneous transition of an electron from the conduction band into the valence band. It is the reverse process to the generation of free electron-hole pairs and, hence, leads to the restoration of the equilibrium after a perturbation, e.g. by illumination.

Two different kinds of recombination processes can be distinguished in crystalline silicon. First, there is intrinsic recombination which is always present and, hence, cannot be avoided. Two different mechanisms contribute to the intrinsic recombination: radiative band-to-band recombination and Auger recombination. On the other hand, in real crystals, extrinsic recombination exists besides the intrinsic recombination. The extrinsic recombination describes the recombination of electron-hole pairs via energy states in the silicon band gap. These states can, for example, be caused by crystallographic defects or impurity atoms such as iron, copper or defect complexes like the BO defect.

A measure of the recombination is the time span free electron-hole pairs can exist before they recombine. This time span is referred to as the carrier “lifetime”, which is more accurately defined as follows:

In thermal equilibrium, the mass action law of the carrier concentrations p_0 and n_0 for holes and electrons, respectively, holds: $n_0 \times p_0 = n_i^2$, with n_i being the intrinsic carrier concentration in crystalline silicon. If free carriers are generated, for example by illumination with photons of sufficiently high energy (i.e. $E > E_g$, with E_g the silicon band gap), this equilibrium is perturbed. After the light is switched off, the equilibrium is restored by electron-hole recombination. The net rate of recombination of the excess carriers U, defined as the difference between the total recombination rate U_{tot} and the thermal generation rate G_{th}, $U \equiv U_{tot} - G_{th}$, is given by the rate equation:

$$\frac{\partial \Delta n(t)}{\partial t} = -U(\Delta n, n_0, p_0), \tag{3.1}$$

with Δn being the concentration of free electron-hole pairs (excess carrier concentration) generated by the illumination.

The net recombination rate U is the sum of all recombination rates of the individual, independent recombination mechanisms. In the most simple case, U is proportional to Δn, which leads, according to Eqn. 3.1, to a simple mono-exponential decay of Δn with a time constant

$$\tau(n_0, p_0) \equiv \frac{\Delta n}{U(\Delta n, n_0, p_0)}, \tag{3.2}$$

which defines the carrier lifetime τ. Please note that in most cases the assumption of U being simply proportional to Δn does not hold and, hence, the carrier lifetime τ becomes dependent on Δn.

3.1.1 Intrinsic recombination

Radiative band-to-band recombination Radiative band-to-band recombination is the inverse process to the optical generation of electron-hole pairs. The energy which is released during the electron-hole recombination generates a photon with a wavelength corresponding to the silicon band gap. Comparable to the chemical reaction kinetics, the rate of recombination per unit volume depends on the number of collisions between the reactants, in this case holes and electrons, and a recombination coefficient B. The number of collisions itself depends on the densities of the participating species. Hence, the net radiative recombination rate U_{rad} can be written as:

$$U_{rad} = B(np - n_i^2) \tag{3.3}$$

which leads according to Eqn. 3.2 to a lifetime for this recombination process of

$$\tau_{rad} = \frac{1}{B(n_0 + p_0) + B\Delta n}, \tag{3.4}$$

using $n = n_0 + \Delta n$ and $p = p_0 + \Delta p$ for the total electron and hole concentrations. On lowly doped silicon, Trupke et al. [55] determined the recombination coefficient at 300 K to be $B_{low} = 4.73 \times 10^{-15}\,\mathrm{cm}^3/\mathrm{s}$. For higher carrier concentrations, the influence of the

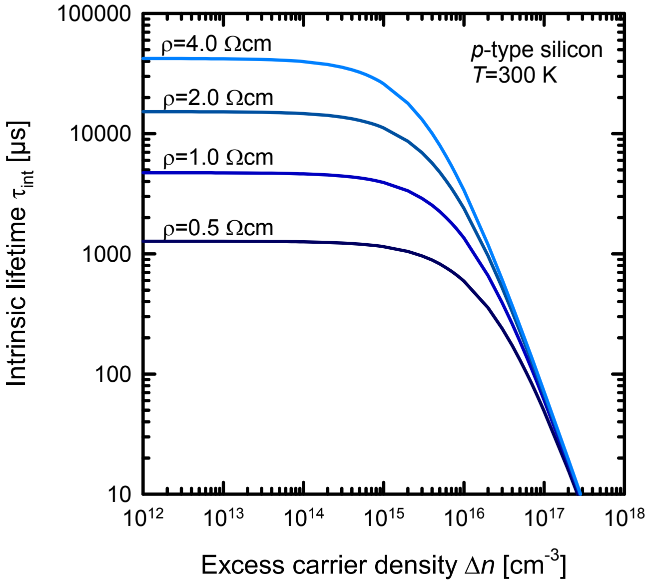

FIGURE 3.1: Injection-dependent intrinsic lifetime [60] for four different base resistivities between 0.5 Ω cm and 4.0 Ω cm.

screening of the Coulomb attraction between the holes and electrons has to be taken into account. Altermatt et al. [56] modelled the screening effects of the Coulomb interaction at high carrier concentrations for various injection densities and doping concentrations and determined a pre-factor $B_{rel}(\Delta n, p_0)$, relative to B_{low}, so that $B = B_{rel} \times B_{low}$.

Auger recombination Auger recombination involves three particles. The energy which is released during the recombination of an electron-hole pair is transferred either to another electron (eeh-process) or another hole (ehh-process). As for the radiative recombination, the Auger net recombination rate U_{Auger} is proportional to the densities of the participants for each of the two processes (eeh) and (ehh). U_{Auger} can be expressed as

$$U_{Auger} = C_n(n^2p - n_i^2 n_0) + C_p(np^2 - n_i^2 n_0), \tag{3.5}$$

with $n = n_0 + \Delta n$ and $p = p_0 + \Delta p$ the total electron and hole concentrations and the Auger coefficients C_n and C_p for the two processes (eeh) and (ehh), respectively.

However, the Auger recombination does not proceed with non-interacting quasi-free particles. Therefore, Hangleiter and Häckler [57] introduced enhancement factors of the Auger coefficients based on the influence of the Coulomb interaction, so that new coefficients can be calculated as follows: $C_p^* = g_{ehh} \times C_p$ and $C_n^* = g_{eeh} \times C_n$. An empirical parameterization of the enhancement factors was derived later on for a wide temperature range between 70 K and 400 K by Altermatt et al. [58] and Schmidt et al. [59].

Intrinsic lifetime The sum of the radiative recombination rate U_{rad} and the Auger recombination rate U_{Auger} add up to the intrinsic recombination rate U_{int}, which results in the intrinsic lifetime τ_{int}. In terms of the corresponding lifetimes, the intrinsic lifetime can be calculated according to:

$$\frac{1}{\tau_{int}} = \frac{1}{\tau_{Auger}} + \frac{1}{\tau_{rad}}. \tag{3.6}$$

In a more recent work, Richter et al. [60] introduced an empirical parameterization of the intrinsic lifetime limit τ_{int} for n- and p-type silicon at 300 K. Based on lifetime measurements, they developed an empirical parameterization which accounts for the Coulomb enhancement of the Auger coefficients as well as for the radiative recombination. In Figure 3.1, the intrinsic lifetime in boron-doped p-type silicon according to Richter's parameterization for a base resistivity range between 0.5 Ω cm and 4.0 Ω cm is displayed.

3.1.2 Extrinsic recombination

In the previous section, unavoidable recombination in a perfect silicon crystal was discussed. However, in real crystals, impurities and crystallographic defects lead to localized energy states in the silicon band gap which can act as efficient recombination centres. If the recombination is dominated by the recombination via a single monovalent energy level, the net recombination rate can be described according to Shockley, Read and Hall (SRH) [61, 62] by

$$U_{SRH} = \frac{np - n_i^2}{\tau_{p0}(n + n_1) + \tau_{n0}(p + p_1)} \tag{3.7}$$

with the capture time constants τ_{p0} and τ_{n0} for holes and electrons, respectively. The capture time constants are related to the capture cross sections σ_p and σ_n of the defect for both species according to: $\tau_{n0} = 1/(\sigma_n v_{th} N_t)$ and $\tau_{p0} = 1/(\sigma_p v_{th} N_t)$, with the thermal carrier velocity v_{th} and the defect concentration N_t. The statistical factors n_1 and p_1 are often referred to as "SRH densities" and describe the electron and hole densities when the energy of the Fermi-level coincides with the energy level of the recombination centre E_t:

$$n_1 = N_c \times \exp\left(-\frac{E_c - E_t}{k_b T}\right) \quad \text{and} \quad p_1 = N_v \times \exp\left(-\frac{E_t - E_v}{k_b T}\right). \tag{3.8}$$

N_c and N_v are the effective densities of states in the conduction and valence band, respectively. E_c and E_v are energy levels describing the lower/upper band edge of the conduction/valence band, respectively. T is the absolute temperature and k_b is the Boltzmann constant. Using Eqn. 3.2 and under the assumption that the charge neutrality is fulfilled, the recombination rate can be transferred to the characteristic

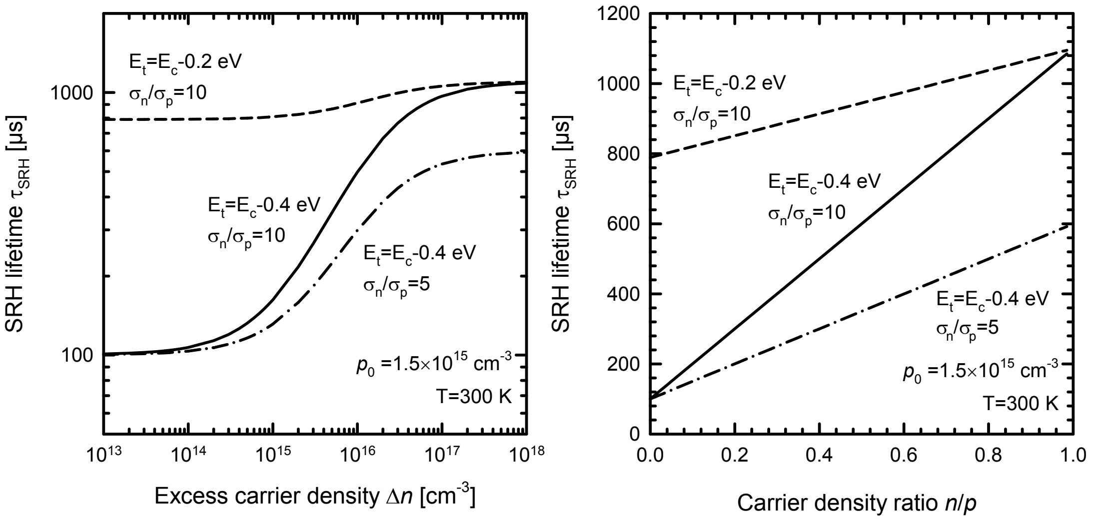

FIGURE 3.2: Injection-dependent SRH lifetime plotted versus Δn (left) and versus n/p (right). An example for different capture cross section ratios σ_n/σ_p and different energy levels of the trap E_t is shown.

lifetime of this recombination process:

$$\tau_{SRH} = \frac{\tau_{p0}(n_0 + n_1 + \Delta n) + \tau_{n0}(p_0 + p_1 + \Delta n)}{n_0 + p_0 + \Delta n}. \tag{3.9}$$

Recently, Murphy et al. [63] presented an alternative notation of this lifetime. For p-type materials and under the assumption that the defect density complies with the condition $N_t << p_0$, the carrier lifetime can be expressed as

$$\tau_{SRH} = \tau_{n0}\left[1 + \frac{Qn_1}{p_0} + \frac{p_1}{p_0} + X\left(Q - \frac{Qn_1}{p_0} - \frac{p_1}{p_0}\right)\right], \tag{3.10}$$

with $Q \equiv \tau_{p0}/\tau_{n0}$ and $X \equiv n/p$.

Equation 3.10 clearly shows that under the mentioned assumption, the SRH lifetime is a linear function of the ratio of the minority carrier density divided by the majority carrier density, i.e. n/p. In Figure 3.2, the SRH lifetime is plotted versus the excess carrier density Δn on the left and versus n/p on the right. An example for two energy levels $E_t = E_c - 0.2\,\text{eV}$ (dashed line) and $E_t = E_c - 0.4\,\text{eV}$ (solid line) and capture cross section ratio of $\sigma_n/\sigma_p = 10$, as well as an example for a ratio of $\sigma_n/\sigma_p = 5$ (dash-dotted line) is shown. For these examples, a fixed capture time constant $\tau_{n0} = 100\,\mu\text{s}$ is chosen. Comparing the curve progression in both plots in Fig. 3.2, in the classical representation the SRH-lifetime features a more complex curve shape than in the representation introduced by Murphy et al.. Hence, when evaluating measured lifetime curves, the new representation allows a faster conclusion if the lifetime is limited by a single SRH defect centre or if additional recombination processes influence the lifetime.

3.1.3 Effective lifetime

Within the silicon bulk, all recombination processes mentioned above occur simultaneously. Hence, the net recombination rates of all individual (intrinsic and extrinsic) processes have to be added up to account for all processes. Thus, the total bulk lifetime τ_b can be calculated according to

$$\frac{1}{\tau_b} = \frac{1}{\tau_{Auger}} + \frac{1}{\tau_{rad}} + \frac{1}{\tau_{SRH}} = \frac{1}{\tau_{int}} + \frac{1}{\tau_{SRH}}. \tag{3.11}$$

The *measured* effective lifetime τ_{eff} is additionally influenced by the finite dimension of *real* lifetime samples. At the samples' edges and surfaces the lattice structure is interrupted which leads to energy states in the band gap and, hence, to an increased recombination. In modern silicon, the recombination at the surface dominates the total recombination if these states are not sufficiently passivated. However, with techniques such as the deposition of silicon nitride or aluminium oxide layers, the recombination at the surfaces can be sufficiently suppressed. In the case of sufficiently small surface recombination velocity (SRV) S, the measured effective lifetime can be approximated by [64]

$$\frac{1}{\tau_{eff}} = \frac{1}{\tau_b} + \frac{2S}{W} \tag{3.12}$$

with the sample thickness W. According to Sproul [64], this expression is a good approximation for sufficiently low and equal recombination velocities at the front and rear side of the sample ($S = S_{\text{front}} = S_{\text{rear}}$). It is accurate within 4% for $SW/D < 0.25$, with D being the diffusion constant of the excess carriers.

3.2 Lifetime measurement techniques

3.2.1 Photoconductance-based lifetime measurements

A widely used instrument to measure the effective lifetime in silicon wafers is the WCT-120 lifetime tester from Sinton Instruments. The method applied is based on time-dependent measurements of the photoconductance of a silicon sample. For this purpose, a calibrated radio frequency (rf) bridge circuit is employed. The rf-coil, which works at a frequency of 10.7 MHz, induces an eddy current in the silicon sample. According to Lenz's law, this eddy current induces an additional voltage in the rf-coil, which is dependent on the sample's conductance. This additional voltage is measured. Once the system is calibrated to silicon wafers with independently determined conductance values, this setup allows the determination of the absolute conductance of a test sample. In Fig. 3.3, a schematic of the setup is shown. The coil has a diameter of 18 mm, thus,

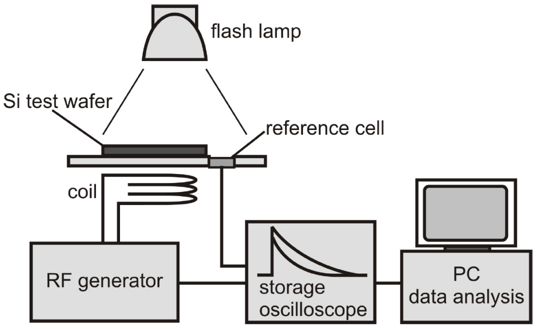

FIGURE 3.3: Schematic of the setup used for the photoconductance-based lifetime measurements in this thesis [65].

all measurements are averaged over the coil area of $\sim$250 mm^2.
To determine the effective lifetime τ_{eff} of a silicon sample, the change in conductance upon illumination of the sample with a flash lamp is measured. In principle, the conductance σ of the sample depends on the product of the carrier concentration and the respective carrier mobility:

$$\sigma = q_e \int_0^W (n\mu_n + p\mu_p)dx. \tag{3.13}$$

q_e is thereby the elementary charge, W the sample thickness and $n\mu_n$ and $p\mu_p$ the product of electron and hole concentrations with their respective mobilities. Please note that the mobility $\mu_{n/p}$ depends on the carrier concentrations. During each lifetime measurement the sample is illuminated with a flash lamp which increases the excess carrier density and hence a photoconductance $\Delta\sigma$ is generated. Assuming that the relations $n = n_0 + \Delta n$ as well as $p = p_0 + \Delta n$ apply, it is convenient to separate the total conductance σ into the dark conductance σ_0, which corresponds to the conductance of the base in darkness, and the photoconductance $\Delta\sigma$, i.e. $\sigma = \sigma_0 + \Delta\sigma$.

For a homogeneous generation of excess carriers, the photoconductance is given according to Eqn. 3.13 by

$$\Delta\sigma \approx qW(\mu_n + \mu_p)\Delta n_{avg}, \tag{3.14}$$

with Δn_{avg} being the average excess carrier density induced by the homogeneous generation. Within the setup, the homogeneous photogeneration is realized by a long-pass filter in front of the flash lamp with a cut-off wavelength of 700 nm. To calculate Δn_{avg}, the sum of the carrier mobilities $\mu_n + \mu_p$ has to be known. Here, a semi-empirical expression is used, which holds for exclusively boron- or phosphorus-doped silicon [66].

The time dependence of the excess carrier density is given by the continuity equation:

$$\frac{\partial \Delta n(x,t)}{\partial t} = G(x,t) - U(x,t) + \frac{1}{q_e}\nabla J(x,t). \tag{3.15}$$

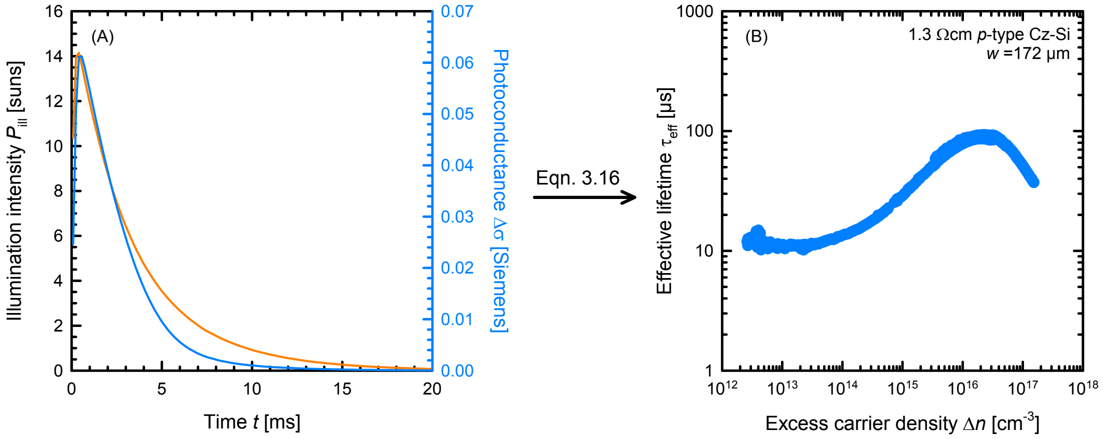

FIGURE 3.4: (A) Illumination intensity P_{ill} and photoconductance $\Delta\sigma$ plotted versus time t, during a QSSPC measurement using the WCT-120 lifetime tester. (B) Injection-dependent effective lifetime τ_{eff} plotted versus the excess carrier density Δn, extracted from photoconductance and illumination intensity measurements using Eqn. 3.16.

Here, G is the generation rate, U is the recombination rate and J is the current density. If the carrier distribution upon illumination is homogeneous, the divergence of the current density J vanishes. Additionally, the recombination rate U can be written according to Eqn 3.2 as $U = \Delta n/\tau_{eff}$ and the *generalized* expression for the effective lifetime τ_{eff} can be determined to [67]:

$$\tau_{eff} = \frac{\Delta n}{G - \frac{\partial \Delta n}{\partial t}}. \tag{3.16}$$

Hence, apart from the change in the excess carrier concentration, which is determined by the change in the photoconductance, the generation rate G has to be known. Within the setup shown in Fig. 3.3, the generation rate is determined using a reference solar cell located next to the sample under investigation. The shot-circuit current I_{sc} of this cell is known to depend linearly on the light intensity P_{ill}, i.e. $I_{sc} = c \times P_{ill}$. To increase the accuracy of the intensity measurement, the reference is connected to a small resistor, so that a voltage drop over this resistor can be measured. Using a calibration factor which accounts for the difference in reflectance and transmission between the reference cell and the sample under investigation, the generation rate G can be directly determined from the measured light intensity. Hence, all input parameters to Eqn. 3.16 are determined and the injection-dependent lifetime can be calculated. Figure 3.4 shows a typical lifetime measurement.

If the carrier lifetime is much shorter than the decay time constant of the flash light, the average excess carrier density is in equilibrium with the illumination at every point in time and a quasi-steady-state condition (often referred to as QSSPC measurement) is established. In this case, the effective lifetime is simply given by $\tau_{eff} = \Delta n/G$.

For high carrier lifetimes, i.e. when the lifetime is much longer than the decay time constant of the light flash, a good alternative to the technique mentioned above is the photoconductance decay (PCD) technique. In this case, the change of the photoconductance is analysed after the light flash terminated. If $G = 0$, Eqn. 3.16 simplifies to:

$$\tau_{eff} = -\frac{\Delta n}{\frac{\partial \Delta n}{\partial t}} \tag{3.17}$$

No information about the optical properties of the sample under investigation is needed in this case. However, as the differential of the signal is analysed, this technique is prone to noise.

Error sources of photoconductance-based lifetime measurements According to McIntosh and Sinton [68] the following factors are most relevant for an accurate measurement:

- the calibration of the rf-bridge circuit
- the calibration of the reference cell
- the uncertainty in the width of the quasi-neutral base
- the measurement uncertainties in the voltage of the rf-coil
- the uncertainty in the sum of the carrier mobilities
- the uncertainty in the base doping density

Accounting for all these uncertainties, they presented two examples for two different lifetime measurements, one in a low-lifetime range, obtained using the QSSPC method, and one in a high-lifetime range, obtained using the PCD method. For the QSSPC measurement they determined a relative uncertainty of 10.9 % and for the PCD measurement 8.6%. The impact of the uncertainty in the sum of the carrier mobilities is quite severe. If this error source was excluded, the relative uncertainty was more than halved.

Please note that the uncertainty described above is the *total* uncertainty of the measured lifetime, which is subdivided in systematic and statistical errors. When comparing lifetime measurements with the same lifetime tester, e.g. at different processing stages, the systematic error is of minor importance. The statistical error between those measurements, however, is below 5 % [69].

3.2.2 Photoluminescence-based lifetime measurements

Within this thesis, spatially resolved lifetime measurements were performed using the photoconductance-calibrated photoluminescence imaging (PC-PLI) method introduced by Herlufsen et. al. [70] in 2008. In the following, this method shall be briefly outlined:

In Fig. 3.5, a schematic of the PC-PLI setup is shown. The sample under investigation is placed on a calibrated rf-bridge circuit as described in the previous section. However, in this case, the excitation of excess carriers is not realized by a flash lamp, but by a laser ($\lambda = 808\,\mathrm{nm}$, $P = 30\,\mathrm{W}$). The laser beam is widened and homogenized in an optical system, so that a complete wafer ($156\times156\,\mathrm{mm}^2$) can be homogeneously illuminated. A reference cell next to the rf-coil is used to measure the photon-flux Φ. The PL signal is detected by a Si CCD camera mounted above the wafer. To prevent laser reflections from the sample to penetrate into the CCD camera, a set of long pass filters is mounted in front of the camera.

The method exploits the fact that the intensity of the photoluminescence signal I_{PL} of the silicon wafer is proportional to the radiative recombination rate U_{rad}. Hence, using Eqn. 3.3 for p-type silicon, with the doping density N_A, a quadratic dependence of I_{PL} on the excess carrier density Δn is obtained:

$$I_{PL} \propto U_{rad} \approx B \times \Delta n(\Delta n + N_A). \tag{3.18}$$

Under steady-state illumination conditions, the effective lifetime is then again given in accordance with Eqn. 3.16 by $\tau_{eff} = \Delta n/G$. The generation rate G in the sample is

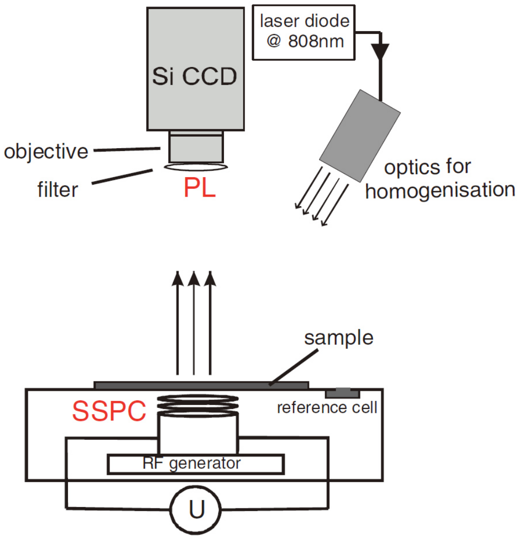

FIGURE 3.5: Schematic of the PC-PLI setup used in this thesis [70].

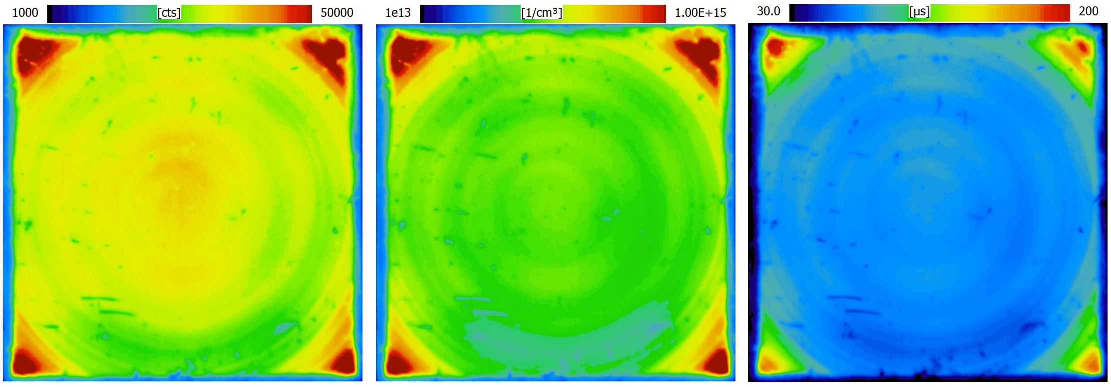

FIGURE 3.6: PC-PLI measurement of a boron-doped Cz-Si sample ($156\times156\,\mathrm{mm}^2$) with a base resistivity of $1.0\,\Omega\,\mathrm{cm}$ in the fully degraded state. The PL-signal (left), the excess carrier density Δn (centre) and the effective lifetime τ_{eff} (right) are shown.

obtained by correcting the measured photon flux Φ for the reflectivity of the sample at the laser wavelength $R_{f,808\,\mathrm{nm}}$. As the penetration depth of the laser used in this setup is $\sim 12.7\,\mu\mathrm{m}$ a good approximation for G is:

$$G = \Phi(1 - R_{f,808\,\mathrm{nm}}) \times \frac{1}{W} \tag{3.19}$$

To calibrate the measured PL signal to the excess carrier density Δn, an eddy current measurement under illumination is performed, as described in the previous section. The eddy current measurement is averaged over the coil area of $\sim 250\,\mathrm{mm}^2$, hence, the PL signal has to be averaged over the same area.

In Fig. 3.6, an example of a PC-PLI measurement at a laser intensity of 0.4 suns, on a boron-doped Cz-Si lifetime sample is shown. The ring structure indicates an influence of the axially symmetric Czochralski process on the effective lifetime.

Error sources of PC-PLI measurements According to Herlufsen et al. [70, 71] the main error sources of the PC-PLI measurements are:

- the increasing sample temperature during laser illumination especially at high light intensities
- the influence of reabsorption of the photons in the silicon, which is relevant for inhomogeneous depth profiles of the excess carrier density
- the influence of the areas over which the PL signal and the conductance signal are averaged, as for samples with very inhomogeneous lifetime distributions the $I_{PL}(\Delta n)$ calibration curve is strongly influenced by these areas

As the measurement is based on the calibration using a photoconductance-based setup, additionally, the same error sources related to the eddy current measurement, as listed in the previous section, are also relevant for the PC-PLI measurement.

For *standard* PC-PLI measurements on mono-crystalline silicon lifetime samples the uncertainties due to the increasing temperature, the photon reabsorption as well as the averaging area are only small (i.e. $\leq 10\%$). A comparison between injection-dependent lifetime measurements using the PC-PLI setup and the WCT-120 setup revealed a very good agreement [70] suggesting comparable uncertainties.

Chapter 4

Grown-in defect concentrations and their manipulation

In the first part of this chapter, grown-in boron-oxygen-related defect centres are investigated. First, the influence of the crystal growth conditions on the maximum effective defect concentration N_d^* is studied. Additionally, the equilibrium defect concentration after prolonged annealing at intermediate temperatures between 200 °C and 300 °C is examined.

Finally, lifetime limitations in Czochralski-grown silicon are studied which may arise solely due to the presence of oxygen, independent of the doping type. In this experiment, phosphorus-doped silicon is used.

4.1 Influence of the crystal growth conditions on the BO defect concentration

For the investigation of the influence of the growth conditions on the maximum effective defect concentration N_d^*, wafers from three different crystals are analysed. The three crystals (205 mm in diameter and ~1.6 m in length) are crystallized via the Czochralski process and fully characterized with regard to the boron (via resistivity measurements), oxygen and carbon concentrations (via FTIR measurements using the "new ASTM" standard [72]). An overview of the characteristics of these three crystals is given in Tab. 4.1. Additionally, the oxygen-induced stacking fault (OISF) ring [73] is determined to separate between the region with self-interstitials as predominant point defects and the region with vacancies as predominant point defects. Apart from different positions along the crystal axis, i.e. different wafers, different lateral positions, i.e. samples cut

TABLE 4.1: Boron [B$_s$], oxygen [O$_i$] and carbon concentrations [C$_s$] of the three investigated Cz-Si crystals.

Crystal #	1	2	3
[B$_s$] [10^{15} cm^{-3}]	11.4 – 15.1	7.6 – 8.6	8.6 – 9.8
[O$_i$] [10^{17} cm^{-3}]	7.5 – 8.2	7.6 – 8.7	8.4 – 8.91
[C$_s$] [10^{16} cm^{-3}]	0.1 – 1.4	2.3 – 3.3	2.5 – 4.2

from different positions on a single wafer, are investigated. The three crystals are cut into 156×156 mm^2 pseudo-square wafers. Wafers from three different positions along the crystal axis are investigated: seed end (approx. 10 mm from the top wafer), centre (810 mm from the top), and tail end (1590 mm from the top). One wafer from each position is cut into 30×30 mm^2 samples, which are then processed into lifetime samples; another wafer is processed at full size.

In order to investigate the distribution of the BO-related defects, the effective carrier lifetime $\tau(\Delta n)$ is measured after light exposure [$\tau_d(\Delta n)$] for more than 24 hours at a light intensity of $P_{ill} = 10\,\mathrm{mW/cm^2}$, using a halogen lamp, at room temperature, and after annealing [$\tau_0(\Delta n)$] for 10 min at a temperature of 200 °C in the dark. Assuming all other recombination channels to be unaffected by the anneal/degradation cycle, the lifetimes $\tau(\Delta n)$ can be converted into the effective defect concentration N_d^* using Eqn. 2.1.

Figure 4.2 shows in the top row the measured effective lifetimes after illumination (i.e. after complete degradation) τ_d and after annealing in darkness (i.e. after complete

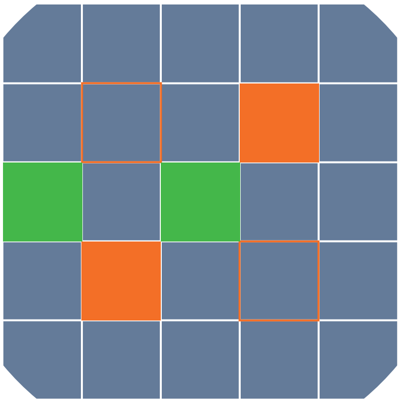

FIGURE 4.1: Cut pattern of the wafers. The orange marked samples are used to study the variation along the crystal axis (open squares: P-diffused samples, full squares: as-grown samples). The green marked samples are used to study the lateral variation (as-grown).

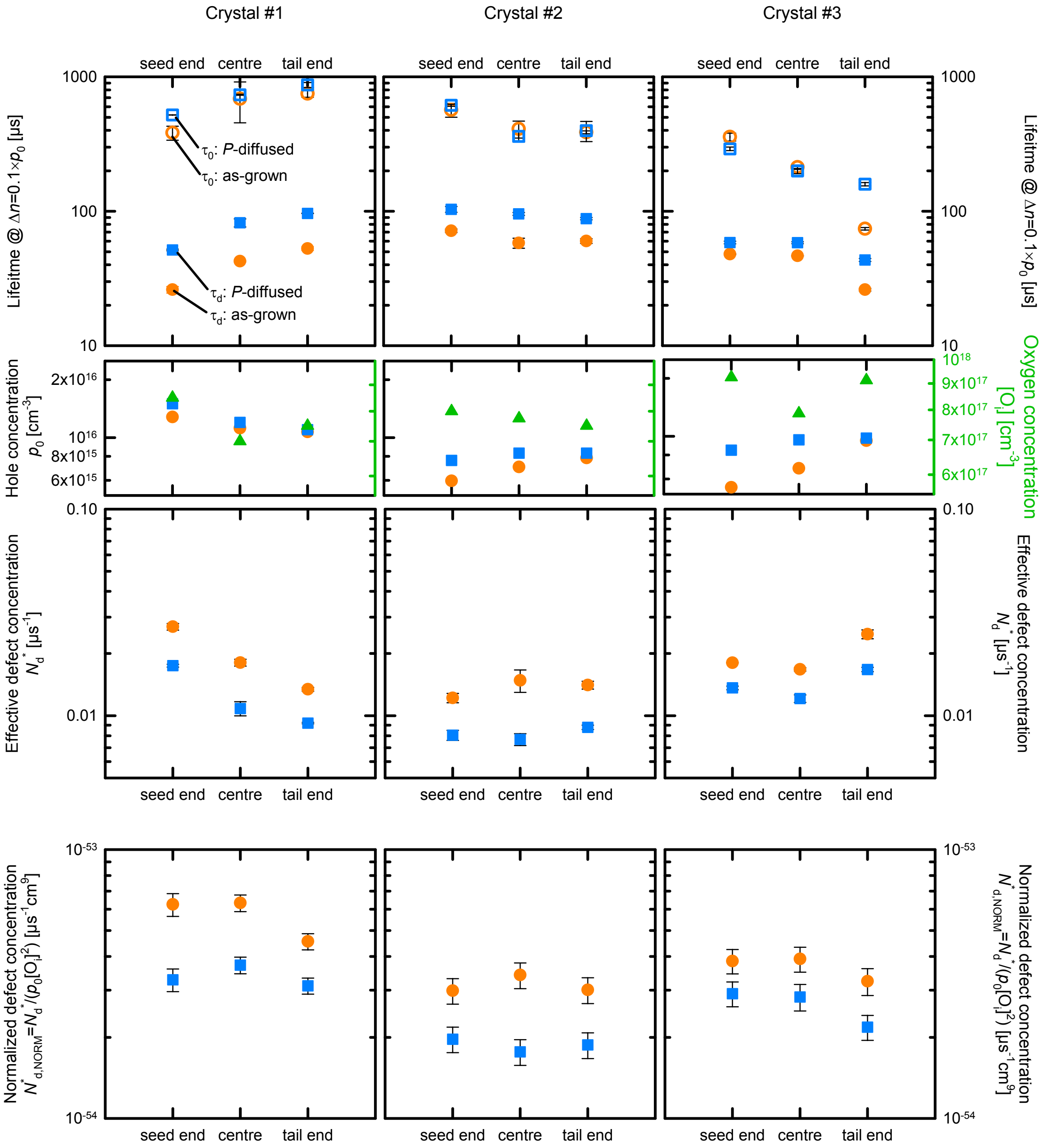

Figure 4.2: Effective lifetimes after illumination τ_d (full symbols) and after annealing in darkness τ_0 (open symbols) for crystal #1, #2 and #3 in the top row from left to right, respectively. Orange circles correspond to as-grown samples, while blue squares correspond to the samples after P-diffusion. The hole and oxygen concentrations are displayed in the second row (green triangles correspond to the oxygen concentration). In the third row, the effective defect concentration N_d^* of the three crystals is shown. In the bottom row, the defect concentration normalized to $p_0 \times [\mathrm{O}_i]^2$, $N_{d,NORM}^*$, is displayed.

annihilation of the BO centre) τ_0 for all investigated crystals. The lifetimes stated are determined at an excess carrier density $\Delta n = 0.1 \times p_0$, with Δn being the excess carrier density and p_0 being the hole concentration in darkness. The error bars indicate the variations of the lifetime values for two identically processed samples of each position. For crystal #1, τ_d increases from $33\,\mu$s to $68\,\mu$s and from $52\,\mu$s to $97\,\mu$s from seed to

tail end, for as-grown and P-diffused samples, respectively. The lifetime after annealing in darkness τ_0 increases as well from seed to tail end, from $384\,\mu$s to $750\,\mu$s and from 521 to $871\,\mu$s, for as-grown and P-diffused samples, respectively. While the lifetimes of both sample types from crystal #2 remain almost unchanged from seed to tail end ($\tau_d \approx 65\,\mu$s for as-grown samples and $\tau_d \approx 95\,\mu$s for P-diffused samples), a decrease of the effective lifetimes for both sample types can be observed for crystal 3. The lifetime τ_d decreases from $48\,\mu$s to $26\,\mu$s and from $59\,\mu$s to $43\,\mu$s, for as-grown and P-diffused samples, respectively, and the lifetime τ_0 decreases from $357\,\mu$s to $74\,\mu$s and from $292\,\mu$s to $159\,\mu$s, for as-grown and P-diffused samples, respectively. For all investigated crystals and crystal positions the degraded lifetimes τ_d of the as-grown samples are a factor 0.6 to 0.8 lower than τ_d of the samples which underwent the additional high-temperature step. This finding corresponds well with previously published results by Bothe et al. [74] and can be attributed to the fact that the cooling subsequent to the high-temperature treatment is faster than the cooling of the crystal directly after crystallization.
From the measured lifetime data, the effective BO defect concentration N_d^* is calculated using Eqn. 2.1. However, in order to compare different crystal positions of a single crystal correctly, it is imperative to consider the changing value of both hole and oxygen concentrations along the crystal axis. The measured hole and oxygen concentrations at each position are displayed in the second row in Fig. 4.2. As was shown by Lim et al. [45], N_d^* increases linearly with the hole concentration p_0 and according to Schmidt et al. [24] quadratically with regard to the interstitial oxygen concentration $[\mathrm{O}_i]$ (for $[\mathrm{O}_i]$ ranging between $3 \times 10^{17}\,\mathrm{cm}^{-3}$ and $1 \times 10^{18}\,\mathrm{cm}^{-3}$). Taking these dependencies into account, N_d^* can be normalized to the product $p_0 \times [\mathrm{O}_i]^2$. This normalized effective defect concentration $N_{d,NORM}^*$ is shown in Fig. 4.2 in the bottom row. The indicated errors of $N_{d,NORM}^*$ are calculated by means of error propagation assuming an accuracy of 10 % for the hole concentration p_0, an error of $2.5\times10^{16}\,\mathrm{cm}^{-3}$ (=0.5 ppma) for the measured oxygen concentration $[\mathrm{O}_i]$, as well as the lifetime uncertainties as displayed in the top row of Fig. 4.2.

As shown in Fig. 4.2, the normalized defect concentration of as-grown and P-diffused samples does not change from seed to tail end for crystals #2 and #3. However, for crystal #1, the normalized defect concentration in the as-grown state is reduced by almost 30 % at the tail end compared to seed end and centre. This fact might be due to the enhanced cooling rate after crystallization of the crystal at the tail end compared to other crystal positions. The observation that no such reduction is observed in crystals #2 and #3 could be due to the fact that the absolute values of the normalized N_d^* are already well below the maximum defect concentration defined by the crystal cooling. It has to be noted that this interpretation is solely based on a single data point. For an unambiguous clarification further investigations would be needed.

In general, the absence of the variation in the normalized N_d^* indicates that the variation of the lifetimes after illumination τ_d at different positions of the crystals can be attributed to the variation of the hole and oxygen concentrations along the crystal axis. An influence of the crystal cooling cannot completely be ruled out, however, following the above discussion, in materials with low BO defect concentrations (possibly for normalized defect concentrations below $N_{d,NORM}^* = 4 \times 10^{-54}\,\mu\text{s}^{-1}\text{cm}^9$) it is not experimentally observed. Comparing the values of the normalized effective defect concentration of different crystals, the observed values of both sample types are considerably reduced for crystals #2 and #3 compared to crystal #1. For crystals #2 and #3 the as-grown samples are reduced to ∼60 % and the P-diffused samples to ∼67 % of the values determined for crystal #1. This difference might result from the increased carbon concentration in crystal #2 and #3 compared to crystal #1 (see Table 4.1). However, such a relation between the reduced defect concentration and the increased carbon concentration contradicts the findings by Rein et al. [23] and Schmidt et al. [26], who did not find a correlation between the carbon concentration $[\text{C}_s]$ and the effective defect concentration N_d^* for a $[\text{C}_s]$-range between $5 \times 10^{15}\,\text{cm}^{-3}$ and $5 \times 10^{16}\,\text{cm}^{-3}$. To clarify this point, further investigations are needed.
Apart from investigating the variation of the effective defect concentration at different crystal positions, the lateral variation at one crystal position is also examined. By comparing the normalized effective defect concentration $N_{d,NORM}^*$ from samples taken from the centre and the edge of each wafer, no lateral variation is observed for any of the investigated crystals.

Importantly, the oxidation of wafers from crystal #3, and the related appearance of OISF rings, reveal that there is a transition from a vacancy-rich region in the centre to

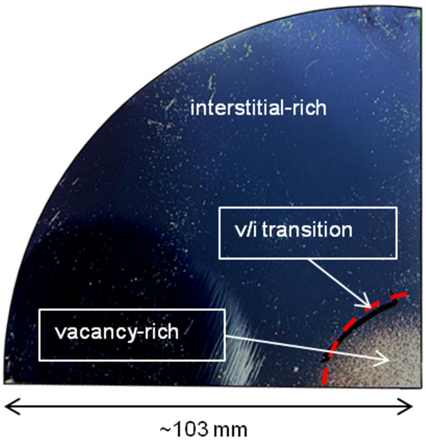

Figure 4.3: Photo of a sample (quarter of a crystal slice) taken from the seed end of crystal #3. An oxidation step is performed in order to reveal the OISF ring after selective etching. The red dashed line marks the transition between the vacancy-rich and the interstitial-rich region.

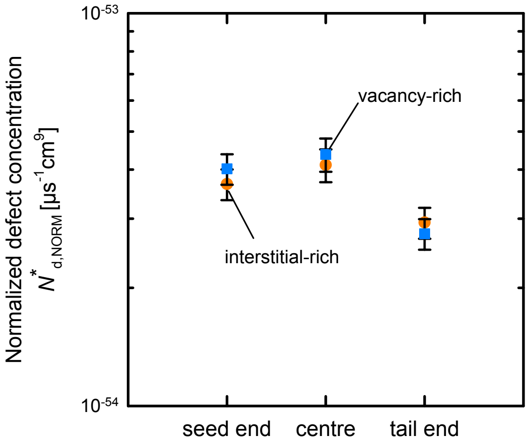

FIGURE 4.4: Normalized effective defect concentration $N^*_{d,NORM}$ of crystal 3 for centre positions (vacancy-rich regions) and edge positions (interstitial-rich regions).

an interstitial-rich region at the edge of the ingot along the entire crystal length. Figure 4.3 shows an example of the OISF ring structure after oxidation of a sample taken from the seed end of crystal #3. In Fig. 4.4, the normalized effective defect concentrations $N^*_{d,NORM}$ determined in the vacancy- and interstitial-rich regions at different crystal positions of crystal #3 are compared. Considering the indicated error bars, the values in interstitial-rich and vacancy-rich regions at each crystal position are identical. This allows the conclusion that the formation of the BO-related defect is *not influenced* by the presence of either vacancies or self-interstitials. This finding corresponds well with results published by Rein et al. [23], where the influence of vacancy-type intrinsic point

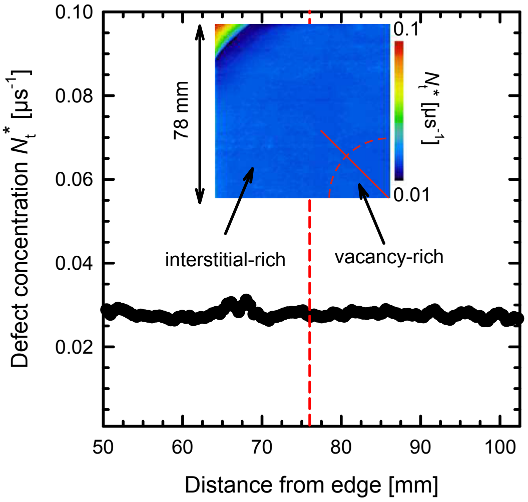

FIGURE 4.5: Line-scan of an effective defect concentration image, shown in the inset, of a sample taken from the seed end of crystal 3. The line-scan is along the indicated solid red line. The red dashed line marks the transition between the vacancy-rich and the interstitial-rich region. The defect concentration is determined at an injection level of $\Delta n \approx 1.4 \times 10^{14}\,\text{cm}^{-3}$.

defects, after a special thermal treatment, was investigated. Figure 4.5 shows exemplarily a line-scan of an effective defect concentration image calculated from two PC-PLI images of a sample taken from the seed end of crystal #3. The indicated line-scan covers the transition between the vacancy-rich and the interstitial-rich region as can be seen by comparing the inset with Fig. 4.3. As already discussed, no lateral variation can be observed. Moreover, lateral measurements of the hole and oxygen concentrations reveal that the concentrations remain almost unchanged in the transition region.

4.2 Determination of the equilibrium BO defect concentration after prolonged annealing

Within the $B_iB_sO_i$ model [47], upon cooling the sample free B_i atoms are captured by the B_sO complex to form the latent form of the defect complex (LC). The free B_i atoms are supplied by boron nano-precipitates (B-NPs) which are formed during the cooling of the ingot directly after crystal growth or during the cooling after a high-temperature process step. The exchange of B_i between the B_sO traps and the B-NPs is assumed to be frozen-in at some temperature.

In the following, the equilibration between the B_sO traps and the B-NPs is investigated in a temperature interval between 200 °C and 300 °C by applying a prolonged annealing for 50 h to lifetime samples with different resistivities (see schematic in Fig. 4.6). For this experiment, Cz-Si materials with different base resistivities between 0.5 Ω cm and 2.5 Ω cm, are chosen. The material is cut into samples of 2.5×2.5 cm^2 in size. Sample processing includes the removal of the surface damage using KOH. After sample cleaning in a standard RCA cleaning sequence, all samples undergo a phosphorus diffusion (847 °C for 51 min). Subsequently, the phosphosilicate glass (PSG) and the n^+-region is removed using hydrofluoric acid (HF) and KOH, respectively. After another RCA cleaning, the

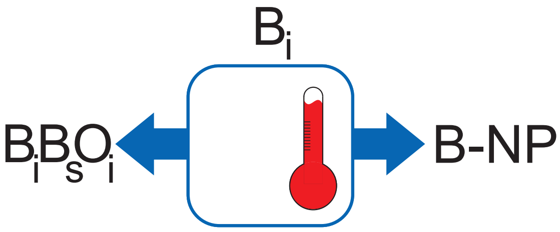

FIGURE 4.6: Schematic of the equilibration process between the two traps for the interstitial boron atom B_i: the B_sO complex and the boron nano-precipitates (B-NPs). Through annealing in darkness at temperatures between 200 °C and 300 °C an equilibrium between the two traps is established.

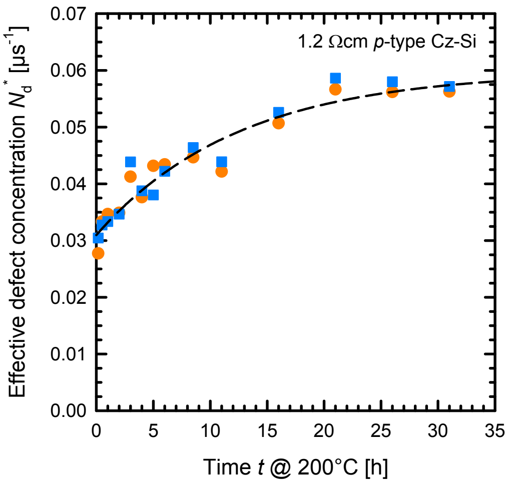

FIGURE 4.7: Change of the effective defect concentration N_t^* of two samples with a base resistivity of 1.2 Ω cm upon annealing at 200 °C in darkness. The black dashed line is a exponential fit with $y = y_0 + a(1 - exp(-\gamma \times t))$. After 20 hours a saturation of the defect concentration is observed.

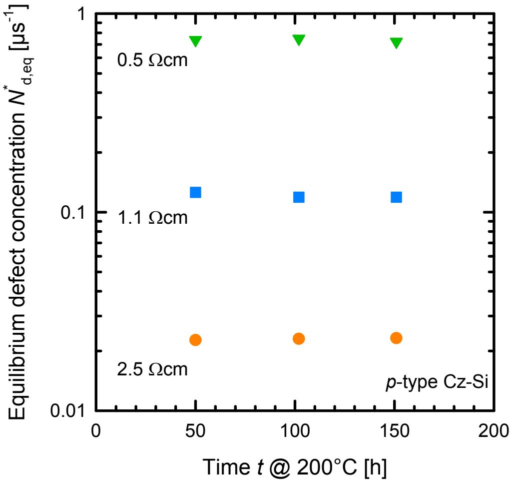

FIGURE 4.8: Equilibrium defect concentration $N_{d,eq}^*$ plotted versus the annealing time at 200 °C in darkness for three different samples with base resistivities between 0.5 Ω cm and 2.5 Ω cm. No change in $N_{d,eq}^*$ is observed for all three materials.

surfaces of the samples are passivated by the deposition of 10 nm Al_2O_3 via a plasma-ALD process. The sample processing is completed by an annealing step at 425 °C for 15 min in order to activate the surface passivation.

In Fig. 4.7, the change of the effective defect concentration N_d^* upon annealing in darkness at 200 °C of two samples with a base resistivity of 1.2 Ω cm is shown. The x-axis shows the cumulative annealing time t. After each annealing step the lifetimes τ_0 and τ_d - after illumination for 40 hours at room temperature with a light intensity of $P_{ill} = 10\,\mathrm{mW/cm^2}$ - are measured. As it is shown in Fig. 4.7, N_d^* increases in the first 20 hours until it starts to saturate. This increasing defect concentration can be reasonably well described by an exponential function: $y = y_0 + a(1 - \exp(-\gamma \times t))$. A fit of the data using this function is shown in Fig. 4.7 by the black dashed line with a resulting rate constant of $\gamma = 0.08 \pm 0.03\,\mathrm{h}^{-1}$.

Figure 4.8 shows the equilibrium defect concentration $N_{d,eq}^*$ plotted versus annealing time at 200 °C for three different samples featuring base resistivities of 0.5 Ω cm, 1.1 Ω cm and 2.5 Ω cm. In-between the lifetime measurements of τ_0 and τ_d after each annealing step, the samples are illuminated at room temperature longer than 100 hours using a halogen lamp with an illumination intensity of $P_{ill} \approx 10\,\mathrm{mW/cm^2}$. No change of the effective defect concentration $N_{d,eq}^*$ is observed for these samples for annealing times larger than 50 hours. This suggests that the equilibrium state is reached in ≤ 50 hours of annealing time for all samples, independent of the base resistivity. Accordingly, all samples are

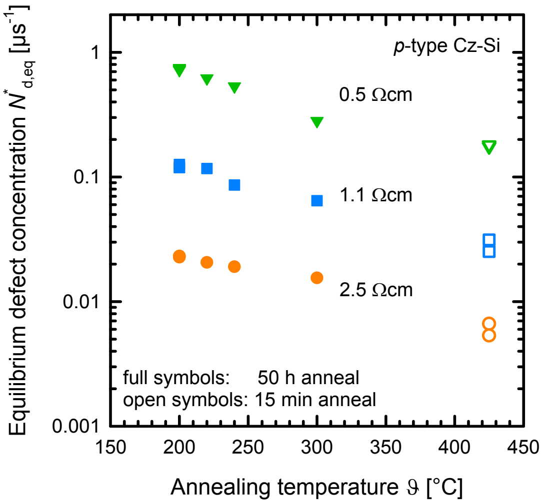

FIGURE 4.9: Equilibrium defect concentration $N^*_{d,eq}$ versus annealing temperature ϑ. $N^*_{d,eq}$ decreases with increasing temperature. Full symbols correspond to the defect concentration after annealing at the respective temperature for 50 hours, while open symbols correspond to the defect concentration after annealing for 15 min at 425 °C before and after the annealing sequence.

annealed for 50 hours in the following sequence: 240 °C, 220 °C, 200 °C and 300 °C. Please note that all samples of this investigation undergo this sequence. In Fig. 4.9, the equilibrium defect concentration is plotted versus the annealing temperature. The full symbols correspond to the equilibrium defect concentration after 50 hours annealing. The open symbols correspond to the defect concentration after annealing for 15 min at 425 °C before and after the annealing sequence. As can be seen from Fig. 4.9, the defect concentration $N^*_{d,eq}$ decreases with increasing temperature for all investigated materials.

Within the $\mathrm{B}_i\mathrm{B}_s\mathrm{O}_i$ model, the concentration $[\mathrm{B}_i\mathrm{B}_s\mathrm{O}_i]$ can be described according to the mass action law for a mobile B_i and a frozen-in $\mathrm{B}_s\mathrm{O}_i$ trap. Accordingly, the defect concentration $[\mathrm{B}_i\mathrm{B}_s\mathrm{O}]$ is proportional to the concentrations $[\mathrm{B}_i]$ and $[\mathrm{B}_s\mathrm{O}_i]$. Depending on the binding energy E_b between the two reactants, the relation

$$[B_iB_sO_i] \propto [B_i][B_sO_i] \times \exp\left(\frac{E_b}{k_bT}\right) \tag{4.1}$$

is obtained, with k_b being the Boltzmann constant and T the absolute temperature. On the other hand, the equilibrium concentration of the interstitial boron atoms $[\mathrm{B}_i]_{eq}$ follows the temperature dependence of the solubility in the silicon, comparable to the equilibrium between voids and free vacancies [75]. Hence, $[\mathrm{B}_i]_{eq}$ is given by

$$[B_i]_{eq} \propto \exp\left(-\frac{E_i}{k_bT}\right) \tag{4.2}$$

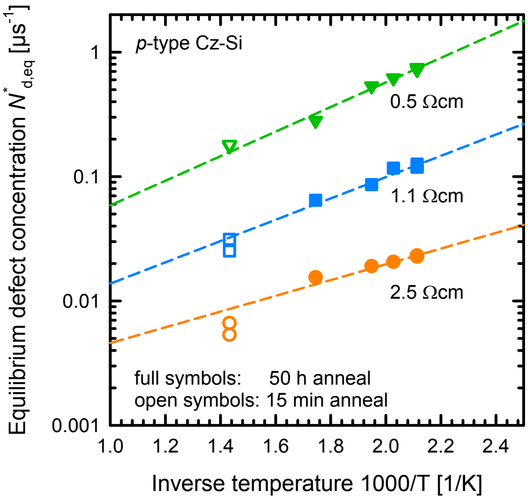

FIGURE 4.10: Equilibrium defect concentration $N^*_{d,eq}$ versus the inverse annealing temperature $1/T$. The coloured dashed lines are fits of Eqn. 4.3 to the data, which results in $\Delta E = (0.16 \pm 0.03)\,\mathrm{eV}$.

with the dissolution energy E_i between the boron nano-precipitates and the free interstitial boron atoms. Inserting Eqn. 4.2 into Eqn. 4.1 leads to:

$$[B_iB_sO_i] \propto \exp\left(\frac{E_b - E_i}{k_bT}\right) = \exp\left(\frac{\Delta E}{k_bT}\right) \tag{4.3}$$

ΔE describes the difference between the binding energies between the B_i and the traps $\mathrm{B}_s\mathrm{O}_i$, E_b, and between the B_i and the B-NPs, E_i.

Figure 4.10 shows an Arrhenius-like plot where the equilibrium defect concentration $N^*_{d,eq}$ is plotted versus the inverse temperature $1/T$. The coloured dashed lines are fits of the defect concentrations using Eqn. 4.3. From these fits $\Delta E = (0.16 \pm 0.03)\,\mathrm{eV}$ is obtained. As ΔE is positive, it can be concluded that the binding energy between the free B_i and the $\mathrm{B}_s\mathrm{O}_i$-traps is larger than the binding energy between the B_i and the B-NPs. Interestingly, the defect concentration extracted after annealing at 425 °C agrees well with the exponential fit. This suggests that an annealing at 425 °C for 15 min is sufficient to establish the equilibrium.

Moreover, the increasing equilibrium defect concentration $N^*_{d,eq}$ cannot be explained by the change of the solubility of one species alone. Two competing traps for this species need to be present, which are in the present model the $\mathrm{B}_s\mathrm{O}_i$ complex and the boron nano-precipitates. Hence, our experimental results clearly support the framework of the $\mathrm{B}_i\mathrm{B}_s\mathrm{O}_i$ model (see section 2.3.3.3).

4.3 Lifetime degradation in oxygen-rich n-type silicon

Apart from the boron-oxygen defect, the lifetime in oxygen-rich silicon can be limited solely due to the presence of oxygen independent of the doping type. Within this section, lifetime investigations are presented which are performed on Czochralski-grown n-type silicon doped with phosphorus. Various high-temperature treatments are performed which are known for their possible impact on the configuration of oxygen in the silicon and the resulting recombination activities (see section 2.2).

Apart from the point of fundamental interest, the influence of high-temperature treatments on the silicon material is also of major importance in the solar cell production of high-efficiency n-type solar cells which have the putative advantage that the boron-oxygen defect is irrelevant in the base material. However, the processing sequences of high-efficiency n-type silicon solar cells often feature high-temperature treatments, such as boron diffusions or thermal oxidations, which may cause a thermally induced degradation of the bulk lifetime [76]. Often, the lifetime reduction is not observed over the entire ingot, but only on some wafers, whereas other wafers cut from the same ingot show the desired high lifetimes. Within this section, these circumstances will be analysed in detail.

N-type silicon wafers cut from two different Czochralski-grown ingots, referred to as material A and B in the following, are investigated. The resistivities and the interstitial oxygen concentrations, measured in the centre of the wafers, are listed in Table 4.2. The resistivities are determined using four-point-probe measurements and the oxygen concentrations are determined via FTIR measurements according to IOC-88 standard [72]. The wafer thickness varies between 150 μm and 200 μm and the wafers are processed at full size, i.e. $156 \times 156\,\mathrm{mm}^2$.

The wafers from materials A and B are separated into three different groups. In the first group (group 1), the samples solely undergo the removal of the saw damage using KOH. In the second group (group 2), after the same treatment as the first group, the samples undergo a boron diffusion (in BBr_3) at a peak temperature of 930 °C for 80 min resulting in a p^+-region with $40\,\Omega/\square$ sheet resistance. Afterwards, the borosilicate glass (BSG) as well as the p^+-region are removed using HF and KOH, respectively. In the

TABLE 4.2: Resistivities ρ and interstitial oxygen concentrations $[O_i]$ of the investigated materials. The values are determined by 4-point probe measurements and the FTIR method in the centre of the wafer, respectively.

Material	**A**	**B**
Resistivity ρ $[\Omega\,\mathrm{cm}]$	1.7 ± 0.1	3.7 ± 0.2
Oxygen concentration $[O_i]$ $[10^{17}\,\mathrm{cm}^{-3}]$	10 ± 1	8 ± 1

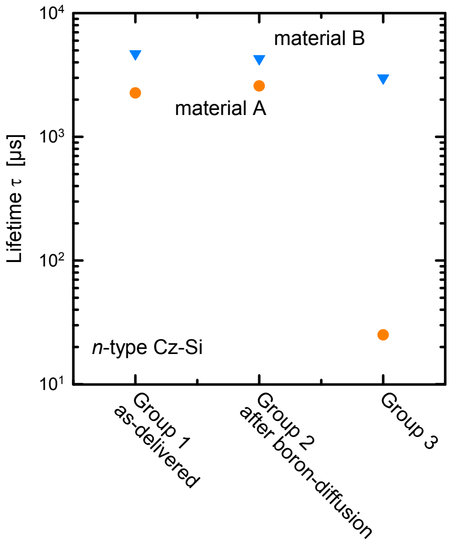

FIGURE 4.11: Lifetime τ measured at $\Delta p = 10^{15}\,\text{cm}^{-3}$ for each investigated group. For Group 3 an example for an oxidation at 1000 °C is shown. Material B exhibits high lifetimes in every group. Material A degrades severely after thermal oxidation (Group 3). The measurements are performed in the centre of the samples.

third group (group 3), the samples undergo the same boron diffusion as group 2. The BSG is removed before a dry oxidation for 130 min is performed. Different oxidation temperatures between 900 °C and 1050 °C are examined using wafers of both ingots. After the oxidation process, the oxide layer as well as the p^+-region are removed using again HF and KOH. All samples are then surface-passivated on both sides using silicon nitride (SiN), deposited via plasma-enhanced chemical vapour deposition (PECVD) in a Roth & Rau SINA tool. The SiN passivation layer is chosen to be 70 nm thick with a refractive index of $n_r = 2.4$.

Photoconductance decay (PCD) as well as quasi-steady-state photoconductance (QSSPC) lifetime measurements are performed using the lifetime tester WCT-120 from Sinton Instruments. For spatially resolved lifetime measurements the method of photoconductance-calibrated photoluminescence imaging (PC-PLI) is used (see chapter 2).

Results of the lifetime investigation are shown in Fig. 4.11. Only a moderate lifetime degradation after high-temperature processing is observed for material B (compare group 1-3). In contrast, material A exhibits high lifetimes (above 2 ms) in group 1 and 2. However, after the second high-temperature process in group 3, the lifetime degrades severely to 25 μs. A PC-PLI measurement of this sample reveals an inhomogeneous lifetime distribution over the sample (see Fig. 4.12). While in the centre of the wafer the lifetime degrades strongly after the oxidation process, at the corner of the wafer the lifetime is on a much higher level. Figure 4.13 shows a line scan over the PC-PL image of the corresponding sample from the centre of the wafer to one of its corners. The

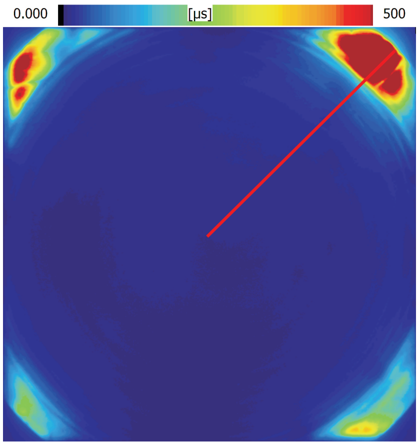

Figure 4.12: PC-PL-image of a lifetime sample of material A after boron diffusion and oxidation, determined at a light intensity of 0.12 suns. The centre of the sample shows a strongly reduced lifetime while the edges of the sample feature a much higher lifetime. The red solid line marks the area of the line scan shown in Fig. 4.13.

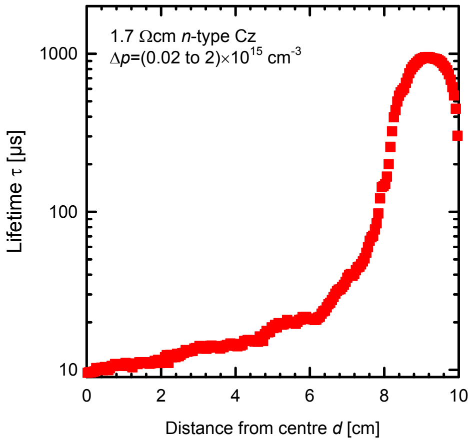

Figure 4.13: Line-scan of the PC-PL-image shown in Fig. 4.12 from the centre of the wafer to its corner. The lifetime varies over almost two orders of magnitude.

PC-PLI measurement reveals a ring structure, frequently observed in Cz-grown silicon due to the symmetries of the growth conditions.

As lifetime degradation after high-temperature processing is known to occur on material A, the impact of the peak oxidation temperature is examined. For this purpose wafers from materials A and B are processed according to group 3 with oxidation temperatures of 900 °C, 950 °C, 1000 °C and 1050 °C. The results of this investigation are shown in Fig. 4.14. For material A, a strong degradation of the lifetime to values below 100 μs can be observed for oxidation temperatures from 900 °C to 1000 °C. The lowest lifetime is observed after oxidation at 1000 °C suggesting that at this temperature defect generation is most efficient. At 1050 °C peak temperature the degradation of the lifetime is less severe than for the lower temperatures but still about an order of magnitude lower than the value measured on the same material after a boron diffusion.

The defects responsible for lifetime degradation after high-temperature treatment have been attributed in the past to the agglomeration of intrinsic point defects and interstitial oxygen, the major contamination in Cz-grown silicon, during the crystal growth process [77]. The problem for solar cell production is, as observed in this study, that these defects are not detectable in the as-grown material and reveal their harmful presence only after high-temperature processes. However, in semiconductor industries, oxygen precipitation has been widely studied due to both its beneficial (transition metal gettering, strengthening of the material) as well as its harmful properties (if present in the active region

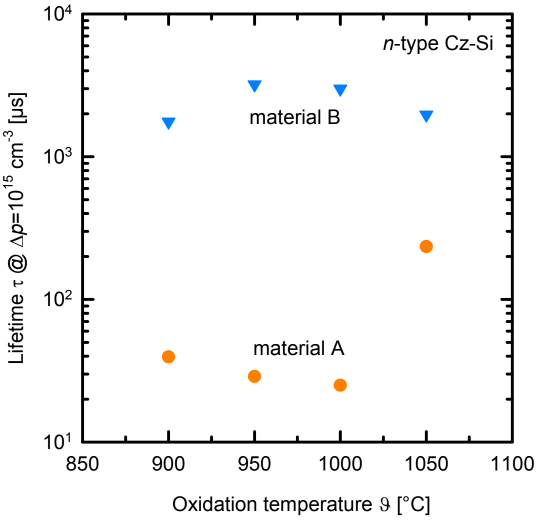

FIGURE 4.14: Lifetime τ, determined at $\Delta p = 10^{15}\text{cm}^{-3}$, plotted versus oxidation temperature ϑ. A variation of the lifetime depending on the oxidation temperature is observed for material A. The lifetime of material B hardly depends on the oxidation temperature.

of an integrated circuit (IC) precipitates act as defects and impair device performance). From these studies it is known that a grown-in distribution of oxygen precipitate nuclei can be dissolved by a single high-temperature treatment of the wafer before it is subsequently processed to the desired device. This high-temperature treatment is often referred to as “tabula rasa” treatment [15, 16] (see section 2.2).

In semiconductor industries, the tabula rasa treatment has been applied to obtain a starting material with an almost ideal oxygen cluster distribution consisting of only

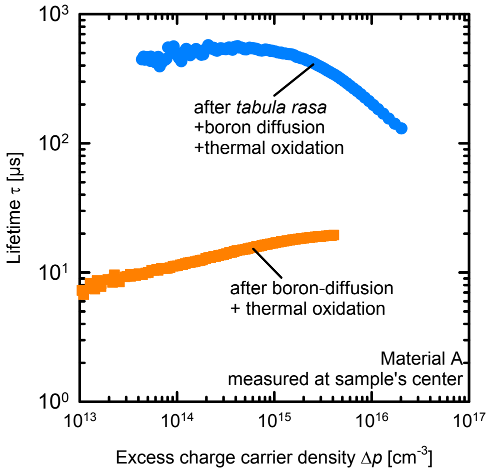

FIGURE 4.15: Injection-dependent lifetime $\tau(\Delta n)$ of two samples after boron diffusion and thermal oxidation at 1000 °C. The blue curve represents a sample with the tabula rasa treatment performed before sample processing. The sample corresponding to the orange curve is processed without tabula rasa treatment.

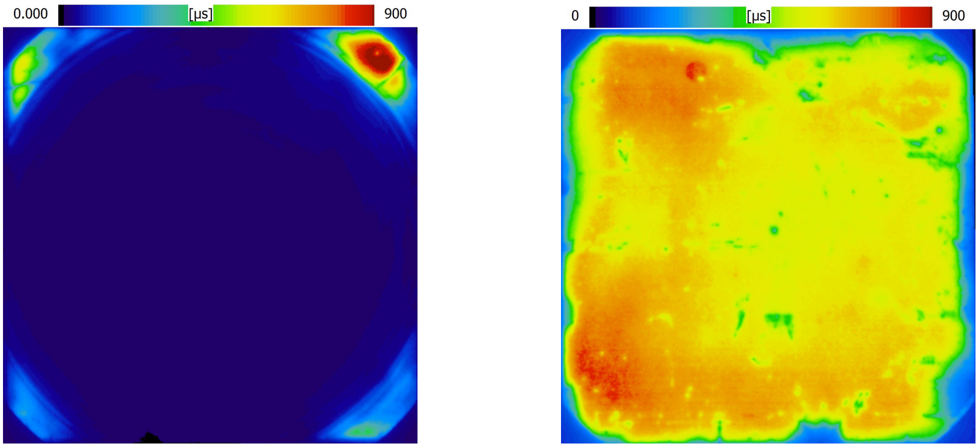

FIGURE 4.16: PCPL-image of two samples from material A at an illumination intensity of 0.12 suns. The samples are processed according to group 3 including a boron diffusion and an oxidation. On the left, no tabula rasa treatment is applied before sample processing, on the right tabula rasa is applied.

monomeric, interstitial oxygen. From this starting material, a desired cluster distribution can be tailored by applying various high-temperature treatments. Here, the tabula rasa treatment is adapted to silicon solar cell material. For this purpose, another group of lifetime samples consisting of material A is processed, including boron diffusion and thermal oxidation (group 3). This time, however, before performing the boron diffusion, the tabula rasa treatment is applied, which dissolves the major part of the grown-in distribution of oxygen precipitate nuclei. The tabula rasa treatment is performed in a conventional belt-firing furnace (Centrotherm, DO-FF-8.600-300) with a belt speed of 2.0 m/min and a peak temperature of 1000 °C (set temperature). After this step, the lifetime samples are processed including a boron diffusion and a thermal oxidation at 1000 °C. The result of this investigation is shown in Fig. 4.15, proving that this additional high-temperature treatment before sample processing is very beneficial for this material. From 17 μs (at $\Delta p = 10^{15}\,\text{cm}^{-3}$), without tabula rasa treatment, the lifetime increases by a factor of 20 to 500 μs (at $\Delta p = 10^{15}\,\text{cm}^{-3}$). The injection-dependent lifetime curve without tabula rasa treatment features a decreasing lifetime towards low injection densities, which has to be attributed to a bulk defect. Compared to that, applying the tabula treatment, the injection-dependent lifetime shows no or only a very weak decrease towards low injection densities.

Apart from the increase of the measured effective lifetime in the centre of the sample, the lifetime distribution also changes after the tabula rasa treatment. In Fig. 4.16, two lifetime images of samples of material A are compared. No tabula rasa treatment is applied to the sample corresponding to the map on the left, whereas on the right a map of a sample with tabula rasa treatment is shown. In the case where tabula rasa is applied before sample processing, a homogeneous lifetime distribution over the entire wafer is observed.

To identify the defects being responsible for the lifetime degradation of material A, a defect analysis according to Shockley-Read-Hall theory is performed [61, 62]. The analysis of the injection-dependent lifetime reveals that the lifetime curve can be fitted by two defect centres, if the recombination at the surfaces is neglected. The defect characteristics of the two centres, suitable to describe the injection-dependent lifetime curves, are summarized in Table 4.3, with E_c being the energy level of the lower edge of the conduction band, E_v the energy level of the upper edge of the valence band and E_t the energy level of the recombination centre. σ_n and σ_p correspond to the capture cross sections for electrons and holes, respectively. For material B, where no degradation is observed, only a shallow defect centre is present (defect II in Table 4.3). However, for material A, where degradation after thermal oxidation occurs (cf. group 3), an additional defect centre with an energy level close to the middle of the band gap (defect I) is needed to model the injection-dependent lifetime curve. Within this investigation, using these two sets of defect parameters all injection-dependent lifetime curves are successfully modelled. The values of these defect parameters suggest that different defect centres are present compared to the recently published ones found by Murphy et al. [63]. An analysis of the injection-dependent lifetime of the sample treated with the tabula rasa treatment shows that the shape of the lifetime curve can also be explained by the two defects present in the material without the tabula rasa treatment. This may be an indication that the dissolution of the grown-in distribution of precipitate nuclei is not completed after the short high-temperature treatment in the belt furnace. However, this result supports the interpretation of oxygen precipitates being responsible for the observed lifetime degradation after high-temperature processing. In Figure 4.17 an example of the injection-dependent lifetime after boron diffusion (green triangles),

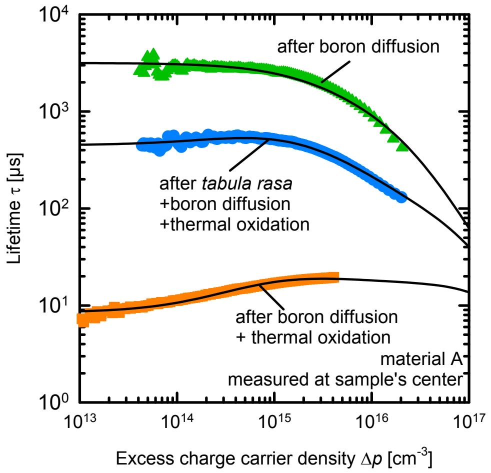

FIGURE 4.17: Injection-dependent lifetime $\tau(\Delta n)$ of three samples after boron diffusion (green triangles), after B-diffusion and oxidation at 1000 °C (orange squares) and after tabula rasa and both high temperature process steps (blue circles). The black solid lines are calculated using the defect parameters shown in Table 4.3.

Table 4.3: Defect parameters suitable to describe the measured injection-dependent lifetime curves on materials A and B.

Defect	**I**	**II**
$E_c - E_t$ or $E_t - E_v$ [eV]	> 0.3	< 0.2
σ_n/σ_p	0.12 ± 0.04	> 0.1

after boron diffusion and subsequent oxidation (orange squares) as well as after tabula rasa and the two high-temperature process steps (blue circles) is shown. The calculated injection-dependent lifetimes (black solid lines) using the parameters summarized in Table 4.3 fit well to the measurements.

4.4 Chapter summary

The impact of the crystal growth conditions on the formation of the BO defect has been studied on three differently grown crystals at three different positions: seed end, centre and tail end. It was shown for the first time in a comprehensive investigation that the variation of the effective defect concentration along the crystal axis can be fully attributed to the variation of the hole and the oxygen concentrations. In addition, a fast cooling after crystallization reduces the normalized defect concentration by almost 30 %, although this effect is only observed in defective crystals.

In the second part of this study, the lateral distribution of the boron-oxygen-related defect centre on wafers cut from different crystal position was examined. In accordance with the previous result, the variations in the effective defect concentration were attributed to the varying concentrations of holes and oxygen alone. In particular, we have shown for the first time that typical growth-related concentrations of the intrinsic point defects, such as vacancies and self-interstitials, have no impact on the boron-oxygen-related defect concentration. From these results it can be concluded that the formation of the boron-oxygen-related defect is not systematically affected by the pulling conditions of the Czochralski growth process.

In the second part of the chapter, the equilibrium BO defect concentration after prolonged annealing at temperatures between 200 °C and 300 °C was examined. We discovered that after processing, the defect concentration has not necessarily reached an equilibrium. For the investigated materials with base resistivities ranging between 0.5 Ω cm and 2.5 Ω cm it was observed that an annealing at 200 °C for 50 hours establishes the equilibrium, independent of the base resistivity. Investigations at different temperatures revealed that the equilibrium defect concentration decreases with increasing annealing temperature. This observation is in accordance with the predictions of the most recent

$B_iB_sO_i$ model. Within the $B_iB_sO_i$ model, the equilibrium defect concentration corresponds to an equilibrium between free interstitial boron atoms captured by the B_sO_i trap and the boron nano-precipitate. The observed decreasing defect concentration with increasing temperature translates within the model into a higher binding energy between B_i and the B_sO_i complex compared to the dissociation energy between B_i and the boron-nano-precipitates.

In the last part of this chapter, lifetime limitations of oxygen-rich silicon have been studied in phosphorus-doped *n*-type Cz-grown silicon. While one material under investigation featured a high lifetime independent of the additional temperature treatments, the lifetime of another material was significantly reduced after a high-temperature step. Based on a thermal oxidation process, we discovered that the reduction of the lifetime is most pronounced at 1000 °C, hence the defect generation is most efficient at this temperature. However, an additional short high-temperature step (‘tabula rasa’), which was within this thesis realized for the first time in an industrial belt-line furnace prior to the thermal oxidation, strongly reduced the lifetime degradation during the subsequent thermal process. Our results are in accordance with the behaviour of oxygen in silicon and were explained with the temperature- and time-dependent growth/dissolution of oxygen precipitates and their recombination activity.

Chapter 5

Permanent deactivation of the boron-oxygen-related recombination centre

The following chapter is divided into three parts. In the first part, the deactivation kinetics and parameters controlling the kinetics, such as the sample cooling, the deactivation temperature and the illumination intensity during the deactivation process are analysed in detail. In the second part, we examine if hydrogen —incorporated into the sample during processing— is affecting the deactivation kinetics. In the third part, a new parameterization of the lifetime which can be reached after fully deactivating the BO defect is introduced, as a function of the doping concentration and the injection density. Additionally, the impact of the parameterized lifetimes on next-generation industrial-type solar cells is examined by means of numerical simulations.

5.1 Deactivation kinetics

The boron-oxygen-related recombination centre poses a fundamental limitation on the efficiency of solar cells fabricated from oxygen-rich boron-doped silicon. It has been known for a while that the sample cooling after a high temperature process has a crucial impact on the BO defect concentration [22] although no detailed study on this effect was performed up to now. In this section, the cooling rate after high-temperature annealing is systematically varied and its impact on the lifetime of boron-doped Cz-Si samples is examined in three well-defined states: (i) after complete light-induced degradation, τ_d, (ii) after subsequent recovery in darkness at 200 °C, τ_0, and (iii) after permanent recovery, i.e. after permanent deactivation of the BO centre [4], τ_{0p}.

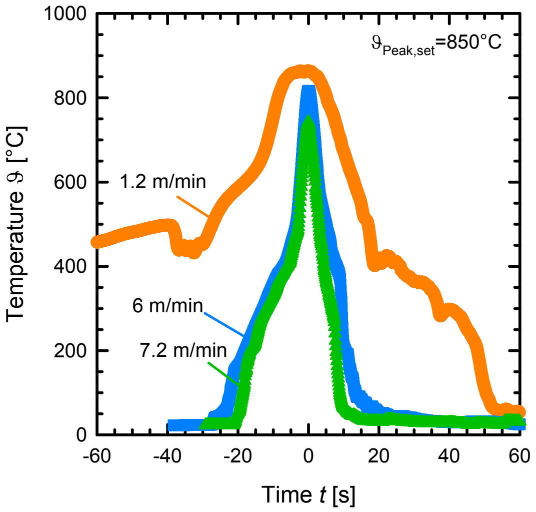

FIGURE 5.1: Temperature profiles determined using a temperature probe attached to a lifetime sample. The probe sample is passivated with an Al_2O_3/SiN_x stack. Different coloured symbols correspond to different belt speeds ranging between 1.2 and 7.2 m/min. The set peak temperature is fixed at $\vartheta = 850\,°C$.

5.1.1 Experimental details

Sample processing includes the removal of surface damage, a phosphorus diffusion (850 °C, 70 min) followed by the removal of the n^+-region, and the passivation of the surfaces. For the surface passivation Al_2O_3 is chosen (film thickness 10 nm) which is deposited via plasma-assisted atomic layer deposition (plasma-ALD). A 70 nm- hick silicon nitride (SiN_x) capping layer is deposited via plasma-enhanced chemical vapour deposition (PECVD) in order to improve the thermal stability of the passivation [78]. The surface passivation of the deposited layers is then activated by annealing at 425 °C for 15 min in ambient atmosphere [79]. On a second set of samples, the n^+-region remains on the samples during the rapid thermal annealing (RTA) process. The n^+-region is removed after the RTA and the surfaces are passivated with a single Al_2O_3 layer followed by the activation anneal as mentioned above.

The RTA process is carried out in a commercially available belt-line firing furnace (DO-FF-8.600-300, Centrotherm). In order to realize various cooling rates, different temperature profiles are chosen, corresponding to different belt speeds and peak temperatures. The set peak temperature is either 650 °C or 850 °C and the belt speed is varied from 1.2 up to 7.2 m/min. The temperature profile is monitored by a temperature probe attached to a wafer which is processed identically to the lifetime samples. The profile is recorded using a DATAPAQ Insight Oven Tracker. An example of the recorded temperature profiles is shown in Fig. 5.1 for a sample passivated with an Al_2O_3/SiN_x stack. As can be seen from Fig. 5.1, the belt speed has a pronounced impact on the maximum temperature as well as the heating and cooling behaviour.

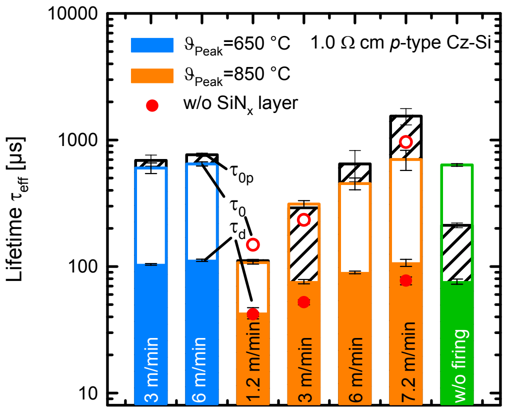

FIGURE 5.2: Measured lifetimes after light soaking τ_d (full columns), after annealing in the dark (200 °C for 10 min) τ_0 (open columns with colour edge), and after permanent recovery τ_{0p} (hatched columns). Orange columns correspond to a set peak temperature of 850 °C and blue columns to a peak temperature of 650 °C. Red circles corresponds to the lifetimes τ_d (full symbols) and τ_0 (open symbols) of samples without SiN_x layer during RTA treatment. The belt speeds are displayed in each bar. The green column on the right corresponds to samples without additional RTA treatment before the lifetime measurement.

Lifetimes are measured using a WCT-120 lifetime tester (see section 3.2.1). If not mentioned, all lifetimes are reported at an injection density of $\Delta n = 0.1 \times p_0$ with Δn being the excess electron concentration and p_0 the dark value of the hole concentration (identical, in our case, to the boron concentration). The characteristic lifetimes are denoted as:

(i) τ_d - fully degraded lifetime after light soaking under a halogen lamp at a light intensity of $P_{ill} \approx 10\,\mathrm{mW/cm^2}$ for 12 h or longer,

(ii) τ_0 - after annealing in the dark at 200 °C for 10 min (this lifetime is used as the reference value for calculating the effective concentration of the recombination centres), and

(iii) τ_{0p} - after annealing the degraded samples at elevated temperatures (typically around 185 °C) under illumination with a halogen lamp intensity of $100\,\mathrm{mW/cm^2}$ [this is the stable (permanently recovered) value that does not change (or changes only slightly) upon subsequent illumination at room temperature (see chapter 6)].

5.1.2 Impact of rapid thermal annealing (RTA)

The material used for this investigation is 150 μm thick boron-doped Cz-Si with a resistivity of $\rho = (1.02 \pm 0.03)\,\Omega\,\mathrm{cm}$ and an interstitial oxygen concentration of $[\mathrm{O}_i]=$

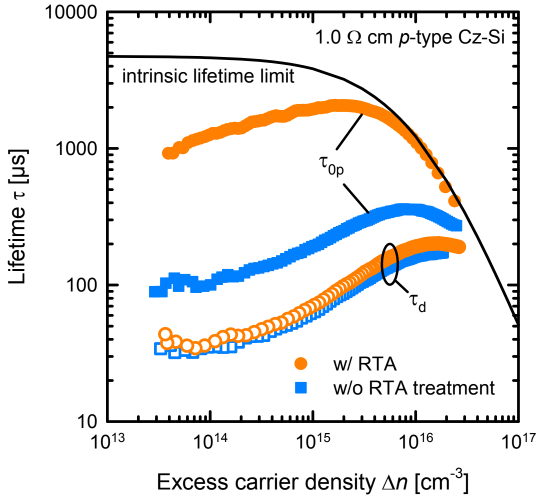

FIGURE 5.3: Measured injection-dependent lifetimes $\tau(\Delta n)$ in two different stable states: (i) after complete degradation τ_d and (ii) after permanent recovery τ_{0p}. Open symbols correspond to the lifetimes after complete degradation and full symbols after permanent recovery. The lifetime values of the sample without RTA treatement are shown as blue squares, whereas the lifetimes of the sample with the RTA treatment at 7.2 m/min belt speed and 850 °C peak temperature are shown as orange circles. For comparison, the intrinsic lifetime limit [81] is also included (black line).

$(6.9 \pm 0.3) \times 10^{17}\,\mathrm{cm}^{-3}$, determined via four-point-probe and FTIR measurements (IOC 88), respectively. We observe (see Fig. 5.2) that for all samples the three characteristic lifetimes, τ_0, τ_d and τ_{0p}, depend on the conditions of the RTA process. For an applied peak temperatures of 850 °C, all three lifetimes increase strongly with increasing belt speed. For a peak temperature of 650 °C this increase is only observed for τ_d. τ_0 and τ_{0p} appear to be independent of the belt speed, considering the uncertainties. At 850 °C peak temperature and 1.2 m/min belt speed the lowest lifetimes are measured: $\tau_d = (42 \pm 4)\,\mu\mathrm{s}$, $\tau_0 = (107 \pm 3)\,\mu\mathrm{s}$ and $\tau_{0p} = (111 \pm 3)\,\mu\mathrm{s}$. The lifetime after complete degradation is the highest after the 650 °C RTA treatment with 6 m/min belt speed: $\tau_d = (112 \pm 2)\,\mu\mathrm{s}$. The lifetimes after dark recovery and after permanent recovery are the highest after the 850 °C RTA treatment at the maximum belt speed of 7.2 m/min: $\tau_0 = (700 \pm 125)\,\mu\mathrm{s}$ and $\tau_{0p} = (1540 \pm 225)\,\mu\mathrm{s}$. For comparison, on samples without RTA treatment we measure $\tau_d = (76 \pm 4)\,\mu\mathrm{s}$, $\tau_0 = (635 \pm 20)\,\mu\mathrm{s}$, and $\tau_{0p} = (212 \pm 9)\,\mu\mathrm{s}$; the permanently recovered value is essentially lower than for the RTA-processed samples. Please note that the lifetimes τ_0 and τ_d of the samples without additional hydrogen-rich layers also increase with increasing belt speed (red circles in Fig. 5.2). This indicates that the observed increase of the lifetimes is not due to a hydrogen-related effect, as it was recently suggested by Hallam et al. [80]. In the following, results of lifetime samples with hydrogen-rich layers present during firing (i.e., $\mathrm{Al_2O_3/SiN}_x$ stacks) are discussed only.

Figure 5.3 shows the injection level dependence of τ_d (after complete degradation) and

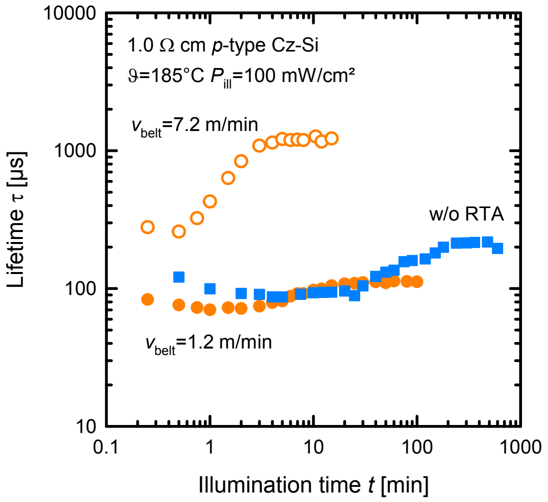

FIGURE 5.4: Measured lifetime τ ($\Delta n = 0.1 \times p_0$) versus illumination time t during the process of permanent recovery. Circles correspond to a sample processed including an RTA treatment with a peak temperature of 850 °C: open symbols at 7.2 m/min belt speed, full symbols at 1.2 m/min belt speed. Blue squares correspond to a sample without RTA treatment but with an annealing step at 425 °C for 15 min.

τ_{0p} (after permanent recovery) for a reference sample without RTA and a sample after the most efficient RTA treatment (7.2 m/min belt speed, 850 °C peak temperature). While the lifetime curves of τ_d almost coincide, the lifetime τ_{0p} is significantly higher for the RTA-processed sample.

The typical lifetime evolution during the process of permanent recovery is shown in Fig. 5.4. The measured lifetimes are transformed into an effective defect concentration N_t^* using Eqn. 2.1. The recovery rate constant R_{de} is then determined by fitting an exponential decay function $A\exp(-R_{de} \times t) + B$ to N_t^*. The lowest rate constant, $R_{de} = (1.0 \pm 0.2)\,\mathrm{h}^{-1}$, is obtained for the sample that has not received any RTA treatment (blue symbols in Fig. 5.4). By applying a peak temperature of 850 °C and a belt speed of 7.2 m/min, R_{de} is increased by almost two orders of magnitude, up to $R_{de} = (75 \pm 11)\,\mathrm{h}^{-1}$. Thus, we achieve an acceleration of the permanent recovery process by two orders of magnitude after the RTA treatment and an increase of the absolute lifetime after permanent recovery of one order of magnitude.

Within the framework of the $B_iB_sO_i$ model [82] (see section 2.3.3.3), the reduction of the effective lifetime upon light soaking has been attributed to a change in the configuration of a grown-in complex consisting of an interstitial boron atom (B_i) and a frozen-in complex B_sO_i. During cooling, the free interstitial boron atoms (produced by self-interstitials emitted by oxide particles) agglomerate into small precipitates (nano-precipitates, NPs). This happens at a relatively high temperature, which we show later in this work to be around 600 °C. At this stage, the remaining free interstitial boron atoms are in equilibrium with the NPs, and there are also complexes of B_i with other

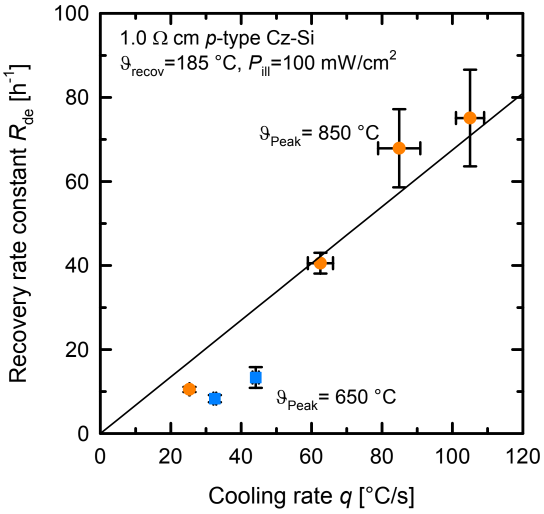

FIGURE 5.5: Measured recovery rate constant R_{de} as a function of the cooling rate q in a temperature range between 575 °C and 625 °C. Samples with RTA treatment at 850 °C peak temperature are shown as orange circles, samples with RTA treatment at 650 °C are shown as blue squares. The black line is a guide to the eye.

impurities, such as B_s, O_i, O_{2i}, etc. The defect responsible for the light-induced degradation has been proposed recently by Voronkov and Falster to be B_iB_sO [82]. Below some relatively low characteristic temperature ϑ_f, (roughly, less than 350 °C [82]) the equilibrium between the B_i-containing defects and the NPs is no longer supported, and the total concentration of the defects is frozen-in. This means that the concentration of frozen-in $B_iB_sO_i$ defects depends on the cooling rate $q = -d\vartheta/dt$ at ϑ_f, and also on the NP density and size - which in turn depend on q but now referring to a different characteristic temperature ϑ_n. Accordingly, the dependence of the frozen-in $B_iB_sO_i$ concentration (and hence of the degraded lifetime τ_d) on the cooling conditions is somewhat complicated being dependent on the full cooling curve rather than on the cooling rate in a single temperature interval. A noticeable impact of sample cooling after a high-temperature step on the effective defect concentration N_t^* was reported previously by Bothe et al. [22].

Within the $B_iB_sO_i$ model, the permanent recovery can be attributed to increasing the free B_i atom concentration by a partial dissociation of B_i-containing complexes at the recovery temperature and in the presence of excess carriers. An enhanced loss of B_i to the NPs [34, 83] leads to the disappearance of all B_i-containing centres —-including $B_iB_sO_i$— and subsequent illumination at room temperature does not lead to a renewed lifetime degradation. Please note, that the same explanation of the permanent recovery is also used within the B_iO_{2i} model [34] as both models assume the presence of boron nano-precipitates. The rate constant of the permanent recovery R_{de} is then proportional to the sinking ability of NPs which is characterized by the product of the NP density

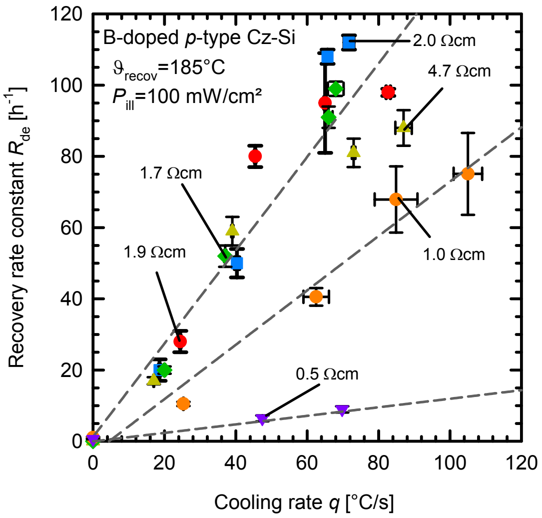

FIGURE 5.6: Recovery rate constant R_{de} versus cooling rate q in a temperature range between 575 °C and 625 °C after RTA for various silicon materials relevant for solar cell production. The base resistivity varies between 0.5 and 4.7 Ω cm. For all materials, R_{de} increases with increasing cooling rate q. The grey dashed lines are guides to the eyes.

N_p and the average NP radius R_p as discussed in detail in Ref. [83]. These properties of the NPs can be analysed using an analogy with vacancy aggregation into voids [11] (see section 2.3.3.3). Upon lowering ϑ, e.g. after an RTA step, the nucleation rate of NPs is rapidly increasing, and, at some temperature, becomes so high that the number of growing NPs completely consumes the dissolved B_i, thus suppressing further nucleation. Appreciable nucleation occurs in a very narrow temperature interval, and the produced NP density N_p and the final average NP radius R_p (upon consuming the majority of dissolved B_i) depend in a simple way on the cooling rate q and on the concentration of B_i atoms prior to the nucleation/growth stage. Remarkably, the quantity of interest, the $N_p \times R_p$ product, is independent of $[B_i]$ and simply proportional to q (see Eqn. 2.9). Hence, the rate constant for the permanent recovery (deactivation) should follow this simple dependence on the cooling rate:

$$R_{de} \propto N_p \times R_p \propto q. \tag{5.1}$$

The cooling rate q in this expression refers to a narrow temperature interval where the NP nucleation occurs, and thus to some definite temperature ϑ_n of nucleation – which is unknown beforehand but can be estimated from our experimental data. To do so, we determine the cooling rate q of every investigated temperature profile in specific temperature intervals using linear approximations. As can be seen in Fig. 5.5, we observe a linear correlation of R_{de} and $q = -d\vartheta/dt$ for the temperature range between 575 and 625 °C. From these data we conclude that the nucleation temperature of NPs is around 600 °C.

Our highest achieved recovery rate constant of $R_{de} = (75 \pm 11)\,\mathrm{h}^{-1}$ corresponds to a cooling rate of $q \sim 100\,^\circ\mathrm{C/s}$ in the indicated temperature range. According to Eqn. 5.1 we would expect that further increasing the cooling rate (although difficult to realize experimentally) would lead to still higher values of R_{de}. The proportionality coefficient between R_{de} and q (with the units used above) is according to our measurements about $2.08 \times 10^{-4}\,^\circ\mathrm{C}^{-1}$.

The majority of B_i-containing complexes is believed to disappear in the course of permanent recovery and the achieved lifetime τ_{0p} is then controlled by other defects. In principle, also the NPs may contribute to the recombination but this contribution is apparently very small – since we measure the highest value of τ_{0p} for the highest cooling rate, when the NP density is the highest.

To further support the validity of our findings shown in Fig. 5.5, the experiment is repeated with lifetime samples, processed analogously to the samples shown in Fig. 5.5, on five different Cz-Si materials with base resistivities ranging from 0.5 to 4.7 Ω cm. Again, a variation of the belt speed during the firing process at a constant set peak temperature of 850 °C facilitates different cooling rates q at $\sim 600\,^\circ\mathrm{C}$. Each individual cooling rate is measured with a temperature probe attached to a sample processed in parallel to the sample under investigation. Figure 5.6 shows the recovery rate constants R_{de} versus various measured cooling rates q at 600 °C after RTA. For comparison the rate constants shown in Fig. 5.5 are also displayed. We observe an increasing rate constant R_{de} with an increasing cooling rate q for all investigated materials, which emphasizes the general validity of our findings shown in Fig. 5.5. Interestingly, the recovery rate constants determined on 1.0 Ω cm material are lower than the rate constants measured

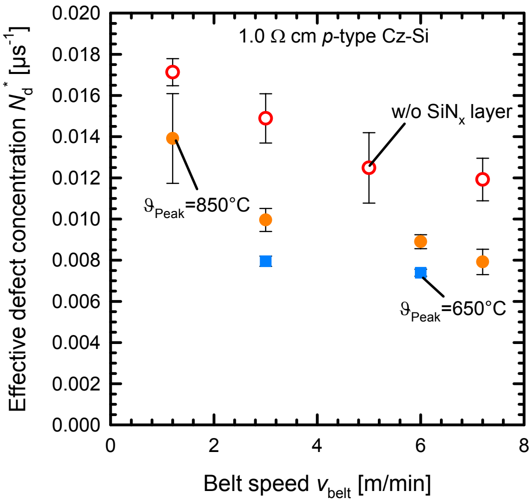

FIGURE 5.7: Effective defect concentration N_d^* plotted versus the belt speed v_{belt} during RTA treatment. A fast belt speed leads to a fast cooling of the sample. Samples treated with a peak temperature of 850 °C are shown as circles, samples treated with 650 °C are shown as squares. N_d^* decreases with increasing belt speed.

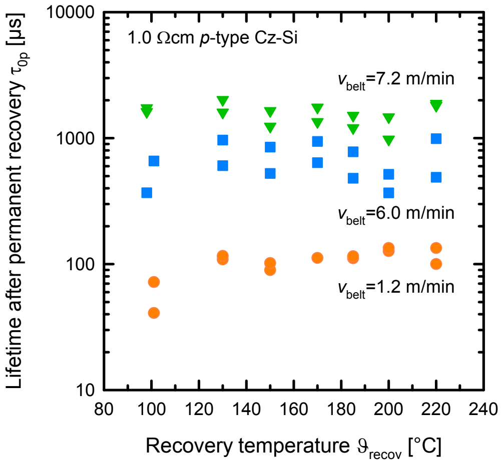

FIGURE 5.8: Lifetime after permanent recovery τ_{0p} depending on the recovery temperature ϑ_{recov} for samples exposed to a peak temperature of 850 °C during RTA. During RTA the samples are passivated with an Al_2O_3/SiN_x stack. Green triangles correspond to samples processed with a belt speed of 7.2 m/min, blue squares correspond to a belt speed of 6.0 m/min and orange circles correspond to the lowest belt speed of 1.2 m/min.

for the materials of higher resistivities, but no unambiguous dependence on the doping concentration p_0 can be extracted from these results. The grey dashed lines are guides to the eyes of the expected linear behaviour. The different slopes of the dashed lines might indicate that apart from the cooling rate at ~ 600 °C another parameter exists which additionally influences the recovery rate constant, however, to a much weaker extent than the cooling rate. One may speculate that a dependence on the resistivity up to resistivities in the range of 1.7 Ω cm exists, especially when considering the results on 0.5 Ω cm material, which show for the highest cooling rate a much smaller recovery rate constant. Therefore, further investigations are needed to clarify this possible correlation with the doping concentration.

The effective defect concentration after complete degradation, $N_d^* = 1/\tau_d - 1/\tau_0$, is proportional to the frozen-in concentration of $B_iB_sO_i$ and, hence, should depend on the cooling conditions in a more complicated way –as discussed above– being sensitive to the entire cooling curve. In Fig. 5.7, N_d^* is plotted as a function of the belt speed. A fast belt speed generally leads to a fast cooling of the sample. There is a well pronounced reduction in N_d^* upon increasing the sample cooling, although the effect is not as strong as for the permanent recovery rate constant R_{de} at the defined temperature interval.

5.1.3 Impact of the recovery temperature

The material used in this experiment is again the 150 μm thick boron-doped Cz-Si material with a resistivity of $\rho = 1.0\,\Omega\,\text{cm}$. All samples are coated with an Al_2O_3/SiN_x stack passivation on both wafer surfaces. The impact of the recovery temperature on the

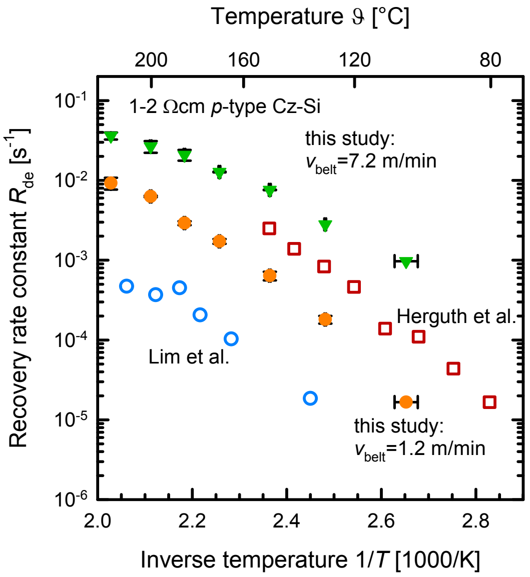

FIGURE 5.9: Arrhenius-plot of the recovery rate constant R_{de}. Full symbols correspond to data taken from this study treated with a set peak temperature of 850 °C during RTA. Open squares correspond to data taken from a publication by Herguth et al. [84] and open circles to data taken from Lim et al. [36].

lifetime after permanent recovery is examined by performing the recovery treatment at different temperatures ranging between 100 and 220 °C, however, at a constant illumination intensity of $P_{ill} = 100\,\mathrm{mW/cm^2}$. In Fig. 5.8, the result of this experiment is shown for samples exposed to an RTA step at 850 °C peak temperature and belt speeds of 7.2, 6.0 and 1.2 m/min (corresponding to green triangles, blue squares and orange circles, respectively). As can be seen from Fig. 5.8, for all three RTA conditions the lifetimes show a significant scatter, however, the different conditions can be clearly separated in the plot. Despite the scattering, it can be concluded that the lifetime after permanent recovery is independent of the recovery temperature (for a defined RTA treatment). Within this study, the highest achieved lifetime after permanent recovery of $\tau_{0p} = 2020\,\mu\mathrm{s}$ is measured on a sample treated during RTA with 850 °C peak temperature and a belt speed of 7.2 m/min and permanently recovered at a recovery temperature of 130 °C at a light intensity of $100\,\mathrm{mW/cm^2}$.

In contrast to the lifetime after permanent recovery τ_{0p}, the rate constant R_{de} critically depends on the recovery temperature. An Arrhenius-plot of the recovery rate constant is shown in Fig. 5.9 for the 1.0 Ω cm samples of this study (filled symbols). For comparison, previously published data by Lim et al. [36] and Herguth et al. [84] on Cz-Si samples with a specific resistivity between 1 and 2 Ω cm are also displayed. Please note that the permanent recovery process was performed at different light intensities in the different studies. Up to now, the large difference in the rate constants determined by Lim et al. and Herguth et al. (more than one order of magnitude at comparable temperatures) was unclear. However, considering our results regarding the impact of an RTA treatment, we conclude that the difference in the sample processing of both groups caused this difference, as Herguth et al. performed an RTA step, while Lim et al. omitted the RTA step.

As shown in Fig. 5.9, the recovery rate constants R_{de} vary up to 3 orders of magnitude when the recovery is performed in a temperature range between 80 and 220 °C. Comparing different rate constants at a constant recovery temperature, it can be concluded from our new data that the last high-temperature process step has a crucial impact on the rate constant (apart from variations in the light intensity during the recovery process). The data is plotted here in the form of an Arrhenius-plot, as it has been concluded in previous publications [36, 84] that the process of permanent recovery is thermally activated. Assuming a simple thermally activated process, the recovery rate constant would follow a simple exponential law: $R_{de} = \nu \times \exp(-E_a/(k_b T))$, where ν is the attempt frequency, E_a the activation energy of the recovery process, k_b the Boltzmann constant and T the absolute temperature. However, as is shown in Fig. 5.9, our new data does not show a simple Arrhenius-law behaviour of the rate constant over the entire investigated temperature range. A possible explanation for the retarded increase of the rate constant towards higher temperatures could be that at elevated recovery temperatures (higher than $\sim 185\,^\circ$C) the lifetime after the process of permanent recovery is not completely stable under subsequent illumination. This suggests that another defect transition occurs in this temperature range and the increase of the lifetime during the process is promoted by at least two competing defect reactions. However, even at low temperatures (lower than $\sim 185\,^\circ$C) the dependence of R_{de} cannot be explained by a single-exponential function. Therefore, we conclude that the process of permanent recovery is not described by a simple thermally activated process and that the recovery process is of more complex nature. Also, previous data presented by Lim et al. [36] and Herguth et al. [84] support our findings.

5.1.4 Impact of illumination intensity during recovery

The material used for this investigation is $(165 \pm 10)\,\mu$m thick boron-doped Cz-Si with a resistivity of $\rho = (1.6 \pm 0.1)\,\Omega\,$cm and with an interstitial oxygen concentration of $[\mathrm{O}_i]= (7 \pm 0.5) \times 10^{17}\,\mathrm{cm}^{-3}$, determined via four-point-probe and FTIR measurements (IOC 88), respectively. The measured dependence of the recovery rate constant R_{de} on the illumination intensity P_{ill} is shown in Fig. 5.10 on a double-logarithmic scale. The orange circles correspond to results obtained on lifetime samples passivated with $\mathrm{Al_2O_3/SiN}_x$ stacks. All of these samples have been treated during RTA at 850 °C with a belt speed of 7.2 m/min and are permanently recovered at 185 °C. The blue diamonds correspond

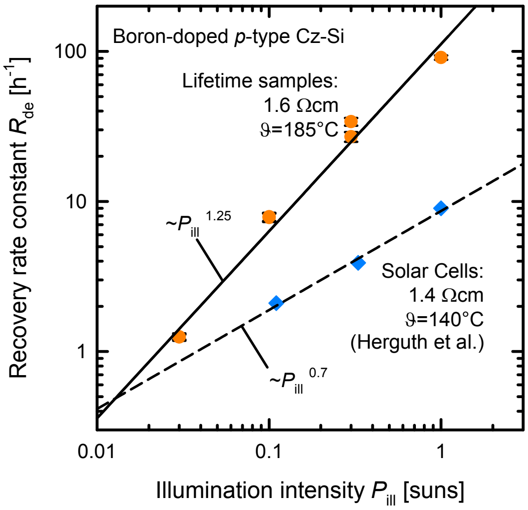

FIGURE 5.10: Recovery rate constant R_{de} plotted versus the illumination intensity P_{ill} during permanent recovery of lifetime samples with Al_2O_3/SiN_x stack and fired at $v_{belt} = 7.2\,m/min$ belt speed (orange circles) on a double-logarithmic scale. The recovery is performed at 185 °C. Blue diamonds correspond to data determined by Herguth et al. [35] at a temperature of 140 °C from solar cells. The black solid and dashed lines are power law fits to the respective data. Note that 1 sun corresponds to a light intensity of $100\,mW/cm^2$.

to recovery rate constants published by Herguth et al. [35] measured on solar cells using a recovery temperature of 140 °C. In both cases, an increasing rate constant with increasing illumination intensity is observed. From a power-law fit to the data, however, different exponents are extracted. For our lifetime data an exponent of (1.25 ± 0.06) is extracted, while for Herguth's data a value of (0.66 ± 0.06) is obtained. Despite the notable difference in the exponents of almost a factor of 2, the qualitative behaviour is comparable. Note that the recovery of the lifetime at elevated temperatures depends on the concentration of excess carriers, as it was shown by Herguth et al. [35]. As the concentration of excess carriers increases with the illumination intensity, the observed trend of an increasing rate constant R_{de} with increasing illumination intensity P_{ill} may be expected. However, if results on lifetime samples and solar cells are compared, it has to be taken into account that the change of the excess carrier concentration in the silicon bulk does not only depend on the illumination intensity, but also on the optical properties of the sample and on the overall (injection-dependent) lifetime of the sample during permanent recovery. Hence, these additional factors might explain the differences observed between the $R_{de}(P_{ill})$-dependence of the lifetime samples and the cell results of Herguth et al., shown in Fig. 5.10.

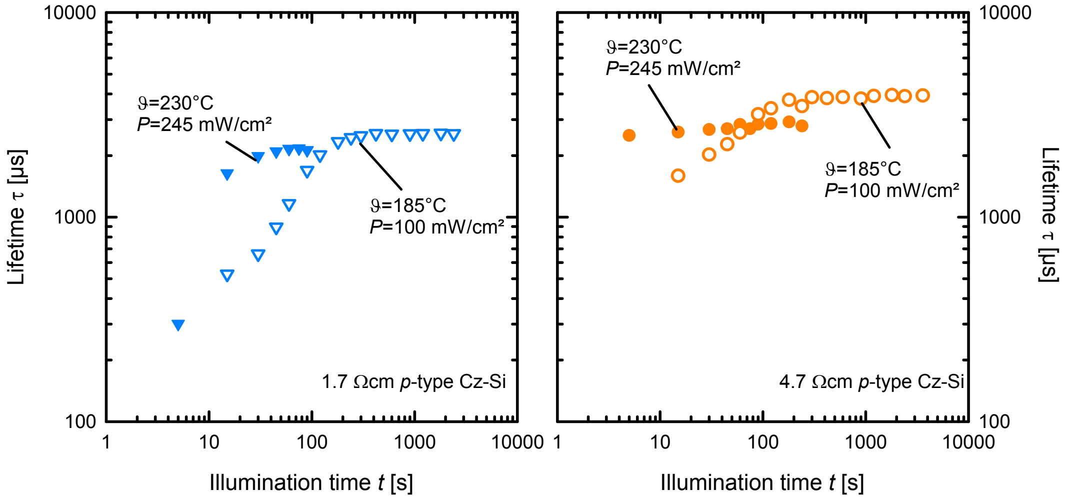

FIGURE 5.11: Measured lifetimes τ at a fixed injection density $\Delta n = 0.1 \times p_0$ as a function of illumination time t during the recovery process. Left, two curves of samples with a base resistivity of 1.7 Ω cm are shown, right two curves of samples made of 4.8 Ω cm material. Open symbols correspond to samples after annealing at 200 °C in darkness for 10 min and subsequently recovered at 185 °C and 100 mW/cm^2 light intensity. Filled symbols correspond to two samples after 250 °C annealing in darkness and recovered at 230 °C and 245 mW/cm^2 light intensity.

5.1.5 Recovery within seconds

For industrial applications it is important to reach the high lifetimes after permanent recovery τ_{0p} in an as short as possible time frame. Therefore, an optimized pre-treatment is required. In particular, a fast cooling ramp at 600 °C is very important to minimize the process time of the recovery process (see section 5.1.2). From previous studies it is known that increasing the recovery temperature (see [84] and also Fig. 5.9) as well as increasing the illumination intensity (see [35] and Fig. 5.10) during the recovery process further increases the recovery rate constant, i.e. shortens the recovery period. Additionally, it was shown by Wilking et al. [49] that an additional annealing step in darkness after the RTA treatment at intermediate temperatures between 200 °C and 400 °C leads to a further reduction of the recovery period. All these findings are included into our experiments described in this section. We anneal the samples after firing at 250 °C for 10 min in darkness and perform the recovery process at an elevated temperature of 230 °C at 245 mW/cm^2 light intensity. Two different Cz-Si materials with base resistivities of $\rho = 1.7\,\Omega\,$cm and $\rho = 4.7\,\Omega\,$cm are chosen. Again, the samples are P-diffused, with the diffused regions removed afterwards, and are coated with an Al_2O_3/SiN_x stack. During RTA the samples are treated with 850°C set peak temperature and 7.2 m/min belt speed.

Figure 5.11 shows the recovery behaviour of the lifetime during annealing under illumination for four samples. The filled symbols correspond to samples treated with our improved conditions, while the samples corresponding to the open symbols are annealed at 200 °C and recovered at 185 °C and 100 mW/cm^2 (1 sun) light intensity. Our improved conditions clearly further accelerate the recovery process. After only 10 s during the recovery process the lifetime of the 1.7 Ω cm Cz-Si material reaches values above 1 ms (see left graph in Fig. 5.11). On another sample with a higher resistivity of 4.7 Ω cm (circles in right graph of Fig. 5.11), which was also treated with our improved conditions, the typical degradation of the lifetime followed by its recovery is not observed. The lifetime remains apparently stable at values above 2.5 ms. As the first data point is measured after 5 s of recovery treatment, we conclude that the deactivation process is in fact already completed within the first 5 seconds. We have, hence, for the first time identified an industrially applicable (i.e. ultra-fast) treatment leading to lifetimes larger than 1 ms in conventional boron-doped Cz-Si.

5.1.6 Summary

In this section, we have examined the impact of rapid thermal annealing (RTA) on the carrier lifetime of boron-doped, oxygen-rich *p*-type Cz-Si wafers for three characteristic stages of light-induced degradation/recovery. The RTA step was performed in a belt-type firing furnace as typically used for the metallization of screen-printed silicon solar cells. By varying the peak temperature and the belt speed of the RTA treatment, significant differences in the lifetimes after complete degradation (τ_d), after dark annealing (τ_0), and after permanent recovery (τ_{0p}) were observed. On 1 Ω cm Cz-Si material we have found that the degraded lifetime can be improved by RTA from 42 μs to 107 μs. The permanently recovered lifetime can be improved even more dramatically: from 110 μs up to 2020 μs.

In addition, we discovered a very strong impact of the RTA treatment on the kinetics of the permanent recovery. Due to the RTA treatment, the recovery rate constant R_{de} (at the recovery conditions: $\vartheta = 185\,°\mathrm{C}$, $P_{ill} = 100\,\mathrm{mW/cm^2}$) increased from 1 h^{-1} to 75 h^{-1} for the highest applied belt speed of 7.2 m/min. We attribute the observed increase of R_{de} with increasing belt speed to an increased cooling rate at the end of the RTA step. We have identified the relevant temperature interval during cooling after RTA to be $\sim 600\,°\mathrm{C}$, as the recovery rate constant in that temperature interval shows a linear correlation with the cooling rate, i.e. $R_{de} \propto q$. A further experiment on a variety of Cz-Si materials featuring different base resistivities confirmed the validity of this important fundamental finding, which clearly favourites a recently proposed $\mathrm{B}_i\mathrm{B}_s\mathrm{O}_i$ model [47].

Our investigations of the recovery temperature on the lifetime after permanent recovery τ_{0p} revealed no dependence in the temperature range between 100 and 220 °C. In contrast, the rate constant R_{de} was found to be strongly dependent on the recovery temperature. However, R_{de} does not follow a simple Arrhenius-law, suggesting that the process of permanent recovery is more complex than a simple thermally activated process. Apart from the recovery temperature, we examined the impact of the illumination intensity on the recovery process. Our experiments clearly showed that the rate constant R_{de} also depends critically on the illumination intensity, for intensities below 1 sun. On the investigated samples, R_{de} increases following a simple power-law with an exponent of $a = 1.25$.

Our new experimental findings are discussed in the context of a previously proposed $\mathrm{B}_i\mathrm{B}_s\mathrm{O}_i$ model (see section 2.3.3.3) for the lifetime-degrading recombination centres. Within this model, various B_i-containing complexes exist —in the initial stage of sample cooling from a high temperatures ϑ— in equilibrium with boron nano-precipitates (B-NPs). At lower temperature the equilibrium is no longer supported and a specific concentration of $\mathrm{B}_i\mathrm{B}_s\mathrm{O}_i$ is frozen-in. This concentration is expected to be smaller at higher cooling rates, as was also observed in our experiments. The sinking ability of the B-NPs (the product of their density and the radius) is predicted to be simply proportional to the cooling rate referring to a specific temperature of B-NP nucleation. From our experimental results it is hence concluded that this nucleation temperature is around 600 °C. The rate constant R_{de} for the permanent recovery is proportional to the B-NP sinking efficiency – and thus to the cooling rate q.

In the last part of this section we combined all measures to increase the rate constant R_{de} as discussed before. This led to ultra-short industrially feasible process times in a time frame of 5 s to 10 s, opening the path for implementing our recovery process to industrial solar cell production.

5.2 Impact of hydrogen on the deactivation process

In a series of three different experiments we examine the impact of hydrogen on the BO deactivation. In the first experiment, different dielectric passivation layers featuring largely different hydrogen concentrations are applied to the Cz-Si wafers. The impact of the various hydrogen contents in combination with high-temperature firing on the lifetime is then examined. In the second experiment, the cooling of the lifetime samples after a high-temperature treatment is varied without any hydrogen-rich dielectric layer being present. The surface passivation is carried out after the sample cooling, so that an equally small amount of hydrogen is incorporated into each sample. In the final experiment, a low-temperature passivation (the maximum temperature applied is 130 °C) based on depositing the polymer PEDOT:PSS is applied, which virtually completely omits the in-diffusion of hydrogen from the passivation layer into the silicon bulk.

For our experiments we use wafers from three different boron-doped Cz-grown silicon ingots. The wafers feature base resistivities of $(1.0 \pm 0.03)\,\Omega\,\mathrm{cm}$, $(1.6 \pm 0.1)\,\Omega\,\mathrm{cm}$, and

$(2.5 \pm 0.03)\,\Omega\,\text{cm}$, as determined via four-point-probe measurements and have a final thickness after processing of $(165 \pm 10)\,\mu\text{m}$.

5.2.1 Dielectric passivation layers with varying hydrogen content

5.2.1.1 Experimental details

Sample processing starts with the removal of the surface damage using a solution of potassium hydroxide (KOH) followed by a RCA cleaning sequence. Afterwards, a phosphorus diffusion is performed at 850 °C for 70 minutes, which results in n^+ layers with a sheet resistance of $(100 \pm 10)\,\Omega/_\square$ on both wafer surfaces. After the removal of the phosphosilicate glass (PSG) in hydrofluoric acid (HF), the phosphorus-doped n^+-regions are removed from both wafer surfaces, again using KOH. In the following, two different surface passivation schemes are applied which feature very different hydrogen concentrations. Within the first group of samples, 20 nm Al_2O_3 are deposited on both wafer surfaces via plasma-assisted atomic layer deposition (plasma-ALD) in a FlexAL tool (Oxford Instruments). In the second group, a 10 nm Al_2O_3 layer, also deposited via plasma-ALD, is covered by a 70 nm thick SiN_x (n_r=2.05) layer deposited via plasma-enhanced chemical vapour deposition (PECVD) using a Roth & Rau SiNA system. Please note that the hydrogen content of the Al_2O_3 and the SiN_x layers differ by about one order of magnitude between 12 to 20 at.% [85] for the SiN_x layer and between 1 to 2 at.% [86] for the Al_2O_3 layer. After the deposition of the dielectric layers, all samples underwent a fast firing step in a conventional belt-firing furnace (Centrotherm DO-FF-8.600-300) with a set peak temperature of $\vartheta_{Peak} = 850°\text{C}$ at various belt speeds between 1.2 and 7.2 m/min. The temperature profiles are measured on identically processed samples, using a DATAPAQ Insight Oven Tracker. Afterwards, the lifetime measurements are performed and the permanent deactivation of the BO centre is performed at a temperature of 185 °C and at a light intensity of 100 mW/cm^2. As illumination source a halogen lamp is used. To start the deactivation process from a defined state of the BO defect, all samples are annealed at 200 °C for 10 min in darkness directly before the deactivation process is performed.

5.2.1.2 Results and discussion

In Fig. 5.12, the regeneration curves of two lifetime samples passivated with single Al_2O_3 layers and fired at 850 °C set peak temperature with two different belt speeds are shown. The orange circles correspond to a sample fired at a belt speed of 7.2 m/min, while the blue squares correspond to a sample fired at a belt speed of only 1.2 m/min.

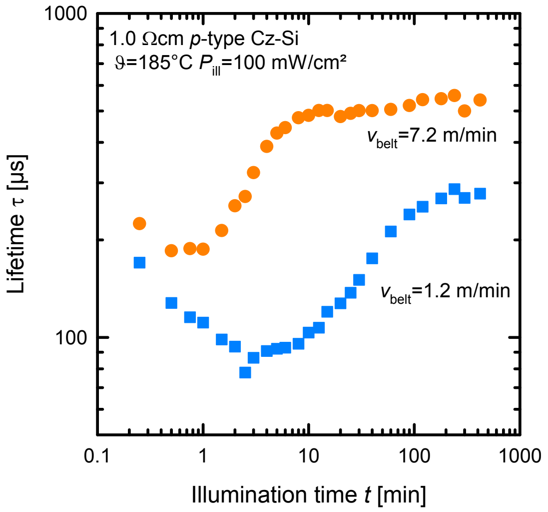

FIGURE 5.12: Recovery of the effective lifetime τ plotted versus the illumination time t at 185 °C and 100 mW/cm^2 (1 sun) light intensity. A fast belt speed ($v_{belt} = 7.2$ m/min, orange circles) leads to a fast recovery of the lifetime, while for a slow belt speed ($v_{belt} = 1.2$ m/min, blue squares) a longer recovery time is needed.

Comparing the saturated lifetimes of the sample treated with the fastest belt speed with the results obtained on samples passivated with a stack of Al_2O_3/SiN_x on various Cz-Si materials (see section 5.3), we observe that the saturated lifetime with a single Al_2O_3 layer is significantly lower compared to that with SiN_x capping layer, the latter ones being larger than 1 ms. This suggests that a hydrogen-rich layer during the firing step is indeed required in order to obtain very high lifetimes ($>$ 1 ms). However, the same kinetics for the recovery process, independent of the hydrogen content in the dielectric passivation layer, is observed. As can be seen in Fig. 5.12, for the fast belt speed, the lifetime clearly regenerates much faster compared to the sample treated with the slow belt speed.

In order to evaluate these different recovery behaviours quantitatively, we extract the recovery rate constants R_{de} using Eqn. 2.1. The rate constant R_{de} is then determined by fitting the time-resolved effective defect concentration N_t^* with a single-exponential decay function: $N_t^* = A \times \exp(-R_{de} \times t) + B$. The rate constants R_{de} of all samples, passivated with a single Al_2O_3 layer and treated with different belt speeds, are compared to the extracted values of the recovery rate constants of samples treated identically which, however, are passivated with an Al_2O_3/SiN_x stack (see Fig. 5.5). The result of this comparison is shown in Fig. 5.13, where the extracted recovery rate constant R_{de} is plotted versus the measured cooling rate q at 600 °C after the firing step at $\vartheta_{Peak} = 850$ °C. Compared to the samples fired with the Al_2O_3/SiN_x stack, the samples passivated with a single Al_2O_3 layer also show a linearly increasing rate constant with increasing cooling rate after firing. The comparison at equal cooling rates clearly shows that the recovery rate constants R_{de} are quite comparable between the two sample types.

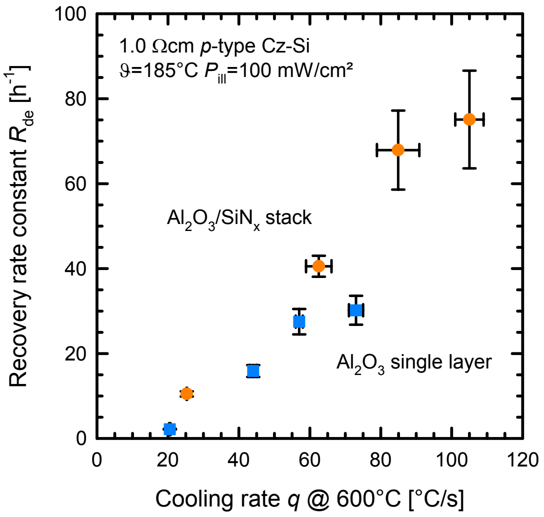

FIGURE 5.13: Recovery rate constant R_{de} plotted versus the cooling rate q at 600°C after firing. The blue squares correspond to the rate constants determined from the single-layer Al_2O_3 passivated samples, while the orange circles correspond to samples passivated with an Al_2O_3/SiN_x stack (see Fig. 5.5).

The rate constants for the samples with single Al_2O_3 layer tend to be slightly below the R_{de} values determined for the Al_2O_3/SiN_x-passivated samples. However, this can be explained by the different optical properties of the dielectric layers, resulting in different reflectivities and hence different excess carrier concentrations at the same illumination intensity (see section 5.1.4). That is, the slight difference between the two sample types in Fig. 5.13 can be attributed to the overall lower excess carrier concentration in the Al_2O_3-passivated Cz-Si samples under the same regeneration conditions. First, the reflectivity considerably varies between the two sample groups. At a wavelength of 1000 nm, which is the dominating wavelength in our halogen lamp spectrum, the reflectivity of the Al_2O_3-passivated samples is calculated to be approximately 32 % using the OPAL 2 ray tracer [87]. The reflectivity of the Al_2O_3/SiN_x-passivated samples is only about 13 %. Second, the observed lifetime of these samples is significantly lower at room temperature compared to the samples passivated with the Al_2O_3/SiN_x stack.

Hence, we draw the important conclusion that the different hydrogen contents in the silicon bulk do not have a major impact on the kinetics of the BO deactivation process.

5.2.2 Variation of the sample cooling rate without any hydrogen source present

5.2.2.1 Experimental details

In this experiment, the samples are split up into 4 different groups. Groups 1 and 2 undergo a phosphorus diffusion at 850 °C for 50 minutes. Group 1 is removed from

the tube furnace at 800 °C, while group 2 remains within the furnace in a nitrogen atmosphere until the furnace is cooled down to 250 °C. In total, the cooling down to 250 °C takes 215 min. Groups 3 and 4 undergo an annihilation step for thermal donors (TDs) in a quartz-tube furnace at 650 °C for 30 min in a nitrogen atmosphere. The third group is immediately removed from the tube furnace at 650 °C to realize a high cooling rate, while group 4 remains within the tube furnace until it is cooled down to 250 °C, which takes 180 min in total. Afterwards, all samples are passivated with Al_2O_3 deposited via thermal-ALD in a FlexAL system. The deposition of the Al_2O_3 layers as well as the activation of the passivation layers, performed on a hotplate in ambient air for 15 min, are performed at a maximum temperature of 260 °C. The layer deposition takes 36 min per side.
From literature it is well known that the diffusion of hydrogen in oxygen-rich silicon ($[O_i] \approx 8 \times 10^{17}\,\mathrm{cm}^{-3}$, which is a typical value for today's Cz-Si) is trap-limited [52, 88]. Hence, it must be assumed that even at deposition times of 72 min in total, the diffusion of hydrogen is limited to the first $\sim 20\,\mu$m of the silicon bulk [52, 89, 90]. Because of the trap-limited diffusion of hydrogen, the in-diffusion of hydrogen into the silicon bulk at even lower temperatures (and shorter time spans), e.g. during wet chemical processing, can be neglected as well.

The permanent deactivation of the BO centre is performed at a temperature of 185 °C and a light intensity of $100\,\mathrm{mW/cm^2}$, again using a halogen lamp as light source. To start the deactivation process from a defined state of the BO defect, the permanent deactivation is performed after all samples have been illuminated at room temperature for 60 hours (i.e. from the fully degraded state).

5.2.2.2 Results and discussion

In Fig. 5.14, the kinetics of the BO deactivation in terms of the effective lifetime are shown for four different lifetime samples, which are cooled down rapidly (orange circles) or very slowly (blue triangles) after the TD annihilation step. During the high-temperature TD annihilation (performed at 650 °C) no dielectric layers are present on the wafer surfaces, i.e. no hydrogen is incorporated into the silicon bulk. As can be seen from Fig. 5.14, the time span until the lifetime saturates depends critically on the sample cooling, even if there is no hydrogen present during the cooling of the samples. Again, the same trend can be observed: a fast cooling results in a fast recovery of the lifetime, while a slow cooling results in a slow recovery. Additionally, our previous result (see section 5.1) that the achievable lifetime after the recovery process τ_{0p} increase with increasing cooling rate is also confirmed. For the fast cooled samples we

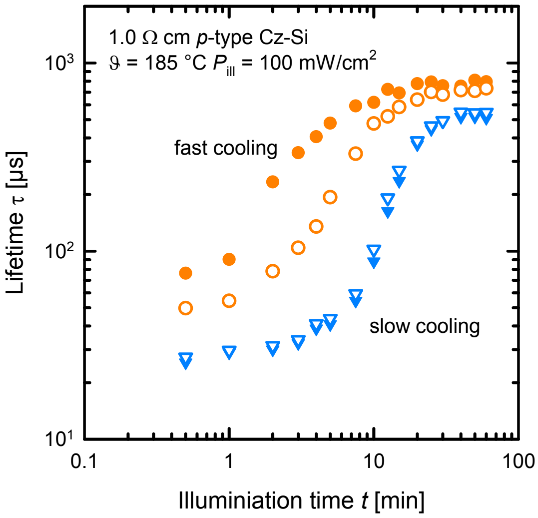

FIGURE 5.14: Lifetime τ plotted versus the illumination time t at 185°C recovery temperature and $100\,\mathrm{mW/cm^2}$ (1 sun) light intensity. Orange circles correspond to two samples with a fast cooling after the last high temperature treatment (TD annihilation) at 650°C, while the blue triangles correspond to two samples with a slow cooling. No hydrogen-containing dielectric layer has been present during the high-temperature anneal.

measured a lifetime $\tau_{0p} = 738 \pm 52\,\mu$s, while for the slowly cooled samples we measured $\tau_{0p} = 520 \pm 23\,\mu$s.

In Fig. 5.15, the extracted recovery rate constants R_{de} are shown for different annealing treatments and Cz-Si materials. The orange circles correspond to samples annealed at 850 °C, while the blue squares correspond to samples annealed at 650 °C. In all cases,

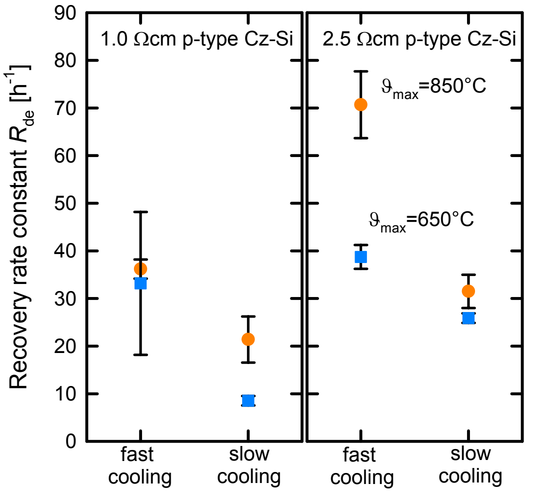

FIGURE 5.15: Recovery rate constant R_{de} for different samples cooled w/o hydrogen being present. Two different base resistivities are shown: left $1\,\Omega$ cm, right $2.5\,\Omega$ cm. Orange circles correspond to samples annealed at 850 °C in the last high temperature process, blue squares to samples annealed at 650 °C.

a high rate constant for the rapidly cooled samples and a reduced rate constant for samples after a slow cool down is found. This result further supports our interpretation that the thermal history and especially the cooling of the samples after the last high-temperature step is of major importance for the dynamics of the BO deactivation process. Concerning the influence of hydrogen, it has to be pointed out that the amount of hydrogen introduced into the silicon is extremely small and in particular it is exactly the same for all examined samples in this experiment, as the same Al_2O_3 surface passivation layer, which is the only source of hydrogen, is applied after the last high-temperature treatment. Still, the recovery rate constant varies up to a factor of three between fast and slowly cooled samples, clearly proving that the cooling rate and not the hydrogen content is the most crucial parameter.

5.2.3 Polymer-based surface passivation at temperatures $\leq 130\,°\mathrm{C}$

5.2.3.1 Experimental details

After the removal of the surface damage, a phosphorus diffusion is performed at 850°C for 70 min. After diffusion, the PSG as well as the diffused n^+-regions are removed using HF and KOH, respectively. The surface passivation is then realized by poly(3,4-ethylenedioxythiophene):poly(styrenesulfonate) (PEDOT:PSS) which is deposited using a spin-on technique [91]. PEDOT:PSS is a transparent hole-conducting polymer which allows to achieve low saturation current densities of $J_0 = 80\,\mathrm{fA/cm^2}$ on c-Si [92]. Before PEDOT:PSS deposition, all samples are illuminated at room-temperature and a light intensity of $P_{ill} = 10\,\mathrm{mW/cm^2}$ for more than 48 hours to fully degrade the lifetime. After PEDOT:PSS deposition, the samples are dried on a hotplate at 130 °C for up to 11 hours under illumination, using a halogen lamp of approximately $200\,\mathrm{mW/cm^2}$ light intensity. Under these conditions, the PEDOT:PSS is dried and the BO defect is deactivated at the same time.

5.2.3.2 Results and discussion

Within this experiment, unfired Cz-Si samples are exposed to the recovery conditions (in this case 130 °C and 2 suns light intensity) for defined time intervals. In Fig. 5.16, the injection-dependent lifetimes of four samples are shown which are recovered for different time intervals. The red curve corresponds to the lifetime before recovery. The light blue, dark blue and green curves correspond to the lifetime of samples exposed to the recovery conditions for 2, 4 and 6 hours, respectively. While for the red curve the pronounced injection dependence typical of the BO-related defect is observed, the injection dependence weakens with increasing time interval under recovery conditions. At increased injection densities ($\Delta n > 10^{16}\,\mathrm{cm}^{-3}$), the lifetime is limited by a saturation current density of $J_0 = 80\,\mathrm{fA/cm}^2$ provided by the PEDOT:PSS/c-Si interface. This J_0 value is also confirmed by our lifetime measurements on $1.3\,\Omega\mathrm{cm}$ boron-doped float-zone (FZ) silicon wafers processed in parallel. As the measured effective lifetime at high injection densities of the samples shown in Fig. 5.16 is strongly influenced by recombination at the surfaces, the bulk lifetime τ_b of the Cz-Si material is extracted by determining the saturation current density J_0 of the PEDOT:PSS/c-Si interface in the high-injection regime and subtracting its influence from the measured effective lifetime τ using the equation:

$$\tau_b = \left(\frac{1}{\tau(\Delta n)} - \frac{2 \times J_0(\Delta n + p_0)}{q_e n_i^2 W} \right)^{-1}, \tag{5.2}$$

with q_e being the elementary charge, n_i the intrinsic carrier concentration and W the sample thickness. Please note that this equation only holds if the injection dependence of the PEDOT:PSS surface passivation can indeed be expressed by a single J_0 value, which will be assumed in the following. From the lifetime measurements on FZ reference samples it is known that this is a reasonable assumption. However, even if the assumption does not hold, the extracted bulk lifetimes can be considered as a lower limit for the actual bulk lifetime.

In Fig. 5.17, an example for the extraction of the bulk lifetime τ_b from the measured effective lifetime τ for a Cz-Si sample exposed for 2 hours to the regeneration conditions

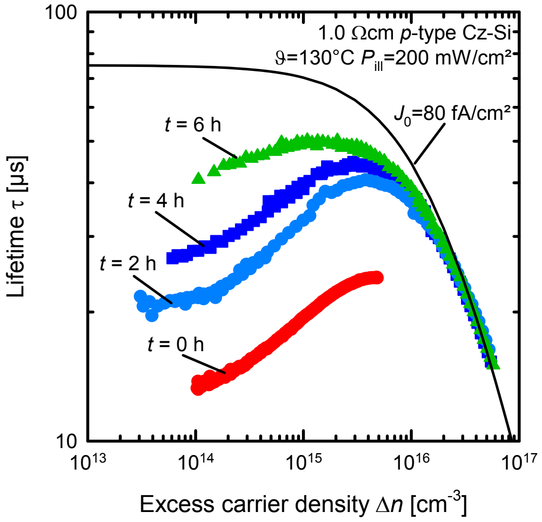

FIGURE 5.16: Injection-dependent carrier lifetime $\tau(\Delta n)$ of PEDOT:PSS-passivated samples, exposed between 2 and 6 hours to the recovery conditions at a temperature of 130 °C and 2 suns light intensity. The red curve corresponds to the injection-dependent lifetime before the recovery process is applied. The black solid line corresponds to the lifetime limited by a saturation current density of $J_0 = 80\,\mathrm{fA/cm}^2$.

is displayed. At low injection levels, $\Delta n < 5 \times 10^{14}\,\mathrm{cm}^{-3}$, the bulk lifetime can be determined quite accurately. However, at higher injection conditions ($\Delta n > 10^{15}\,\mathrm{cm}^{-3}$), the uncertainty in the extracted τ_b is larger compared to the determined bulk lifetime itself. In the following, we perform this analysis for all investigated time spans and extract the bulk lifetimes in the low-injection regime at a fixed injection density of $\Delta n = 2 \times 10^{14}\,\mathrm{cm}^{-3}$. The result of this analysis is shown in Fig. 5.18 where the extracted bulk lifetime τ_b is plotted versus the recovery time t. As can be seen by the black dashed line (guide to the eyes), the bulk lifetime clearly increases with recovery time. Moreover, the recovery of the lifetime proceeds in a time frame which is comparable to the recovery of a lifetime sample without RTA treatment and passivated with a single Al_2O_3 layer (blue squares), deposited via a thermal-ALD process (see section 5.2.2). For the latter sample, the recovery is performed at a temperature of 130 °C and a light intensity of $100\,\mathrm{mW/cm}^2$. Despite the strong scatter in the data obtained from the samples passivated with PEDOT:PSS, the lifetime seems to saturate after ∼ 6 hours, i.e. slightly faster than the sample passivated with Al_2O_3. This difference might be attributed, at least partially, to the increased light intensity ($200\,\mathrm{mW/cm}^2$) during regeneration of the PEDOT:PSS-passivated sample. This result further supports that the deactivation of the BO defect does not require any hydrogen. Especially, a fast-firing step with a hydrogen-rich dielectric layer is not required for the BO deactivation. Hence, we conclude from our experiments that hydrogen is not a necessary prerequisite for the BO deactivation. Advanced BO defect models should hence not rely on the presence of

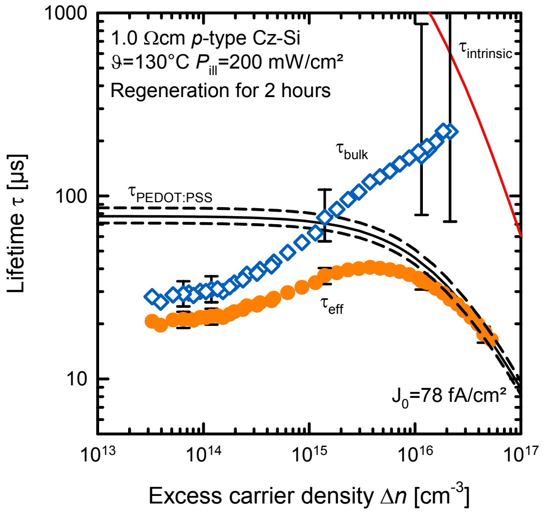

FIGURE 5.17: Lifetime $\tau(\Delta n)$, extracted from the measured effective lifetime τ and the saturation current density J_0 at the surfaces, for a PEDOT:PSS-passivated sample exposed for 2 hours to the recovery conditions. Orange circles show the measured effective lifetime while the open blue diamonds represent the extracted bulk lifetime. The black solid line is the lifetime limit described by a saturation current density of $J_0 = 78\,\mathrm{fA/cm}^2$.

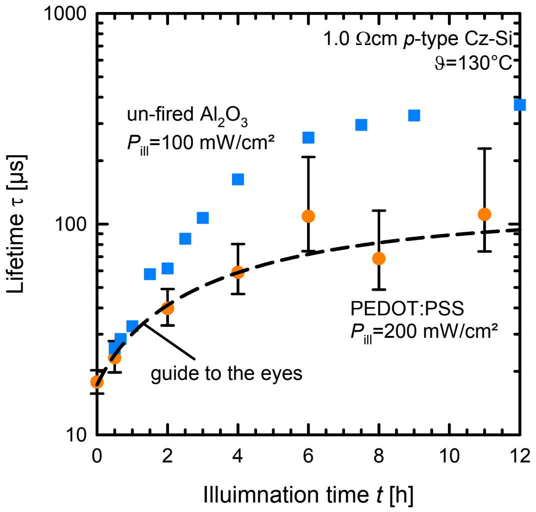

FIGURE 5.18: Lifetime $\tau(\Delta n = 2 \times 10^{14})\,\mathrm{cm}^{-3}$ plotted versus the illumination time t. The orange circles show the increasing bulk lifetimes of the samples passivated with PEDOT:PSS with increasing recovery time. The black dashed line is a guide to the eyes. For comparison, the effective lifetime τ of a sample passivated with Al_2O_3 (blue squares) is also displayed.

hydrogen in the silicon bulk during permanent deactivation.

5.2.4 Summary

We have performed three different experiments with the intention to separate the effects of hydrogen and thermal history on the kinetics of the permanent deactivation of boron-oxygen-related recombination centres in crystalline silicon.

In the first experiment, it was shown that the recovery kinetics of the lifetime under illumination at elevated temperatures are not affected by different hydrogen contents in the dielectric layers, deposited onto the sample surfaces prior to a high-temperature fast-firing process. However, omitting any hydrogenation (via fast-firing with a hydrogen-rich dielectric layer being present) no lifetimes in excess of 1 ms have been achieved. This result might be interpreted in terms of an effective hydrogen passivation of background defects of yet unidentified nature.

In the second experiment, we have examined the influence of sample cooling after the last high-temperature treatment without the presence of hydrogen. A surface passivation based on Al_2O_3 at a maximum temperature of 260 °C was deposited onto the surfaces only *after* the high-temperature step. Our experimental results clearly revealed the crucial importance of the sample cooling on the kinetics of the recovery process. Moreover, even with exactly the same, very low hydrogen content in the silicon bulk, a pronounced recovery of the lifetime in all cases with the kinetics depending on the sample cooling was observed.

In the last experiment, we observed a pronounced permanent recovery of the lifetime even without any hydrogen in-diffusion into the silicon bulk. This result is based on a low-temperature (maximum temperature 130 °C) surface passivation using the polymer PEDOT:PSS.

Summarizing our experiments, the results clearly prove for the first time that hydrogen introduced from dielectric layers present during high-temperature treatments is not responsible for the observed permanent recovery of the lifetime in boron-doped Czochralski-grown silicon upon illumination at elevated temperature. However, in order to obtain very high lifetimes, we found that a hydrogen-rich dielectric layer as well as a fast-firing step are required, which we attribute to the hydrogen passivation of up to now unknown background defects.

5.3 Lifetime parameterization after complete BO deactivation and the impact on solar cell performance

The following section is subdivided into two parts. In the first part, the maximum stable lifetimes which can be achieved after permanent deactivation of the boron-oxygen defect centre will be analysed and parameterized. In the second part, we examine the impact of these lifetimes on the performance of next-generation industrial-type passivated emitter and rear solar cells (PERC).

5.3.1 Parameterization of the lifetime after BO deactivation

In order to examine the achievable lifetimes after permanent recovery as a function of the boron doping concentration, five different commercially available boron-doped Cz-Si materials with resistivities between 0.5 Ω cm and 5 Ω cm were processed into lifetime samples. The measured interstitial oxygen concentration $[O_i]$, determined via FTIR measurements (IOC 88), varies between 5×10^{17} and $10 \times 10^{17}\,\mathrm{cm}^{-3}$, representing a typical range for Cz-Si material.

5.3.1.1 Experimental details

Sample processing includes the removal of the surface damage using an aqueous solution of KOH which is followed by a standard RCA cleaning sequence. Afterwards, all samples undergo a phosphorus diffusion (850 °C, 1 h) resulting in a sheet resistance of the diffused n^+-regions of $\rho_{sheet} \approx 100\,\Omega/\square$. After the removal of the phosphosilicate glass using HF, the n^+-diffused regions are removed using KOH. After RCA cleaning, the wafer surfaces are passivated by a stack of aluminum oxide (Al_2O_3) and silicon nitride (SiN_x) [78]. 10 nm of Al_2O_3, deposited via plasma-assisted atomic layer deposition (plasma-ALD) using an Oxford Instruments FlexAL reactor, are deposited underneath a 70 nm thick SiN_x layer (refractive index $n_r = 2.05$) which is deposited by plasma-enhanced chemical vapor deposition (PECVD) using a Roth & Rau SiNA system. After deposition of the dielectric passivation layers, the samples undergo a fast-firing step in a commercially available belt firing furnace (Centrotherm). For the determination of the ultimate lifetime limit, the firing parameters are set at a peak temperature of 850 °C and a maximum belt speed of 7.2 m/min (see section 5.1.2). Please note that the actual peak temperature of the wafer, which is measured using a temperature probe attached to lifetime samples of the same material processed in parallel, is only in the range of (775 ± 20) °C.

After sample processing, the permanent BO deactivation is performed by illuminating the samples at a light intensity of 100 mW/cm^2 using a halogen lamp. The samples were placed on a hotplate at various temperatures between 130 and 230 °C during illumination. As shown previously (see section 5.1.3), in contrast to the belt speed the temperature of the permanent recovery process does not affect the lifetime reached after the recovery process in the applied temperature interval.

5.3.1.2 Results and discussion

The maximum effective lifetimes reached after completing the deactivation process, i.e. after full deactivation of the BO defect, are shown in Fig. 5.19 (green circles) as a function of the doping concentration p_0. On lifetime samples processed in parallel on 1.3 Ω cm boron-doped float-zone silicon (FZ-Si) as well as on 0.8 Ω cm gallium-doped Cz-Si surface recombination velocities below 1 cm/s were extracted. Therefore, it is assumed that the measured effective lifetimes equal the bulk lifetimes of the examined boron-doped Cz-Si materials. Please note that this may underestimate the actual bulk lifetime if the assumption does not hold. In that case, the lifetimes measured here have to be considered as a lower limit to the bulk lifetime. For comparison, the intrinsic lifetime limit, as recently published by Richter et al. (solid black line) [60], as well as the lifetime limit after permanent deactivation (but without fast-firing process), as previously published by Schmidt et al. (dashed blue line) [93] are also shown in Fig. 5.19. Please note, that if no recovery process is applied, the lifetime after complete degradation is represented by the orange dashed-dotted line according to the parameterization by Bothe et al. [27] for a typical interstitial oxygen concentration of $[O_i]=7.5 \times 10^{17}\,\mathrm{cm}^{-3}$. In this case, an enhancement factor of 2 was multiplied to the lifetime parameterization of Ref. [27],

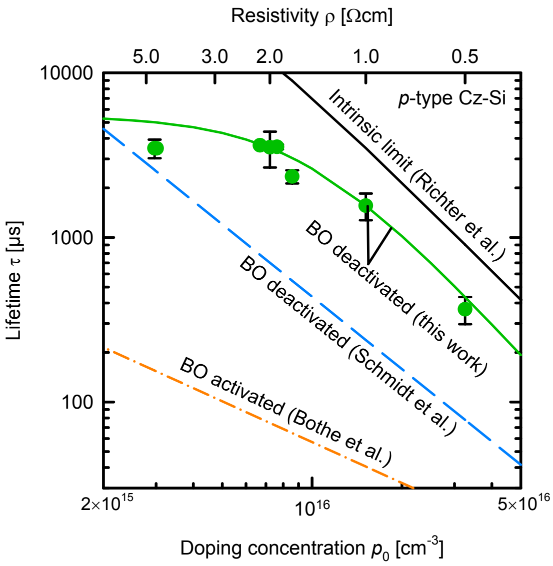

FIGURE 5.19: Measured lifetimes τ at a fixed injection density of $\Delta n = 0.1 \times p_0$ after permanent deactivation (green circles) versus doping concentration p_0. For comparison, the lifetime parameterization after complete degradation according to Bothe et al. [27] (orange dashed-dotted line), the lifetime parameterization after permanent deactivation according to Schmidt et al. [93] (blue dashed line) as well as the intrinsic lifetime limit according to Richter et al. [60] (black solid line) are also displayed. The green solid line gives the dependence of the lifetime after permanent deactivation according to our new proposed parameterization shown in Eqn. 5.3.

accounting for the phosphorus diffusion the samples underwent during processing. However, the actual lifetimes after complete degradation depend also critically on the fast firing process (see Fig. 5.2), which leads to an additional significant lifetime improvement (see section 5.1.2). Therefore, the low lifetimes shown as orange dash-dotted line in Fig. 5.19 can be considered as worst-case scenario.

The lifetimes achieved in this thesis significantly exceed the previously published lifetimes on boron-doped Cz-Si. Note that for the technologically important materials with resistivities around 1 Ωcm, the lifetimes measured in this thesis are a factor of 20 larger than predicted by the previous lifetime limit of Ref. [93] represented by the dashed blue line in Fig. 5.19. The main difference of the samples presented here compared to the previous parameterization is the presence of the optimized fast-firing step, which we have identified to be required to reach maximum lifetimes after permanent recovery.

The dependence of the lifetime τ_{0p} after permanent deactivation of the BO centre on the hole concentration p_0, at a fixed injection density of $\Delta n = 0.1 \times p_0$, is well described by our new parameterization (solid green line in Fig. 5.19):

$$\tau_{0p}(\Delta n = 0.1 \times p_0) = \left(\frac{1}{\tau_1} + \frac{1}{\tau_2}\right)^{-1} = \left(\frac{1}{5500\,\mu\text{s}} + \frac{p_0^2}{5 \times 10^{35}\,\text{cm}^{-6}\mu\text{s}}\right)^{-1} \tag{5.3}$$

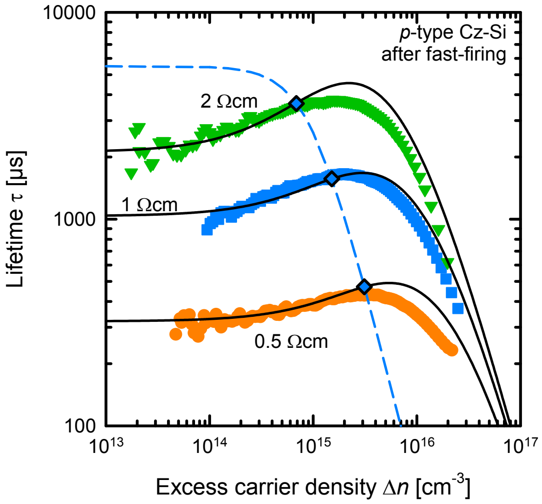

FIGURE 5.20: Measured injection-dependent carrier lifetime $\tau(\Delta n)$ of three differently doped materials (coloured symbols). The blue dashed line is the dependence described by the novel parameterization (Eqn. 5.3). The black solid lines are calculated using the SRH equation and assuming a single-level recombination centre at mid-gap with a capture cross section ratio $\sigma_n/\sigma_p = 12$, including the intrinsic lifetime limit.

In addition to the lifetime values at the fixed injection level of $\Delta n/p_0 = 0.1$, our data also allows to extract the complete injection dependence of the lifetimes after permanent recovery. The full injection dependence of the lifetimes can be quite well described by a single Shockley-Read-Hall (SRH) [61, 62] recombination centre in addition to the intrinsic lifetime limit (including Auger and radiative recombination) according to Ref. [60]. The SRH centre is located in the middle of the silicon band gap and the electron-to-hole capture cross section ratio is $\sigma_n/\sigma_p = 12$. Please note that the lifetime analysis performed here is not intended to comprehensively describe the defect physics involved in the deactivation process but to systematically describe the measured lifetime curves in the low-injection regime relevant to solar cell operation.

In general, the SRH lifetime of a single-level centre is described by the expression shown in Eqn. 3.9. The capture time constants are inversely proportional to the respective capture cross section, thus $\tau_{n0}/\tau_{p0} = \sigma_p/\sigma_n = 1/12$ in our case. Restricting the analysis to excess carrier concentrations of $\Delta n \gg 10^{10}\,\mathrm{cm}^{-3}$ and exploiting the fact that in our case the defect energy level is assumed to be in the middle of the band gap ($p_1 \ll p_0+\Delta n$ and $n_1 \ll \Delta n$), the SRH lifetime for p-type silicon ($p_0 \gg n_0$) can be written as [65]:

$$\begin{aligned} \tau_{SRH}(p_0, \Delta n) &= \frac{\tau_{p0} \times \Delta n + \tau_{n0} \times (p_0 + \Delta n)}{p_0 + \Delta n} \\ &= \tau_{p0} \times \left(\frac{1}{\eta_i^{-1} + 1} + \frac{\tau_{n0}}{\tau_{p0}} \right) \\ &= \tau_{p0} \times \left(\frac{1}{\eta_i^{-1} + 1} + \frac{1}{12} \right) \end{aligned} \qquad (5.4)$$

with $\eta_i \equiv \Delta n/p_0$ being the injection level. A fixed injection level of $\eta_i = 0.1$ leads to:

$$\tau_{SRH}(\eta_i = 0.1) = \frac{23}{132} \times \tau_{p0}. \tag{5.5}$$

Using this equation, as well as the expression for the measured lifetime $\tau^{-1}(\eta_i) = \tau_{int}^{-1}(\eta_i) + \tau_{SRH}^{-1}(\eta_i)$ with τ_{int} being the intrinsic lifetime, the hole capture time constant τ_{p0}, determined at a constant injection-level of $\eta_i = 0.1$, is obtained:

$$\tau_{p0} = \frac{132 \times \tau_{SRH}(\eta_i = 0.1)}{23} = \frac{132}{23}\left(\frac{1}{\tau(\eta_i = 0.1)} - \frac{1}{\tau_{int}(\eta_i = 0.1)}\right)^{-1}. \tag{5.6}$$

Hence, the complete injection-dependent lifetime is given by inserting Eqn. 5.6 into Eqn. 5.4:

$$\tau_{SRH}(p_0, \eta_i) = \left(\frac{1}{\tau(\eta_i = 0.1)} - \frac{1}{\tau_{int}(\eta_i = 0.1)}\right)^{-1} \times \left(\frac{132}{23 \times (\eta_i^{-1} + 1)} + \frac{11}{23}\right). \tag{5.7}$$

For the intrinsic lifetime τ_{int} the parameterization by Richter et al. is used, which is given for materials with $p_0 < 6 \times 10^{16}\,\mathrm{cm}^{-3}$ (i.e. for resistivities exceeding $0.3\,\Omega\mathrm{cm}$) by [60]:

$$\tau_{int} = \frac{\Delta n}{np(8.7 \times 10^{-29}\, n_0^{0.91} + 6.0 \times 10^{-30}\, p_0^{0.94} + 3.0 \times 10^{-29} \Delta n^{0.92} + B_{low})} \tag{5.8}$$

with $B_{low} = 4.73 \times 10^{-15}$. Please note that the electron and hole densities must be given per cubic centimetre in order to obtain the intrinsic lifetime in the unit of seconds. All the measured injection-dependent lifetimes after permanent recovery in this study are well described by this parameterization. An example is given in Fig. 5.20 which shows the injection-dependent lifetimes of three differently doped samples with resistivities ranging from 0.5 to $2.0\,\Omega\,\mathrm{cm}$. The calculated lifetimes using Eqn. 5.7 (black solid lines) are in good agreement with the measured injection-dependent lifetimes of the three exemplary materials, especially in the low-level-injection regime. At higher injection densities one might speculate about the influence of another defect close to edges of the band gap, which is frequently observed on lifetime samples (see also section 4.3) and might originate from recombination at the surface.

5.3.2 Implications of lifetime parameterization on solar cell performance

In order to examine the impact of our new lifetime parameterization on the performance of next-generation industrial silicon solar cells, we perform two-dimensional device simulations using the Quokka simulation tool [94], which is based on the conductive boundary model introduced by Brendel [95]. **P**assivated **E**mitter and **R**ear solar **C**ells (PERC) are simulated with a total thickness of 180 μm and a homogeneous frontside n^+-diffusion with a sheet resistance of 80 $\Omega/\square$. A schematic of the simulated cell structure is shown in Fig. 5.21. Furthermore, a random-pyramid front texture is assumed, which is coated by a 70 nm thick SiN_x layer (refractive index $n_r = 2.03$). The line width of the metal finger on the front side is chosen to be 55 μm, which has already been shown to be achievable using industrial printing technology [96]. Additionally, a 5-busbar design is assumed with an overall front side shading of 4%, which has recently been demonstrated for such a design [97]. At the rear side, a state-of-the-art rear surface passivation using, a stack of Al_2O_3 and SiN_x is further assumed. The rear side is then assumed to be full-area screen-printed with an aluminum paste. Line openings in the dielectric layer stack are assumed to be realized by laser ablation with a contact opening width of 100 μm [96]. A subsequent fast-firing step leads to the formation of a local back surface field. The general input parameters such as the spacing and the saturation current densities J_0 are summarized in Table 5.1. Realistic values for the J_0 values are chosen, which have been shown to be achievable in today's state-of-the-art screen-printed solar cells [98].

Figure 5.22 (a) shows the simulated conversion efficiencies η for a constant pitch p of the metal contact lines of 2 mm on the front and rear as a function of the doping concentration p_0, to compare the results here with previous results by Schmidt et al. [93]. In Figure 5.22 (b), an optimization of the front and rear side pitch in terms of the conversion efficiency has been performed for each simulated data point.

For the constant pitch of 2 mm at the front and rear [Fig. 5.22(a)], the Quokka simulation reveals that the optimum resistivity is shifted towards lower resistivities compared to the results shown in [93]. For the optimal resistivity of 0.75 Ω cm, a maximum efficiency of 21.9% is achieved. Compared to that, the optimal resistivity according to Ref. [93] was in the range between 1 and 2 Ω cm. The decrease of the efficiency towards both sides of the maximum efficiency is dominated by two different mechanisms. Towards

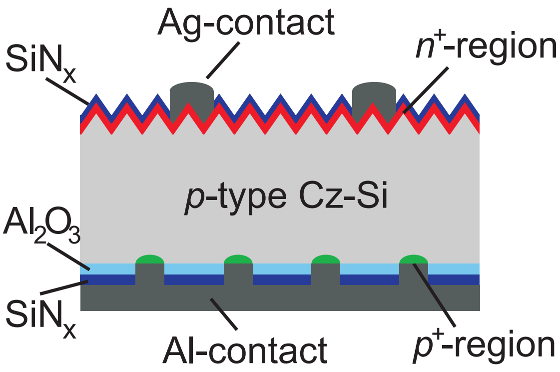

FIGURE 5.21: Schematic of the simulated passivated emitter and rear solar cell (PERC).

Table 5.1: Input parameters for the 2D Quokka simulations.

Parameter	Value
Cell thickness W [μm]	180
Series resistance $R_{s,finger}$ [mΩ cm^2] (only finger contribution)	100
Front side	
Front contact width p_{front} [μm]	55
n^+ sheet resistance ρ_{n^+} [$\Omega/\square$]	80
Junction depth x_{n^+} [μm]	0.62
Saturation current density of contacted area $J_{0,cont,n^+}$ [fA/cm^2]	500
Saturation current density of passivated area $J_{0,pass,n^+}$ [fA/cm^2]	125
Contact resistance R_{c,n^+} [mΩ cm^2]	2
Rear side	
Rear contact width p_{rear} [μm]	100
Sheet resistance beneath contact ρ_{p^+} $\Omega/\square$	35
Junction depth x_{p^+} [μm]	4
Contact resistance R_{c,p^+} [$m\Omega\, cm^2$]	8
Saturation current density on contacted area J_{0,met,p^+} [fA/cm^2]	650
Saturation current density of passivated area $J_{0,pass,rear}$ [fA/cm^2]	25

higher doping concentrations, that is, lower resistivities, the efficiency decreases because of a reduction of the bulk lifetime. Towards lower doping concentrations, that is, higher resistivities, the efficiency decreases because of lateral resistive losses of the majority carriers in the silicon bulk.

The latter limitation can be overcome by a reduction of the contact line distance on the rear side. This can be seen in Fig. 5.22 (b), where the contact distances on the front and rear side are varied independently to obtain the highest efficiency for each base resistivity. For the efficiency curves corresponding to the lifetimes after complete degradation (orange squares) and to the lifetimes after permanent recovery as presented in Ref. [93] (blue triangles), the maximum efficiency is shifted towards higher resistivities, greater than 4 Ω cm. For our novel lifetime parameterization (green circles), the pitch optimization does not shift the maximum efficiency significantly towards higher resistivities, but widens the range of resistivities with maximum efficiencies now reaching 22.1%, for a finger distance of 1.8 mm at the front and a line pitch of 1.2 mm at the cell rear, in this case. The simulation unambiguously reveals that if the contact line distances at the front and rear side are optimized, efficiencies of 22% can be reached for an extremely broad range of base resistivities between 0.5 and 3 Ω cm.

The fact that the green curve decreases towards lower resistivities is, again, an effect of the bulk lifetime. The parameterization of the lifetime after permanent deactivation according to Ref. [93] predicts a continuously increasing lifetime towards lower doping densities. Compared to that and according to Eq. 5.3, the lifetime parameterization presented in this study saturates at low doping densities at a lifetime of $\tau_1 = 5500\,\mu$s.

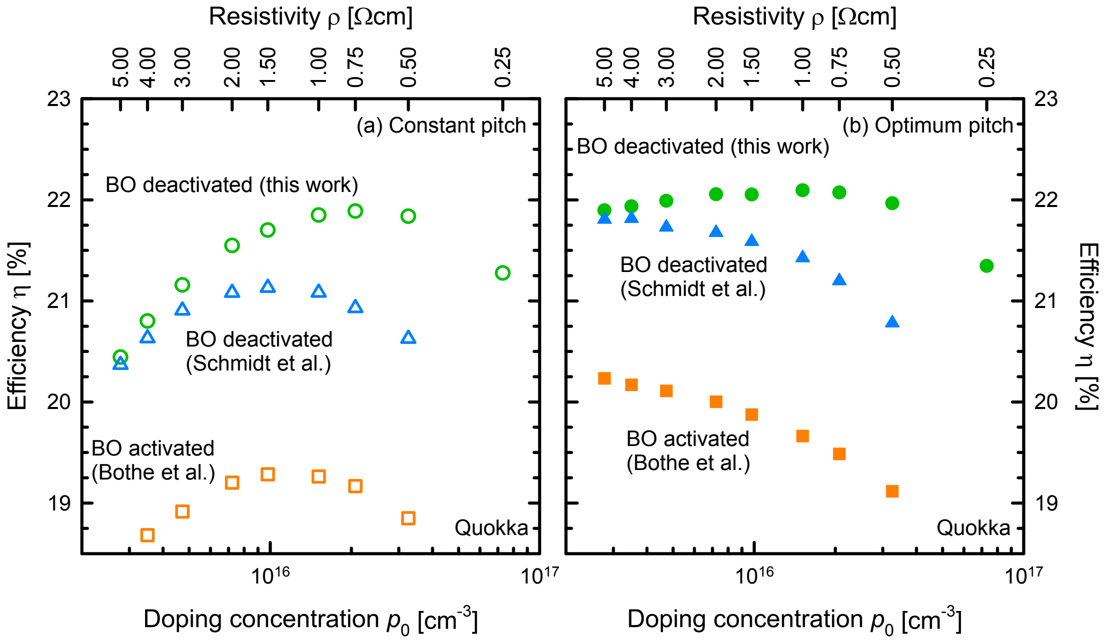

FIGURE 5.22: Simulated conversion efficiencies η versus base doping concentration p_0 (base resistivity ρ) using Quokka. (a) Efficiencies for the three different lifetime parameterizations, shown in Fig. 5.19, for a constant front and back pitch of 2 mm. (b) Efficiencies for the same lifetime parameterization with an optimum pitch at the front and rear side.

This leads to an intersection of the corresponding lifetime curves in Fig. 5.19 (solid green line and blue dashed line) at doping densities p_0 between $10^{15}\,\text{cm}^{-3}$ and $2 \times 10^{15}\,\text{cm}^{-3}$. Therefore, in Fig. 5.22(b), equal conversion efficiencies in this doping range for both parameterizations are obtained.

It is also interesting to take a closer look at the simulation results based on the completely degraded lifetimes shown in Fig. 5.22(b). Obviously, conversion efficiencies above 20% can be achieved even in the fully degraded state if lowly doped material with a specific resistivity above 2.0 Ω cm is used. Note, however, that in this case, the line distance has to be adapted, for example, at a bulk resistivity of 2.0 Ω cm, a rear pitch of only 0.6 mm (front finger spacing of 1.8 mm) leads to an efficiency of 20.0% in the fully degraded state.

For the maximal simulated efficiency of 22.1% on 1.0 Ω cm material, we perform a free energy loss analysis (FELA) [99]. The result of this analysis is shown in Fig. 5.23 for the eight parameters with the highest contributions to the lost power density P_{lost}. From this analysis, we conclude that the bulk lifetime according to our novel parameterization is not the limiting factor of the simulated conversion efficiency. The simulated efficiency is mainly limited by the saturation current densities at the front side at the passivated n^+-region $J_{0,pass,n^+}$ and at the metallized p^+-region on the rear side J_{0,met,p^+}, as well as by resistive losses in the n^+-region on the front side ρ_{n^+}. Hence, the lifetimes based

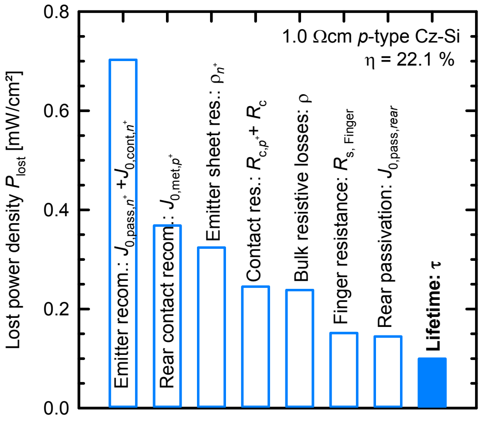

FIGURE 5.23: Lost power density P_{lost} according to the free energy loss analysis, performed for the highest obtained conversion efficiency of 22.1%. The eight parameters with the highest contributions to the lost power density are displayed.

on the novel parameterization would allow conversion efficiencies exceeding 23% if these parameters are further optimized.

To reduce the recombination currents at the front side even further, we introduce a selective emitter [105] to our simulation environment. Additionally, we significantly reduce the saturation current densities as well as the contact resistances at the front and rear side to values which are among the lowest reported for the respective structures. Table 5.2 summarizes the parameters which were adapted for the simulation of the optimized PERC cell. The overall shading at the front side is in this case reduced to 3.4% compare to 4% in the previous simulation. All other parameters remained unchanged. In Fig. 5.24 a schematic of our optimized PERC cell as well as the simulated conversion efficiency versus the base doping concentration are shown (purple squares). While the curve progression compared to our simulation of a PERC cell with a homogeneous emitter (green circles) remained equal, the maximum efficiency now reaches 23.4% for a

TABLE 5.2: Adapted input parameters for a 2D Quokka simulation of a next-generation PERC cell with selective emitter.

Parameter	Value
Front side	
n^+ sheet resistance ρ_{n^+} [$\Omega/\square$]	150 [100]
n^{++} sheet resistance $\rho_{n^{++}}$ [$\Omega/\square$]	30 [101]
Saturation current density of contacted area $J_{0,cont,n^{++}}$ [fA/cm^2]	210 [101]
Saturation current density of passivated area $J_{0,pass,n^+}$ [fA/cm^2]	22 [100]
Contact resistance R_c [mΩ cm^2]	1.3 [102]
Rear side	
Contact resistance R_{c,p^+} [$m\Omega\, cm^2$]	4 [103]
Saturation current density on contacted area J_{0,met,p^+} [fA/cm^2]	300 [104]
Saturation current density of passivated area $J_{0,pass,rear}$ [fA/cm^2]	8 [104]

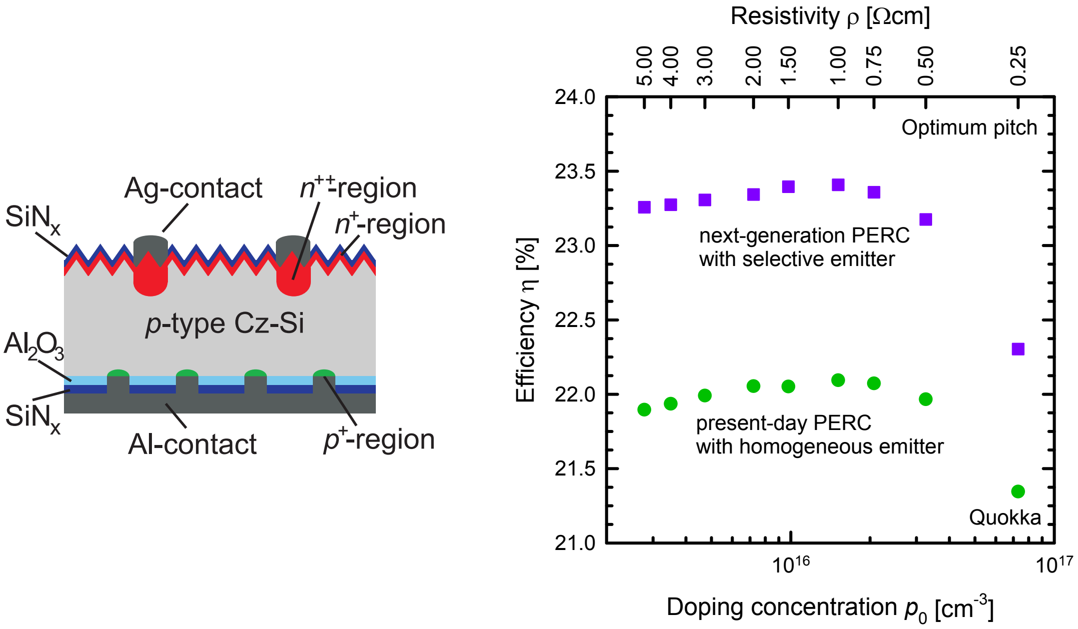

FIGURE 5.24: Left: Schematic of the simulated next-generation PERC cell with selective emitter. Right: Simulated conversion efficiencies η versus base doping concentration p_0 (base resistivity ρ) using Quokka of the next-generation PERC cell with selective emitter (purple squares) including our novel lifetime parameterization. As reference the efficiency curve obtained from the simulations of a present-day PERC cell with a homogeneous emitter is also shown (green circles, cf. Fig. 5.22).

base resistivity of 1.0 Ωcm. Furthermore, over a broad range of base resistivities between 0.5 and 5 Ωcm efficiencies above 23% can be achieved. Accordingly, PERC solar cells featuring a selective emitter can be expected to reach efficiency values above 23% in the future, if the high lifetime we observed on our lifetime samples can be transferred into the solar cell's bulk.

5.3.3 Summary

In the first part of this section, lifetimes of boron-doped Czochralski-grown silicon wafers after complete deactivation of the BO defect have been presented, which significantly exceeded the maximum lifetimes reported previously. For the first time we have achieved lifetimes of several milliseconds due to an optimized thermal treatment, which consisted of a fast-firing process and an optimized permanent BO deactivation. Based on our measured lifetime data, we have developed a new parameterization of the lifetime as a function of the hole concentration. In addition, we have modelled the injection dependence of the measured lifetimes after permanent recovery in the injection range relevant to solar cell applications using a single-level SRH centre at mid-gap with an electron-to-hole capture cross-section ratio of $\sigma_n/\sigma_p = 12$.

In the second part of this section, we have examined the impact of the new parameterization on the efficiency potential of present-day PERC solar cells by performing 2D simulations using Quokka. The simulations revealed that very high efficiencies up to 22.1% are achievable using today's state-of-the-art processing techniques, if the lifetimes achieved on our lifetime samples could be transferred into the device. Additionally, if the contact line spacing at the rear side of the PERC cells would be optimized with respect to the base resistivity of the wafer, a very broad range of wafer resistivities, between 0.5 and $3\,\Omega\,\mathrm{cm}$, has a potential for conversion efficiencies of 22%. Finally, our simulations of next-generation PERC cells with selective emitter revealed that a further optimization of the cell would allow to achieve even higher efficiencies in excess of 23% using conventional boron-doped Cz-Si material in the future.

5.4 Chapter summary

In the first part of this chapter, we have examined the impact of rapid thermal annealing (RTA) on the deactivation of the boron-oxygen-related defect centre. The result of this investigation is twofold. For the first time we could show that the exact parameters of the RTA treatment, namely the peak temperature and the belt speed, determine the lifetimes at different stages of degradation and recovery. The lifetimes τ_d after complete light-induced degradation, τ_0 after annealing in darkness as well as τ_{0p} after the permanent deactivation of the BO-related defect centre critically depend on the applied RTA treatment. Additionally, the kinetics of the deactivation process also depends on the RTA treatment. This is illustrated by the increasing recovery rate constant R_{de} with an increased sample cooling in a critical temperature regime around 600 °C. Importantly, we discovered a linear dependence of R_{de} on the cooling rate q at 600 °C. We interpreted our experimental results within the framework of a recent $\mathrm{B}_i\mathrm{B}_s\mathrm{O}_i$ model which consistently explains the dependence of the characteristic lifetimes on the complete cooling curve due to different participating complexes which are frozen-in at their individual critical temperatures. On the other hand, the recovery rate constant R_{de} depends linearly on the cooling rate at 600 °C as this is the critical temperature for the formation of boron nano-precipitates.

The kinetics of the recovery process was also shown to depend on the applied recovery conditions. For temperatures below $\vartheta = 220\,^\circ\mathrm{C}$ and illumination intensities below $P_{ill} = 100\,\mathrm{mW/cm}^2$ the rate constant R_{de} increases when increasing temperature and light intensity. The lifetime τ_{0p} reached after the recovery process, however, does not depend on the applied recovery conditions.

In the second part of this chapter we studied the impact of hydrogen introduced from the dielectric layers, usually applied for surface passivation, in a variety of experiments. Summarizing the results of these experiments, we could show for the first time that hydrogen is not responsible for the observed deactivation of the BO defect centre. An important finding in that regard is that samples processed at low temperature, passivated with PEDOT:PSS, which inhibits the diffusion of hydrogen into the bulk, nevertheless show a permanent recovery of the lifetime.

In the last part of this chapter, the achievable lifetimes after permanent recovery were examined. We achieved lifetimes which significantly exceeded lifetimes reached in previous studies, where no fast-firing process had been applied. For the first time we achieved lifetimes on conventional boron-doped Cz-Si material in the millisecond-range for base resistivities $\geq 1\,\Omega$cm. Based on our measured lifetime data, we developed a new parameterization which describes the lifetime after permanent recovery, depending on the hole concentration in darkness p_0 as well as on the injection density Δn. The lifetimes measured after permanent recovery were successfully described by a single-level SRH centre in the middle of the band gap with an electron-to-hole capture cross section of $\sigma_n/\sigma_p = 12$.
Additionally, we examined via 2D simulations the impact of our new parameterization on the performance of next-generation industrial PERC solar cells. Assuming today's state-of-the-art techniques, the lifetime in the silicon bulk is no longer the limiting factor for the conversion efficiency. Our simulations predict for the first time that conversion efficiencies exceeding 23% are achievable in next-generation industrial PERC cells on conventional boron-doped Cz-Si.

Chapter 6

Lifetime stability after deactivation of the boron-oxygen-related recombination centre

In this chapter, the stability of the lifetime of boron-doped Cz-Si at room temperature and at elevated temperatures after applying the process of permanent recovery is studied. In addition, we examine the impact of various parameters on the long-term stability, such as the cooling rate in the critical temperature regime (see section 5.1.2) and the recovery temperature at which the recovery process is conducted (see section 5.1.3). Furthermore, the influence of different types of surface passivation layers on the stability of the lifetime is explored. Finally, we present stability results obtained on solar cell level.

6.1 Long-term stability of the lifetime after BO deactivation

Lifetime samples are processed from commercially available Cz-Si which has a resistivity of $\rho = (1.02 \pm 0.03)\,\Omega\,\mathrm{cm}$ and an interstitial oxygen concentration of $[\mathrm{O}_i]$=$(6.9 \pm 0.3) \times 10^{17}\mathrm{cm}^{-3}$ determined via four-point-probe and FTIR measurements, respectively. Sample processing includes the removal of the surface damage using an aqueous solution of KOH and the cleaning of the surfaces by applying a standard RCA cleaning sequence. Subsequently, the samples undergo a phosphorus diffusion resulting in diffused n^+-regions on both surfaces with a nominal sheet resistance of $\rho_{sheet} = 100\,\Omega/\Box$.

Afterwards, the samples are separated into two different groups.

The *first group* keeps the diffused n^+-layers and is surface-passivated using a 70 nm thick silicon nitride (SiN_x) layer ($n_r = 2.05$), directly after the diffusion. The dielectric layer is deposited via plasma-enhanced chemical vapour deposition (PECVD).

In the *second group*, the diffused region is removed, again using KOH, and the surfaces are subsequently passivated by either an aluminium oxide/silicon nitride (Al_2O_3/SiN_x) stack or only with Al_2O_3 which is deposited via plasma-assisted atomic layer deposition (plasma-ALD). The thickness of the Al_2O_3 layer is chosen to be 5 and 10 nm for the passivation stack and 20 nm for the single-layer passivation. For the passivation stack the same SiN_x layer is deposited as in group 1.

After the sample preparation all samples undergo a rapid thermal annealing (RTA) treatment in a conventional belt-firing furnace (DO-FF-8.600–300, Centrotherm) applying a set peak temperature of 850 °C at various belt-speeds between 1.2 and 7.2 m/min. Lifetime measurements are performed using the lifetime tester WCT-120 from Sinton Instruments (see section 3.2.1). If not stated otherwise, the lifetime is extracted at an injection density of $\Delta n = 0.1 \times p_0$, with Δn being the excess carrier density and p_0 being the hole concentration in darkness. For the examined, non-compensated material the hole concentration equals the boron concentration.

The process of permanent recovery is performed at various temperatures between $\vartheta_{recov} = 150\,°C$ and $\vartheta_{recov} = 200\,°C$ on a hotplate, illuminated with a light intensity of $P_{ill} = 100\,mW/cm^2$ using a halogen lamp. To examine the stability of the recovered lifetime, the samples are subsequently illuminated at room-temperature ($\vartheta_{stab} \approx 25\,°C$) at a light intensity of $P_{ill,stab} = 10\,mW/cm^2$, also using a halogen lamp. Further stability tests are performed at an elevated temperature of $\vartheta_{stab} = 75\,°C$ and at an elevated light intensity of $P_{ill,stab} = 75\,mW/cm^2$.

6.1.1 Impact of the recovery temperature on the lifetime stability

One possibility to accelerate the process of permanent recovery is, independent of the previous temperature treatment, to perform the process at higher temperatures (see for example Ref. [106] and section 5.1.3). Hence, we examine here whether the process temperature ϑ_{recov} affects the stability of the lifetime reached after the permanent recovery. In Fig. 6.1, the stability of the lifetime after permanent recovery is shown for four different samples from group 2 passivated with an Al_2O_3/SiN_x passivation stack and recovered at four different temperatures between 150 °C and 200 °C. Over the course of approximately 1000 h, a weak degradation of the lifetime is observed, however, this degradation is completely different compared to the degradation behaviour of these samples prior to the permanent recovery treatment (see open squares in Fig. 6.1). A comparison to the

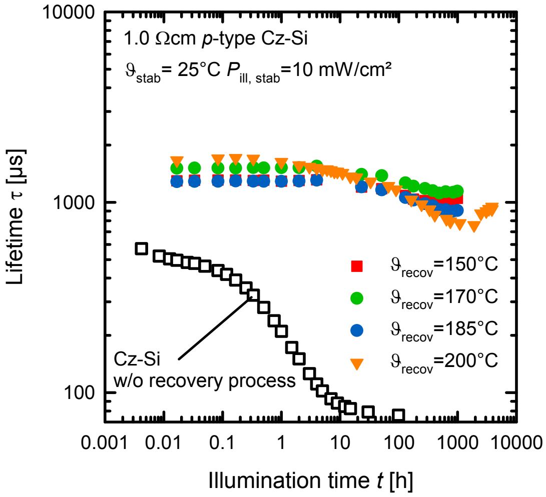

FIGURE 6.1: Effective lifetime τ versus illumination time t at room temperature after permanent recovery. The process of permanent recovery is performed at a light intensity of $100\,\mathrm{mW/cm^2}$ and at different temperatures between 150 °C and 200 °C. A weak degradation of the lifetime upon illumination at $10\,\mathrm{mW/cm^2}$ is observed which is, however, independent of the recovery temperature. The open squares correspond to the lifetime degradation without the recovery process being performed.

lifetime behaviour of identically processed float-zone (FZ) lifetime samples reveals that the observed degradation is a bulk material effect and not due to the degradation of the surface passivation quality.

The observed degradation differs in two different ways from the traditional LID: First, the degradation proceeds on a much longer time scale. The traditional BO-related LID process on the investigated material features a degradation rate constant of $R_{gen} = 0.47\,\mathrm{h^{-1}}$ [28] at room temperature. The observed degradation, however, corresponds to a degradation rate constant of only $\gamma = (0.006 \pm 0.002)\,\mathrm{h^{-1}}$.

Second, the magnitude of degradation is much smaller than typically observed for the standard LID effect. Before the process of permanent recovery, the average lifetime after complete LID τ_d on these samples is determined to $\tau_d = (97 \pm 12)\,\mu\mathrm{s}$. However, after almost 1000 h of illumination at room temperature after the process of permanent recovery, the average lifetime of these samples is still $\tau = (950 \pm 150)\,\mu\mathrm{s}$.

Although the recovered lifetime is fairly stable, there seems to be a weak impact of the recovery temperature, with a slight increase in degradation after 1000 h with increasing ϑ_{recov}. However, this effect lies within the experimental scatter. Another interesting observation is that for some samples, the lifetimes seem to increase again for very long illumination times (see orange triangles in Fig. 6.1).

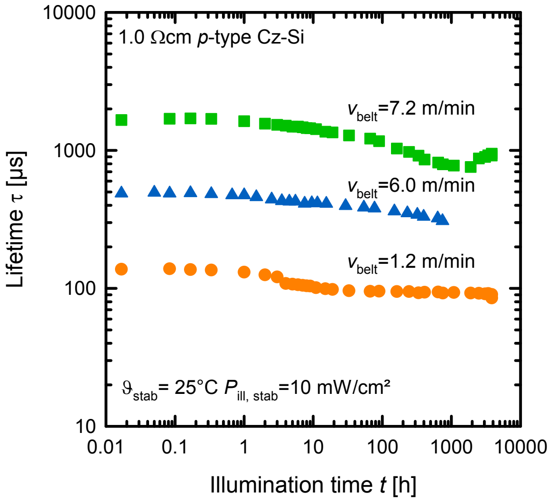

FIGURE 6.2: Effective lifetime τ versus illumination time t at room temperature for three differently treated samples during RTA. A constant set peak temperature of 850 °C is applied to all samples, however, the belt speed during RTA is varied between 1.2 m/min (circles) and 7.2 m/min (squares). All samples are permanently recovered at 200 °C and 100 mW/cm^2 light intensity.

6.1.2 Impact of the RTA treatment on the lifetime stability

In section 5.1.2 it was shown that an RTA treatment can be very beneficial to accelerate the process of permanent recovery. In the following, we examine the stability of the lifetime after the recovery process for different RTA treatments. In Fig. 6.2, the measured effective lifetime versus the illumination time at room temperature with a light intensity of $P_{ill,stab} = 10\,\mathrm{mW/cm^2}$ is shown for three samples, treated differently during the RTA process. A set peak temperature during RTA of $\vartheta_{Peak} = 850\,°\mathrm{C}$ is applied to all samples. The belt speed, on the other hand, varies between $v_{belt} = 1.2\,\mathrm{m/min}$ and $v_{belt} = 7.2\,\mathrm{m/min}$. The investigated samples are all taken from group 2, passivated with an $\mathrm{Al_2O_3/SiN}_x$ stack and recovered at a recovery temperature of $\vartheta_{recov} = 200\,°\mathrm{C}$. For all different samples a comparable degradation of the lifetime after the permanent recovery process is observed, suggesting that the degradation after recovery is independent of the exact RTA conditions.

6.1.3 Lifetime stability at elevated temperatures

Under solar cell operating conditions in a module, the solar cell is exposed to light at elevated temperatures. To test the stability of the lifetime under these conditions, we expose lifetime samples to illumination at a temperature of $\vartheta_{stab} = 75\,°\mathrm{C}$. Concerning the degradation due to the BO defect it is known that the defect generation rate constant is independent of the light intensity for light intensities higher than $P_{ill,stab} = 1\,\mathrm{mW/cm^2}$

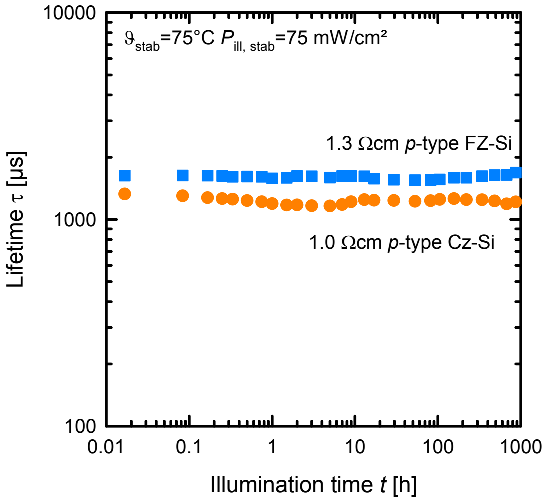

FIGURE 6.3: Effective lifetime τ versus illumination t time at an elevated temperature of 75 °C and at an elevated light intensity of 75 mW/cm^2. No dependence of the lifetime on the illumination time can be observed on both, a FZ-Si reference sample (squares) and the Cz-Si sample under investigation (circles). Both samples are permanently recovered at 185 °C and 100 mW/cm^2 light intensity.

[24]. For the degradation effect which we observed after applying the permanent recovery process the dependence on the light intensity is yet unknown. However, as solar cells preferably operate at higher light intensities ($P_{ill} > 1\,\mathrm{mW/cm^2}$), an increased light intensity of $P_{ill,stab} = 75\,\mathrm{mW/cm^2}$ is chosen. The samples have all been taken from group 2, passivated with an Al_2O_3/SiN_x passivation stack and permanently recovered at $\vartheta_{recov} = 185\,°\mathrm{C}$. In Fig. 6.3, an example of the stability of the lifetime at elevated temperatures is shown. A 1.3 Ω cm FZ silicon lifetime sample, treated identically, is included as reference. Within the first 900 h of illumination no change of the lifetime in observed in both the Cz-Si and the FZ-Si samples, suggesting that the degradation we observed in Fig. 6.1 is not accelerated by increasing temperature and illumination intensity.

6.1.4 Impact of the surface passivation on the lifetime stability

In section 5.2 we showed that the process of permanent recovery does not rely on hydrogen being incorporated from surface passivating dielectric layers into the silicon bulk. In this section, we analyse if the surface passivation layer, and thus the hydrogen concentration in this layer, does have an influence on the stability of the lifetime τ_{0p} after the recovery process. An experiment is performed which analyses the influence of different surface passivation layers providing different amounts of hydrogen. Samples from group 1 and 2 with an Al_2O_3/SiN_x passivation stack and with a single Al_2O_3 layer are chosen. The total hydrogen concentration [H] in the Al_2O_3 and in the SiN_x layers differ roughly

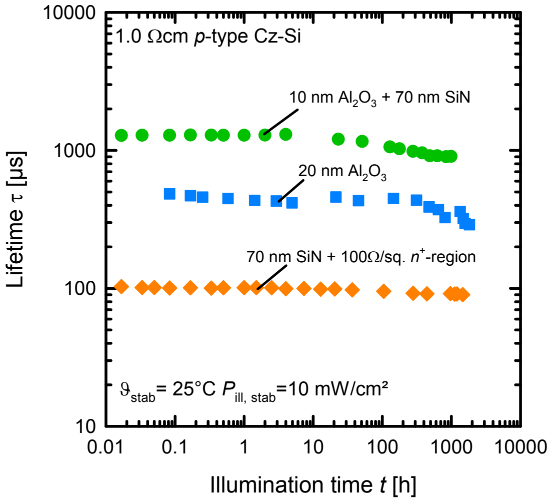

FIGURE 6.4: Effective lifetime τ versus illumination time t at room temperature for three differently passivated lifetime samples. Apart from the surface passivation all samples have been treated identically. Circles correspond to an Al_2O_3/SiN_x passivation stack, squares to a single-layer Al_2O_3 passivation and diamonds to a SiN_x passivation with n^+-region beneath.

by a factor of 10, with [H](Al_2O_3)≈ 1 to 2 at. % [86] and [H](SiN_x)≈ 15 to 20 at. % [107]. After the permanent recovery at $\vartheta_{recov} = 185\,°C$ we expose the samples to illumination with a light intensity of $P_{ill,stab} = 10\,mW/cm^2$ at room temperature. The results of this experiment are shown in Fig. 6.4 for three different samples which have been treated at 850 °C set peak temperature and 7.2 m/min belt speed during RTA.

For samples with different surface passivation layers, treated otherwise identically, a comparable degradation of the lifetime after the process of permanent recovery is observed. Especially, when comparing the results for the sample with the Al_2O_3/SiN passivation stack and the result for the sample with a single Al_2O_3 layer, it can be concluded that the amount of hydrogen being present in the dielectric layer does not have a major impact on the stability of the lifetime.

On the other hand, comparing the samples with the passivation stack and the single Al_2O_3 layer, the absolute values of the lifetimes are higher, by approximately a factor of two, for the passivation layers with more hydrogen. In case of the passivated diffused region, the lifetime is mostly dominated by the recombination at the n^+-diffused surfaces.

6.1.5 Impact of material in the lifetime stability

In the first sections of this chapter, the impact of external influences, namely the recovery temperature, the RTA treatment, the surface passivation type and the exposure to room and elevated temperatures, was studied on a single Cz-Si material. In order to

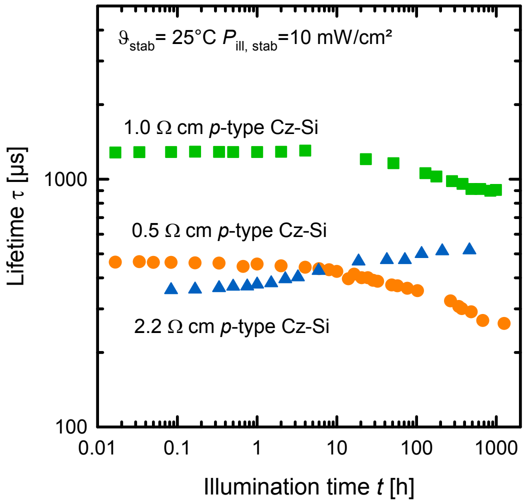

FIGURE 6.5: Effective lifetime τ versus illumination time t at room temperature for three samples with different base resistivities. Besides the different staring materials, the lifetime samples are treated identically.

examine the validity of these findings on different Cz-Si materials, we process lifetime samples on different Cz-Si materials following the process of group 2. For the RTA process the parameters have been set at 850 °C peak temperature and a belt speed of $v_{belt} = 7.2\,\mathrm{m/min}$. Materials with a base resistivity of $\rho = 2.2\,\Omega\,\mathrm{cm}$ and $\rho = 0.5\,\Omega\,\mathrm{cm}$ are chosen. After sample processing and subsequent permanent recovery of the lifetime at 185 °C at a light intensity of $P_{ill,recov} = 100\,\mathrm{mW/cm^2}$, the samples are exposed to prolonged illumination at room temperature at a light intensity of $P_{ill,stab} = 10\,\mathrm{mW/cm^2}$. In Fig. 6.5, the result of this experiment is shown for three lifetime samples. While the Cz-Si samples with the base resistivites $\rho = 1.0\,\Omega\,\mathrm{cm}$ and $\rho = 0.5\,\Omega\,\mathrm{cm}$ feature a slightly degrading lifetime over the same time scale, the lifetime sample with the base resistivity of $\rho = 2.2\,\Omega\,\mathrm{cm}$ shows a continuously increasing lifetime, however, on a relatively low lifetime level. For comparison, in section 5.3, lifetimes above $\tau = 2\,\mathrm{ms}$ were obtained for materials in this resistivity range. This result shows that the stability, or the lifetime behaviour after permanent recovery, critically depends on the Cz-Si material itself. We attribute the differences in the long-term stability to different background defects which are expected to be present in the different Czochralski-grown materials and limit the lifetime to values usually lower than the lifetime of defect-lean float-zone silicon. Although the detailed nature of these defects is so far unknown, it is very likely that they are not related to the BO defect which causes the typical light-induced degradation in boron-doped Cz-Si, as for example no clear trend depending on the boron (or hole) concentration can be observed, as can be seen in Fig. 6.6.

Figure 6.6 shows the result of an experiment, which has been jointly conducted with centrotherm photovoltaics AG using their commercially available belt-line regeneration

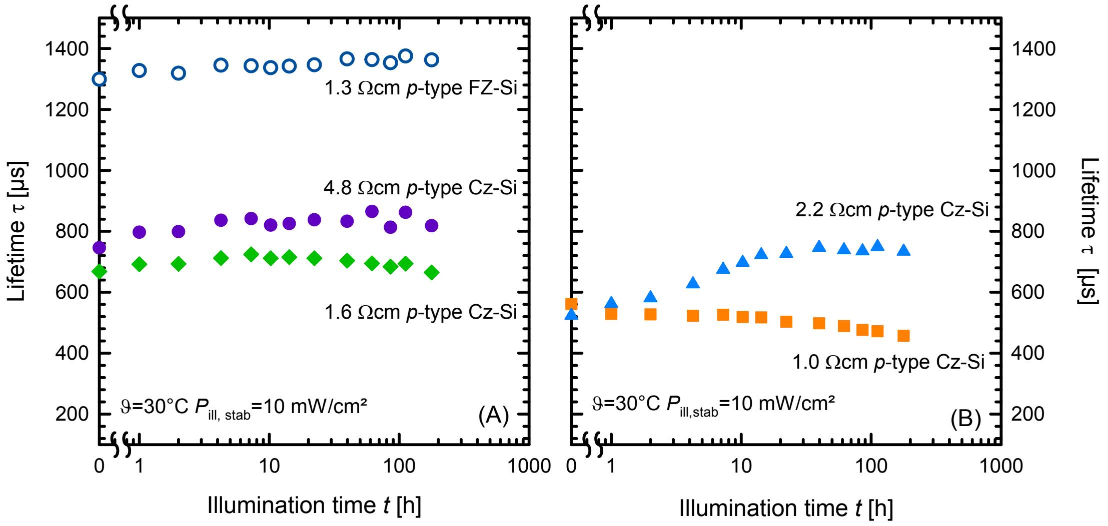

FIGURE 6.6: Effective lifetime τ plotted versus the illumination time t at room temperature and $P_{ill,stab} = 10\,\mathrm{mW/cm^2}$ light intensity for five Cz-Si materials. Left (A) two examples of Cz-Si materials featuring a stable lifetime after regeneration are shown, right (B) two examples of Cz-Si materials with changing lifetimes are shown. The FZ reference sample (A) features a stable lifetime.

furnace (C.REG 6.200), especially designed for the deactivation of the boron-oxygen defect centre on an industrial scale. While the processing to lifetime samples has been performed at ISFH according to the processing sequence of group 2 applying the same conditions for the RTA treatment as mentioned above ($\vartheta_{Peak} = 850\,^\circ\mathrm{C}$, $v_{belt} = 7.2\,\mathrm{m/min}$), the recovery of the lifetime has been performed using the belt-line furnace at at centrotherm. In total four different Cz-Si materials with base resistivities between $\rho = 1.0\,\Omega\,\mathrm{cm}$ and $\rho = 4.8\,\Omega\,\mathrm{cm}$ have been investigated. Again it is observed that different materials behave differently under the same conditions after the recovery process. While stable lifetimes are observed for the $4.8\,\Omega\,\mathrm{cm}$ and the $1.6\,\Omega\,\mathrm{cm}$ material (see Fig. 6.6(A)) the lifetime of the $1.0\,\Omega\,\mathrm{cm}$ material slightly degrades and the lifetime of the $2.2\,\Omega\,\mathrm{cm}$ material even increases.

6.2 Long-term stability of solar cells after BO deactivation

We present our results on solar cell level from two different perspectives. In the first part, a one-dimensional device simulation of a silicon solar cell is performed which includes the lifetime changes observed in the previous section. In the second part, we examine actual PERC solar cells.

Table 6.1: Input parameters for the 1D PC1D simulations.

Parameter	Value
Cell thickness W [μm]	180
Base resistivity ρ [$\Omega\,$cm]	1
Emitter	
Emitter contact resistivity $\rho_{Emitter}$ [$\Omega\,$cm^2]	0.4
Emitter sheet resistance ρ_{sheet} [$\Omega/\square$]	80
(error function profile)	
Peak concentration [cm^{-3}]	10^{20}
Junction depth x_j [μm]	0.16
Surface	
Recombination velocity at the front S_{front} [cm/s]	16000
Recombination velocity at the rear S_{rear} [cm/s]	70

6.2.1 One-dimensional device simulations of the solar cell stability

In order to estimate the impact of the lifetime degradation observed in the previous sections on the performance of high-efficiency silicon solar cells, we perform one-dimensional device simulations using the PC1D simulation tool [108]. A next-generation industrial-type solar cell using a passivated emitter and rear cell (PERC) design [105] is simulated. The general input parameters of the simulation are listed in Tab. 6.1. For the simulation, the optical properties of the cell presented in Ref. [97] are adopted. For the lifetime in the silicon bulk material, it is assumed that the lifetime degrades as shown in Fig. 6.1 for the sample permanently recovered at a recovery temperature of $\vartheta_{recov} = 185\,°$C. To implement the change of the lifetime into the simulation, the injection-dependent lifetime measured after defined illumination times is analysed and the lifetime curves are fitted according to Shockley-Read-Hall theory [61, 62]. The determined values for the capture time constants for electrons τ_{n0} and holes τ_{p0}, as well as the energy level E_t are then included in the PC1D device simulation. An example of an injection-dependent lifetime curve measured after 988 h of illumination at room-temperature is shown in Fig. 6.7. For comparison, the injection-dependent lifetime measured on the same sample after 1 min of illumination as well as the intrinsic lifetime limit are also displayed.

The result of the PC1D simulation is shown in Fig. 6.8. As can be seen from Fig. 6.8, the reduction in the lifetime during illumination at room temperature, in this case from $\tau = 1500\,\mu$s to $\tau = 900\,\mu$s over the period of 988 h, does not lead to a change in the conversion efficiency of $\eta = 21.2\,\%$ and only to a marginal degradation in the open-circuit voltage of $\Delta V_{oc} < 1\,$mV . Compared to that, the efficiency and open-circuit voltage in the fully degraded state are $\eta = 20.5\,\%$ and $V_{oc} = 649\,$mV ($V_{oc} = 662\,$mV after permanent recovery), respectively.

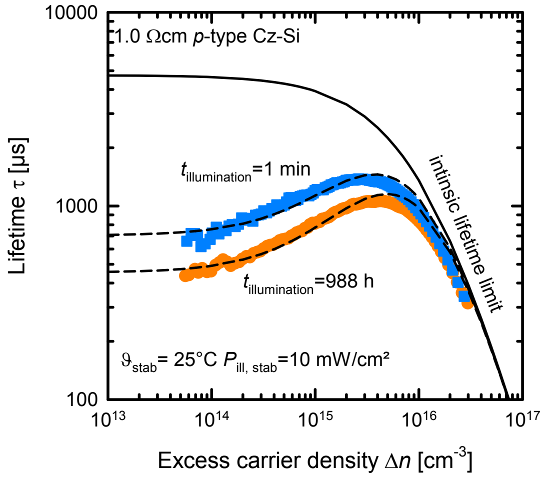

FIGURE 6.7: Injection-dependent effective lifetime τ measured after 1 min of illumination at room-temperature (blue squares) and after 988 h (orange circles) of illumination on the same lifetime sample. The time characteristic of the degradation of this sample is shown in Fig. 6.1 for the sample recovered at $\vartheta_{recov} = 185\,°\text{C}$. The intrinsic lifetime limit according to Richter et al. [60] is also displayed. The black dashed lines are calculated using the SRH equation and assuming a single-level recombination centre at mid-gap, including the intrinsic lifetime limit.

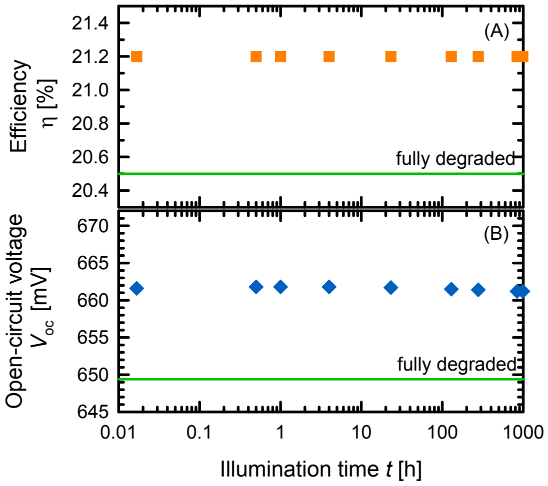

FIGURE 6.8: Simulation result of a PC1D simulation of an industrial-type PERC solar cell in terms of the conversion efficiency η (A) and the open-circuit voltage V_{oc} (b) versus the illumination time t. The implemented lifetime values are extracted from Fig. 6.1.

Hence, it can be concluded that on solar cell level our process of permanent recovery, leads to a stable solar cell performance for at least 1000 h under illumination at room temperature (25°C) as well as at elevated temperatures (75°C).

6.2.2 Experimental results on solar cell level

In this section, we examine PERC solar cells after permanent deactivation of the BO defect. As base material $1.0\,\Omega\,\mathrm{cm}$ Cz-Si is used. The cells are processed at a size of $239\,\mathrm{cm}^2$. Processing includes the removal of the surface damage as well as wafer cleaning. Afterwards, a rear side protection layer is deposited followed by an alkaline texturing. The emitter is then formed in a phosphorus diffusion. The diffused region features a sheet resistance of $\rho_{sheet} = 80\,\Omega/\square$. After the diffusion process, the rear protection layer as well as the phosphosilicate glass are removed before the surfaces are passivated using an aluminium oxide (Al_2O_3) / silicon nitride (SiN_x) stack at the rear side and a silicon nitride anti-reflection coating at the front side. Next, the laser contact openings are formed on the rear side using a pico-second laser. The front side metallization is then realized by a fine-line silver printing technique while the rear metallization is realized using a full-area printed aluminium paste. At last, the solar cells are fired for contact formation. More details about the processing sequence can be found in Ref. [98].

The solar cells are characterized using the pv-tools LOANA system under standard testing conditions, i.e. under $100\,\mathrm{mW/cm}^2$ light intensity at a temperature of 25 °C. Figure 6.9 shows the changes of the parameters of the IV-characteristics of the solar cell during the recovery process at an illumination intensity of $P_{ill} = 100\,\mathrm{mW/cm}^2$ and a recovery temperature of $\vartheta_{recov} = 185\,^\circ\mathrm{C}$. The orange squares in Fig. 6.9 correspond to the values in the fully activated state of the boron-oxygen complex which is reached upon illuminating the cell at room temperature for more than 24 h. The green squares are the values measured directly after an annealing step at 200 °C for 10 min in darkness, which corresponds to an inactive state of the BO complex. Directly after the latter measurement, the solar cell is exposed to the recovery conditions. Hence, a fast degradation of the open-circuit voltage V_{oc} (Fig. 6.9 (A)) and the short-circuit current density J_{sc} (Fig. 6.9 (B)) is observed which is followed by a recovery of these values. The fill factor FF (Fig. 6.9 (C)), on the other hand, does not change throughout the process. Accordingly, the conversion efficiency η (Fig. 6.9 (D)) follows the changes of V_{oc} and J_{sc}. The strongest influence of the recovery process can be observed for the V_{oc} values. In the fully degraded state we measure an open-circuit voltage of $V_{oc} = 644.5\,\mathrm{mV}$ which is strongly increases by 2% to $V_{oc} = 658.1\,\mathrm{mV}$ after annealing in darkness. After completing the recovery process, a slightly higher value of $V_{oc} = 659.3\,\mathrm{mV}$ is measured. J_{sc} changes form $J_{sc} = 38.0\,\mathrm{mA/cm}^2$ prior to the recovery process to $J_{sc} = 38.8\,\mathrm{mA/cm}^2$, which is also an increase of 2% relative. With the unchanged average fill factor of FF = 80.0%, this translates into an increase of the conversion efficiency from $\eta = 19.6\%$ in the fully degraded state to a maximum efficiency of $\eta = 20.5\%$ after recovery, which corresponds to a relative increase of 4.5%.

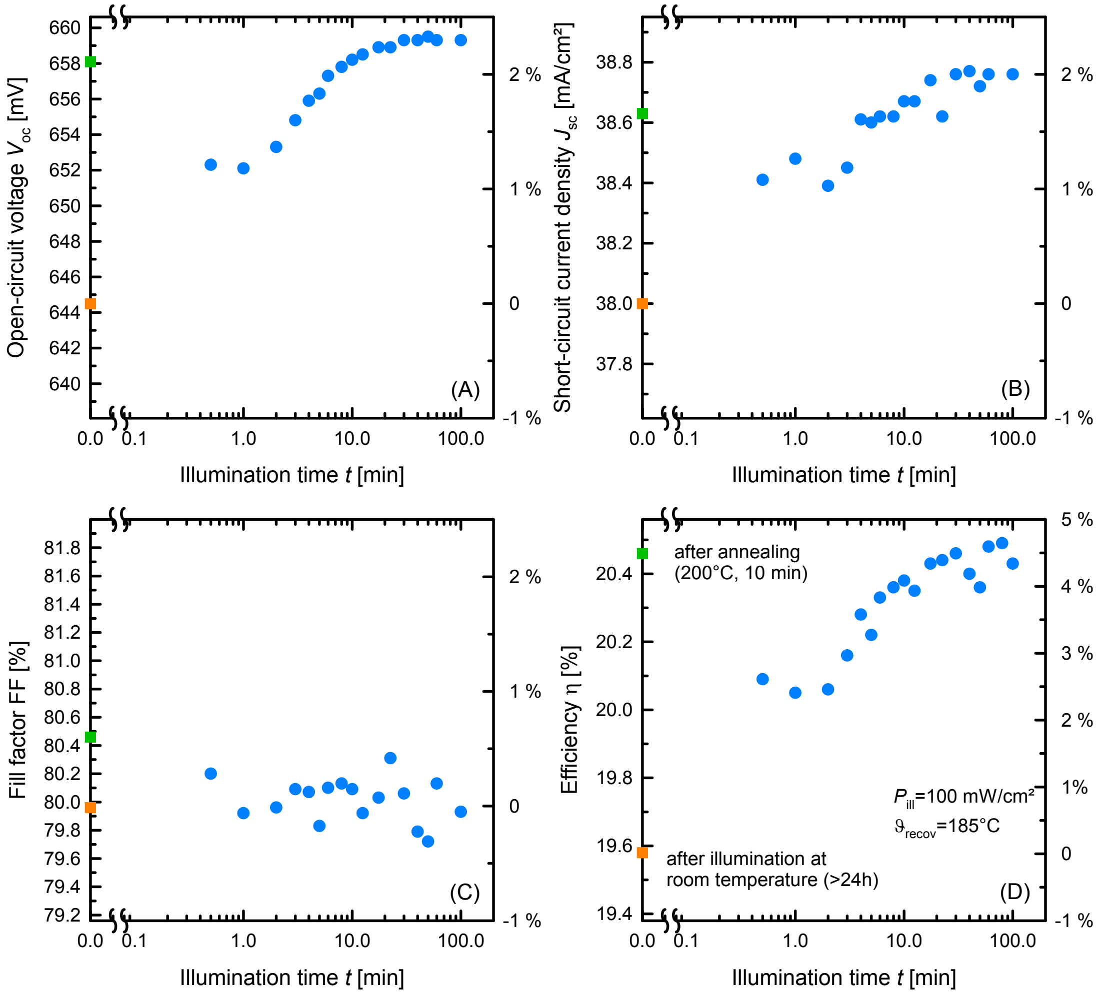

FIGURE 6.9: Permanent recovery of a PERC solar cell at an illumination intensity of $P_{ill} = 100\,\mathrm{mW/cm^2}$ and a recovery temperature of $\vartheta_{recov} = 185\,°\mathrm{C}$. The change during the recovery process of the open-circuit voltage V_{oc} (A), of the short-circuit current density J_{sc} (B), of the fill factor FF (C) and of the conversion efficiency η (D) is displayed. Relative changes, referenced to the values in the fully activated state of the BO complex, are given on the right y-axis.

The changes of V_{oc} and J_{sc} are mainly driven by the changes of the free carrier lifetime in the bulk material [3] which can be easily understood for V_{oc}. The V_{oc} of an ideal solar cell is given by [109]:

$$V_{oc} = \frac{k_b T}{q_e} ln \left[\frac{(N_A + \Delta n)\Delta n}{n_i^2} \right], \tag{6.1}$$

with T being the absolute temperature, k_b the Boltzmann constant, q_e the elementary charge, $N_A = p_0$ the doping density, Δn the excess charge carrier density and n_i the intrinsic carrier concentration. According to Eqn. 3.2, a higher lifetime corresponds to a lower recombination rate and hence a higher carrier density Δn at a constant illumination intensity. Accordingly, V_{oc} increases with increasing lifetime. Also J_{sc} is a monotone function of τ, hence an increasing lifetime causes an increasing short-circuit current.

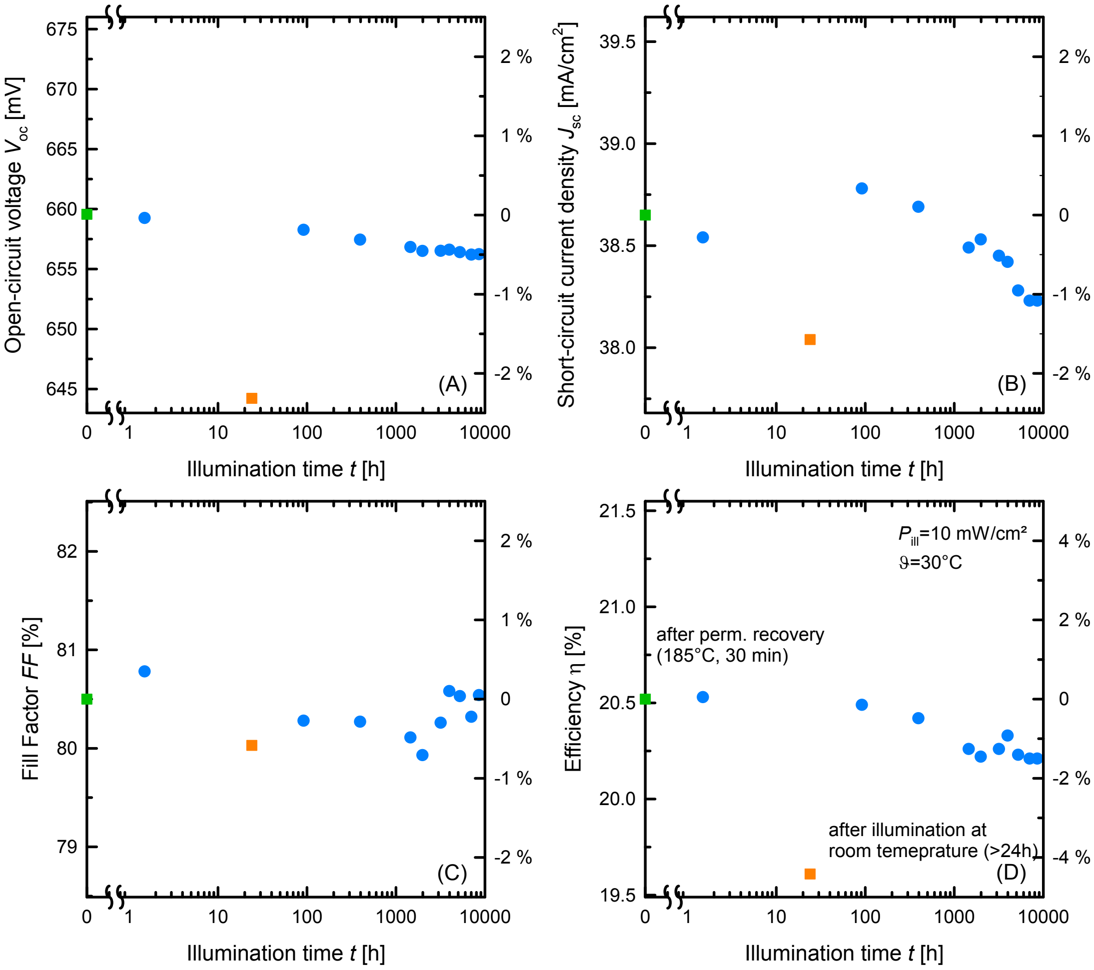

FIGURE 6.10: Stability of a permanently recovered PERC solar cell tested at an illumination intensity of $P_{ill} = 10\,\mathrm{mW/cm^2}$ at room temperature. The changes of the open-circuit voltage V_{oc} (A), of the short-circuit current density J_{sc} (B), of the fill factor FF (C) and of the conversion efficiency η (D) is displayed. Relative changes, referenced to the values measured directly after the recovery process, are given on the right y-axis.

Figure 6.10 shows the stability of a different PERC solar cell from the same batch, recovered at $\vartheta_{recov} = 185\,°\mathrm{C}$ and a light intensity $P_{ill} = 100\,\mathrm{mW/cm^2}$ for 30 min. The stability is tested at room temperature and an illumination intensity of $P_{ill} = 10\,\mathrm{mW/cm^2}$ for up to 10000 h, corresponding to more than 415 days. As can be seen in Fig. 6.10 (D), the conversion efficiency η of the cell under investigation is reduced over the testing period by 1.5% relative, from 20.5 % to saturation value of 20.2 %, which is much lower than the reduction of more than 4% over the course of 24 h without applying the recovery process (see orange square in Fig. 6.10 (D)). The reduction of η is mainly caused by a reduction in J_{sc} of 1% from $J_{sc} = 38.65\,\mathrm{mA/cm^2}$ directly after recovery to $J_{sc} = 38.23\,\mathrm{mA/cm^2}$. Compared to the J_{sc}, V_{oc} decreases only from $V_{oc} = 659.6\,\mathrm{mV}$ to $V_{oc} = 656.2\,\mathrm{mV}$, which corresponds to a reduction of only 0.5%.

As observed previously, the fill factor is not affected. Comparing this experimental result

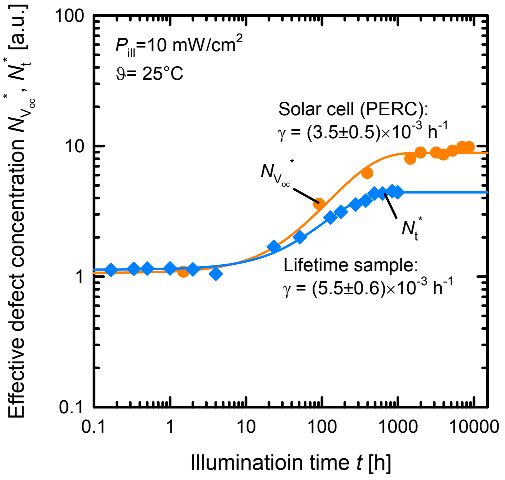

FIGURE 6.11: Effective defect concentrations $N^*_{V_{oc}}$ and N^*_t versus the illumination time t at room temperature after the recovery process, calculated from the change of the open-circuit voltage V_{oc} of a PERC cell shown in Fig. 6.10 (A) (orange circles) and from the change of the lifetime τ of a lifetime sample shown in Fig. 6.1. The cell as well as the lifetime samples are recovered at $\vartheta_{recov} = 185\,°\mathrm{C}$ at a light intensity of $P_{ill} = 100\,\mathrm{mW/cm^2}$. N^*_t is independently scaled.

to the results based on the simulation in the previous section, it is obvious that the solar cell under investigation degrades much stronger upon illumination at room temperature compared to the prediction of the simulation. However, the degradation proceeds over the same time frame as is shown in Fig. 6.11. While the effective defect concentration corresponding to the lifetime sample is calculated using to Eqn. 2.1 and replacing τ_0 with τ_{0p}, the defect concentration corresponding to the solar cell is calculated according to Bothe [65] using the expression

$$N^*_{V_{oc}}(t) = \frac{1}{\exp(q_e V_{oc}(t)/(n_l k_b T))} - \frac{1}{\exp(q_e V_{oc}(t=0)/(n_l k_b T))}. \tag{6.2}$$

Here, q_e is the elementary charge, k_b the Boltzmann constant, T the absolute temperature and n_l the local ideality factor. The latter is considered to be unity in the investigated case [110]. The change in the effective defect concentration can be fitted using a simple exponential function, as is shown by the solid coloured lines in Fig. 6.11, from which the degradation rate constant γ can be extracted. For these two examples, the rate constant $\gamma = (3.5 \pm 0.5) \times 10^{-3}\,\mathrm{h}^{-1}$ is extracted for the solar cell and $\gamma = (5.5 \pm 0.6) \times 10^{-3}\,\mathrm{h}^{-1}$ is extracted for the lifetime sample, which is very similar. Thus, the observed degradation of the solar cell is predominantly driven by the change of the bulk lifetime. Please note, that the degradation rate constant of the lifetime sample without the recovery process is $R_{gen} = 0.47\,\mathrm{h}^{-1}$, i.e. two orders of magnitude larger.

Also, the more pronounced degradation of the solar cell compared to the lifetime sample can be understood considering the results shown in Fig. 6.2 and the fact that the solar cell is not fired at the maximum belt speed. Hence, it is a reasonable assumption that the lifetime in the bulk of the solar cell is lower than the maximum lifetime shown in Fig. 6.2 which might explain the more pronounced degradation of the examined solar cell compared to the simulation, where the maximum lifetime was assumed.

6.3 Chapter summary

In this chapter, the stability of the lifetime upon further illumination of boron-doped, Cz-Si material was examined after applying the permanent recovery process. The stability was investigated at room temperature as well as at elevated temperatures, typical for solar cell operating conditions. Additionally, one-dimensional device simulations of a PERC solar cell implementing the measured injection-dependent lifetimes during the stability tests were performed.

The lifetime measurements showed a minor degradation of the lifetime during illumination at room temperature and a light intensity of $P_{ill,stab} = 10\,\mathrm{mW/cm^2}$. However, for the first time we observed lifetimes higher than 1 ms after an illumination period of approximately 1000 h on the examined $1\,\Omega\,\mathrm{cm}$ Cz-Si material. The observed degradation was found to be independent of the applied recovery temperature, independent of the belt speed at a fixed set peak temperature of $\vartheta_{Peak} = 850\,^{\circ}\mathrm{C}$ during the applied rapid thermal annealing step, as well as independent of the passivation layer deposited on the samples' surfaces.
For lifetime samples exposed to an elevated temperature (75 °C) and an elevated light-intensity $P_{ill,stab} = 75\,\mathrm{mW/cm^2}$ after the process of permanent recovery, no degradation within the first 900 h of illumination was observed. An investigation of the lifetime stability of different Cz-Si materials revealed a material-specific behaviour of the lifetime after the recovery process upon illumination at room temperature. In particular, a stable, an increasing as well as a decreasing lifetime were observed, depending on different background defects in different materials, which dominate the lifetime after permanent deactivation of the BO defect. Because of the different lifetime evolutions we consider it as very unlikely that these unknown background defects are related to the BO defect, which causes the well-known LID effect.

In the second part, the observed degradation of the lifetime was analysed in detail and the lifetime values were implemented into a PC1D simulation of a next-generation industrial-type PERC solar cell. The simulation suggests that the lifetime degradation does not affect the characteristic solar cell parameters and illumination-stable solar cell efficiencies in excess of 21 % are achievable on conventional Cz-grown boron-doped silicon. Additionally, the stability of a PERC solar cell was tested experimentally after permanent recovery. The conversion efficiency of the investigated solar cell degraded by 1.5% relative over the course of 10000 h (more than 415 days) from 20.5% to 20.2%. Despite this degradation, the saturated efficiency of 20.2% was considerably higher than the efficiency after complete degradation without the recovery process of 19.6%. From the observed weak degradation we concluded that the lifetime in the bulk of the solar cell is lower than the optimum lifetimes considered in our simulations. This reduced lifetime was attributed to the non-optimal firing conditions of the solar cell with regard to the bulk lifetime. Nevertheless, the degradation rate constant of the lifetime samples and the solar cell were identical within the uncertainty of our analysis, which clearly indicates that the degradation of the efficiency of the PERC cell is predominantly driven by the reduction of the bulk lifetime.

Comparing the post-recovery degradation to the well known BO-related degradation, it has to be pointed out that the degradation rate constant in this case is two orders of magnitude lower than the rate constant of BO-related degradation. Additionally, the magnitude of the degradation observed in this chapter was much lower than the degradation caused by the BO complex. Hence, we conclude that the degradation observed in this chapter is not related to the boron-oxygen defect, but is due to a hitherto undiscovered background defect, observed for the first time in this thesis.

Chapter 7

Summary and outlook

In this work boron-doped, oxygen-rich Czochralski-grown silicon was studied with regard to the bulk material quality characterized by the recombination lifetime of excess carriers. Our focus was to improve the fundamental understanding of lifetime degradation and regeneration related to the activation and deactivation of a defect complex which is formed in the silicon material in the simultaneous presence of boron and oxygen. The responsible defect complex, referred to as BO defect, becomes recombination-active under carrier injection, typically realized via illumination, at room temperature. However, illumination at elevated temperatures reduces the recombination activity of the defect in a process which is referred to as permanent deactivation. In this thesis, both the activation of the BO defect as well as its permanent deactivation (permanent recovery of the lifetime) were studied in detail.

The impact of the crystal growth conditions on the BO defect formation was studied on three different Czochralski-grown silicon crystals. Along the crystal axis, apart from the influence of the variations in the doping and oxygen concentrations, no relevant impact of the position on the BO defect formation was observed. On a silicon crystal where a transition between a vacancy-rich and interstitial-rich region occurred, we were able to shown for the first time that typical growth-related concentrations of vacancies and self-interstitials do not affect the BO defect formation.

In a series of long-term annealing experiments, we discovered that the BO-related defect concentration is not necessarily in equilibrium after sample processing. However, annealing in darkness at temperatures between 200 °C and 300 °C for up to 50 hours establishes the equilibrium. The equilibrium defect concentration was found to decrease with increasing annealing temperature, which supports a recently proposed defect model ($B_iB_sO_i$ model), which attributes the equilibration process to an exchange of a mobile B_i species between two sinks, presumably a B_sO complex and boron nano-precipitates

(B-NPs). From our new experimental results presented in this thesis, we concluded that the binding energy of the B_i atoms to the B_sO_i complex is larger than the binding energy to the NPs. Consequently, the supply of sufficient energy to the system, for example by annealing in darkness, would cause a net transition of B_i atoms from the B-NPs to the B_sO_i complex and hence a degradation of the lifetime.

Lifetime limitations in oxygen-rich Cz-Si free of the BO defect were studied using *n*-type Cz-Si doped with phosphorus. It was observed that Cz-Si materials from different ingots behave very differently if exposed to high-temperature processing due to the temperature dependent nucleation of oxygen precipitates. However, we were able to prevent the nucleation of these precipitates by a short high-temperature process step, referred to as 'tabula rasa' treatment. It was shown here for the first time that this tabula rasa step can be applied to Cz-Si for PV applications. Additionally, it was shown that tabula rasa can be performed in a conventional belt-line furnace, typically used for the metallization of silicon solar cells.

Concerning the permanent deactivation of the BO defect we showed for the first time that the last high-temperature treatment, before the deactivation process is applied, is of utmost importance for the deactivation kinetics. In particular, by applying a rapid thermal annealing (RTA) step in a conventional belt-line furnace, the deactivation can be strongly accelerated. A linear correlation was discovered between the deactivation rate constant and the cooling rate at a critical temperature of 600 °C. That is, the faster a sample is cooled at 600°C, the larger the deactivation rate constant. This result was explained in the framework of the $B_iB_sO_i$ model, which attributes the deactivation to a dissociation of the $B_iB_sO_i$ complex and a subsequent sinking of the free B_i atoms into B-NPs. Combining a fast cooling rate at 600 °C with a permanent deactivation under optimized conditions (applying a temperature of 230 °C and a light intensity of 245 mW/cm^2) we were able to show for the first time, that industrially feasible process times of 5 to 10 s for the complete deactivation process are achievable. These short process times allow the implementation of the deactivation process into industrial solar cell production, for example by the development of belt-line furnaces for this application.
Additionally, in various experiments the claims that the introduction of hydrogen into the silicon is necessary for a successful permanent deactivation could be disproved, excluding defect models involving hydrogen. Nevertheless, hydrogen can have a beneficial impact on the deactivation process if the lifetime in the silicon is generally improved via a hydrogenation of background defects.

We performed a detailed analysis of the lifetime reached after the deactivation process. In the course of this work, very high lifetimes exceeding 1 ms on 1.0 Ω cm material were obtained, significantly exceeding previous results and demonstrating the potential of

B-doped Cz-Si for high-efficiency solar cells. The achieved lifetimes after deactivation were parameterized as a function of the doping concentration and injection level. The injection level dependence is given by a single Shockley-Read-Hall centre, located in the middle of the silicon band gap and featuring a capture cross section ratio of $\sigma_n/\sigma_p = 12$. To study the impact of our new lifetime parameterization on the performance of silicon solar cells, we performed a 2D device simulation. The simulation, based on a state-of-the-art passivated emitter and rear cell (PERC) with homogeneous emitter, revealed that stable conversion efficiencies exceeding 22% are achievable on conventional boron-doped Cz-Si using today's cell technologies and the deactivation process optimized in this work. In particular, implementing a selective emitter and reducing the recombination current densities at the interfaces to the lowest so far reported values, our measured lifetimes would allow conversion efficiencies of up to 23.4%, which was hitherto not believed to be achievable with conventional boron-doped Cz-Si.

We examined the stability of the lifetime after permanent deactivation of the BO defect in detail under various conditions for up to 10000 hours. On a single material ($\rho = 1.0\,\Omega\,\mathrm{cm}$) the stability was tested at room temperature and at a low illumination intensity of $P_{ill} = 10\,\mathrm{mW/cm^2}$ as well as under harsher conditions, i.e. $P_{ill} = 75\,\mathrm{mW/cm^2}$ and at 75 °C. The lifetime was found to degrade only slightly and lifetimes in the range of 1 ms ($\Delta n = 0.1 \times p_0$) are still achieved after 1000 hours of illumination at room temperature (independent of the recovery temperature). The change in the lifetime in general was found to be independent of the applied belt speed during RTA and independent of the surface passivation type. Under the harsher conditions, no degradation was observed, which is highly relevant, as under operating conditions, the solar cell is exposed to similar temperatures.

Stability tests using different base materials revealed a material-dependent long-term behaviour of the lifetime. While some materials showed no change in lifetime on the long-term, decreasing or increasing lifetimes were observed on other materials. We attribute these different behaviours to different material-dependent background defects. To further improve the quality of the Cz-Si material, these background defects have to be better understood and methods to eliminate them have to be developed in the future.

Finally, we examined the stability of a PERC solar cell after permanent deactivation. After the permanent deactivation, the cell featured a conversion efficiency of 20.5%, which degraded over the course of 10000 hours ($P_{ill} = 10\,\mathrm{mW/cm^2}$ at room temperature) by 1.2% relative to 20.2%. Despite this degradation, the efficiency is still much higher than the efficiency without the deactivation process of 19.6%. Hence, the deactivation process leads to an absolute increase of 0.8% in efficiency, making it highly relevant for industrial applications. Additionally, the degradation rate constant obtained from the solar cell degradation is in very good agreement to the results obtained on lifetime samples, which shows that the change of the efficiency is driven by the bulk lifetime.

From the results obtained within this thesis further fundamental questions arise with regard to the deactivation process of the BO defect. While for the deactivation rate constant we discovered the dependence on the cooling rate, our results indicate a base doping dependence in heavily doped materials, which is not yet understood. Additionally, the deactivation rate constant was found to increase with the illumination intensity during the deactivation process suggesting a dependence on the excess carrier concentration. However, the change of the effective defect concentration during the deactivation process can be described by a single exponential decay function although the excess carrier concentration changes about one order of magnitude during the process. Hence, the dependence on the excess carrier concentration is not yet unambiguously understood. Regarding the lifetime reached after the deactivation process, we have observed lifetimes significantly exceeding previous results. However, the high lifetimes are still below the lifetimes observed in defect-lean FZ-Si. Further studies are therefore necessary to identify the reasons for this difference and to clarify whether these limitations are only due to – up to now – unknown background defects, which need to be further studied, or whether for example the recombination at the B-NPs also contributes to these limitations.

Bibliography

[1] B. Burger, K. Kiefer, C. Kost, S. Nold, S. Phillips, R. Preu, J. Rentsch, T. Schlegl, G. Styri-Hipp, G. Willeke, H. Wirth, I. Brucker, A. Häberle, and W. Warmuth. Fraunhofer ISE: Photovoltaic report, updated: 6 June 2016.

[2] M. J. Kerr, P. Campbell, and A. Cuevas. Lifetime and efficiency limits of crystalline silicon solar cells. In *Proceedings 29th IEEE PVSC, New Orleans, LA*, pages 438–441, 2002.

[3] H. Fischer and W. Pschunder. Investigation of photon and thermal induced changes in silicon solar cells. *Proceedings 10th IEEE PVSC, Palo Alto, CA*, page 404, 1974.

[4] A. Herguth, G. Schubert, M. Kaes, and G. Hahn. A new approach to prevent the negative impact of the metastable defect in boron doped Cz silicon solar cells. *Proceedings 32nd IEEE PVSC (4th WCPEC), Waikoloa, USA*, pages 940–943, 2006.

[5] H.C. Theuerer. Method of processing semiconductive materials. *United States Patent, US 3060123 A*, 1962.

[6] J. Czochralski. Ein neues Verfahren zur Messung der Kristallisationsgeschwindigkeit. *Zeitschrift für Physikalische Chemie*, 92:219–221, 1918.

[7] G. K. Teal and Little J. B. Growth of germanium single crystals. *Physical Review*, 81(4):637, 1951.

[8] W. Zulehner. Historical overview of silicon crystal pulling development. *Materials Science and Engineering: B*, 73(1–3):7–15, 2000.

[9] V. V. Voronkov. The mechanism of swirl defects formation in silicon. *Journal of Crystal Growth*, 59(3):625–643, 1982.

[10] W. von Ammon, E. Dornberger, H. Oelkrug, and H. Weidner. The dependence of bulk defects on the axial temperature gradient of silicon crystals during Czochralski growth. *Journal of Crystal Growth*, 151(3):273–277, 1995.

[11] V.V. Voronkov and R. Falster. Vacancy-type microdefect formation in Czochralski silicon. *Journal of Crystal Growth*, 194:76–88, 1998.

[12] A. Borghesi, B. Pivac, A. Sassella, and A. Stella. Oxygen precipitation in silicon. *Journal of Applied Physics*, 77(9):4169–4244, 1995.

[13] M. Miyagi, K. Wada, J. Osaka, and N. Inoue. Effect of oxide precipitates on minority–carrier lifetime in Czochralski–grown silicon. *Applied Physics Letters*, 40 (8):719–721, 1982.

[14] J. M. Hwang and D. K. Schroder. Recombination properties of oxygen–precipitated silicon. *Journal of Applied Physics*, 59(7):2476–2487, 1986.

[15] K. F. Kelton, R. Falster, D. Gambaro, M. Olmo, M. Cornara, and P. F. Wei. Oxygen precipitation in silicon: Experimental studies and theoretical investigations within the classical theory of nucleation. *Journal of Applied Physics*, 85(12): 8097–8111, 1999.

[16] R. Falster, M. Cornara, D. Gambaro, M. Olmo, and M. Pagani. Effect of high temperature pre-anneal on oxygen precipitates nucleation kinetics in Si. *Solid State Phenomena*, 57-58:123–128, 1997.

[17] V. G. Weizer, H. W. Brandhorst, J. D. Broder, R. E. Hart, and J. H. Lamneck. Photon–degradation effects in terrestrial silicon solar cells. *Journal of Applied Physics*, 50(6):4443–4449, 1979.

[18] J. Schmidt, A. G. Aberle, and R. Hezel. Investigation of carrier lifetime instabilities in Cz-grown silicon. *Proceedings 26th IEEE PVSC, Anaheim, CA*, page 13, 1997.

[19] S. W. Glunz, S. Rein, W. Warta, J. Knobloch, and W. Wettling. On the degradation of Cz-silicon solar cells. *Proceedings 2nd WC-PVSEC, Vienna, Austria*, page 1343, 1998.

[20] J. Schmidt and A. Cuevas. Electronic properties of light-induced recombination centers in boron-doped Czochralski silicon. *Journal of Applied Physics*, 86(6):3175, 1999.

[21] S. W. Glunz, S. Rein, and J. Knobloch. Stable Czochralski silicon solar cells using gallium-doped base material. *Proceedings 16th EUPVSEC, Glasgow, UK*, page 1070, 2000.

[22] K. Bothe, J. Schmidt, and R. Hezel. Effective reduction of the metastable defect concentration in boron-doped Czochralski silicon for solar cells. *Proceedings 29th IEEE PVSC, New Orleans, LA*, page 194, 2002.

[23] S. Rein, S. Diez, R. Falster, and S. W. Glunz. Quantitative correlation of the metastable defect in Cz-silicon with different impurities. *Proceedings 3rd WCPEC, Osaka, Japan*, pages 1048–1052, 2003.

[24] J. Schmidt, K. Bothe, and R. Hezel. Structure and transformation of the metastable center in Cz-silicon solar cells. *Proceedings 3rd WCPEC, Osaka, Japan*, pages 2887–2892, 2003.

[25] H. Hashigami and T. Saitoh. Carrier-induced degradation phenomena of carrier lifetime and cell performance in boron-doped Cz-Si. *Proceedings 3rd WCPEC, Osaka, Japan*, 2003.

[26] J. Schmidt and K. Bothe. Structure and transformation of the metastable boron- and oxygen-related defect center in crystalline silicon. *Physical Review B*, 69(2): 024107, 2004.

[27] K. Bothe, R. Sinton, and J. Schmidt. Fundamental boron-oxygen-related carrier lifetime limit in mono- and multicrystalline silicon. *Progress in Photovoltaics: Research and Applications*, 13(4):287–296, 2005.

[28] K. Bothe and J. Schmidt. Electronically activated boron-oxygen-related recombination centers in crystalline silicon. *Journal of Applied Physics*, 99:013701, 2006.

[29] D. W. Palmer, K. Bothe, and J. Schmidt. Kinetics of the electronically stimulated formation of a boron-oxygen complex in crystalline silicon. *Physical Review B*, 76 (3):035210, 2007.

[30] J.C Bourgoin and J.W Corbett. A new mechanism for interstital migration. *Physics Letters A*, 38(2):135–137, 1972.

[31] J. Adey, R. Jones, D. W. Palmer, P. R. Briddon, and S. Öberg. Degradation of boron-doped Czochralski-grown silicon solar cells. *Physical Review Letters*, 93(5): 055504, 2004.

[32] R. Kopecek, J. Arumughan, K. Peter, E. A. Good, J. Libal, M. Acciarri, and S. Binetti. Crystalline Si solar cells from compensated material: Behaviour of light induced degradation. *Proceedings 23rd EUPVSEC, Valencia, Spain*, pages 1855–1858, 2008.

[33] D. Macdonald, F. Rougieux, A. Cuevas, B. Lim, J. Schmidt, M. Di Sabatino, and L. J. Geerligs. Light-induced boron-oxygen defect generation in compensated p-type Czochralski silicon. *Journal of Applied Physics*, 105:093704, 2009.

[34] V. V. Voronkov and R. Falster. Latent complexes of interstitial boron and oxygen dimers as a reason for degradation of silicon-based solar cells. *Journal of Applied Physics*, 107(5):053509, 2010.

[35] A. Herguth, G. Schubert, M. Kaes, and G. Hahn. Further investigations on the avoidance of boron-oxygen related degradation by means of regeneration. *Proceedings 22nd EUPVSEC, Milan, Italy*, pages 893–896, 2007.

[36] B. Lim, K. Bothe, and J. Schmidt. Deactivation of the boron-oxygen recombination center in silicon by illumination at elevated temperature. *physica status solidi (RRL) - Rapid Research Letters*, 2(3):93–95, 2008.

[37] K. A. Münzer. Hydrogenated silicon nitride for regeneration of light induced degradation. *Proceedings 24th EUPVSEC, Hamburg, Germany*, pages 1558–1561, 2009.

[38] B. Lim, A. Liu, D. Macdonald, K. Bothe, and J. Schmidt. Impact of dopant compensation on the deactivation of boron-oxygen recombination centers in crystalline silicon. *Applied Physics Letters*, 95:232109, 2009.

[39] B. Lim, F. Rougieux, D. Macdonald, K. Bothe, and J. Schmidt. Generation and annihilation of boron-oxygen-related recombination centers in compensated p- and n-type silicon. *Journal of Applied Physics*, 108(10):103722, 2010.

[40] J. Schmidt, K. Bothe, and R. Hezel. Formation and annihilation of the metastable defect in boron-doped czochralski silicon. In *Proceedings 29th IEEE PVSC, New Orleans, LA,*, pages 178–181, 2002.

[41] U. Gösele and T. Y. Tan. Oxygen diffusion and thermal donor formation in silicon. *Applied Physics A*, 28(2):79–92, 1982.

[42] B. Lim. Boron-oxygen-related recombination centers in crystalline silicon and the effects of dopant-compensation. *PhD thesis, University of Hanover*, 2011.

[43] L. I. Murin, T. Hallberg, V. P. Markevich, and J. L. Lindström. Experimental evidence of the oxygen dimer in silicon. *Physical Review Letters*, 80(1):93–96, 1998.

[44] D. Macdonald, A. Liu, A. Cuevas, B. Lim, and J. Schmidt. The impact of dopant compensation on the boron-oxygen defect in p- and n-type crystalline silicon. *physica status solidi (a)*, 208(3):559–563, 2011.

[45] B. Lim, K. Bothe, and J. Schmidt. Impact of oxygen on the permanent deactivation of boron-oxygen-related recombination centers in crystalline silicon. *Journal of Applied Physics*, 107:123707, 2010.

[46] M. Forster, E. Fourmond, F. E. Rougieux, A. Cuevas, R. Gotoh, K. Fujiwara, S. Uda, and M. Lemiti. Boron-oxygen defect in Czochralski-silicon co-doped with gallium and boron. *Applied Physics Letters*, 100(4):042110, 2012.

[47] V. V. Voronkov and R. Falster. Light-induced boron-oxygen recombination centres in silicon: Understanding their formation and elimination. *Solid State Phenomena (SSP)*, 205-206:3–14, 2013.

[48] S. Wilking, A. Herguth, and G. Hahn. Influence of hydrogen on the regeneration of boron-oxygen related defects in crystalline silicon. *Journal of Applied Physics*, 113(19):194503, 2013.

[49] S. Wilking, C. Beckh, S. Ebert, A. Herguth, and G. Hahn. Influence of bound hydrogen states on BO-regeneration kinetics and consequences for high-speed regeneration processes. *Solar Energy Materials and Solar Cells*, 131:2–8, 2014.

[50] S. J. Pearton, J. W. Corbett, and T. S. Shi. Hydrogen in crystalline semiconductors. *Applied Physics A*, 43(3):153–195, 1987.

[51] T. Zundel and J. Weber. Boron reactivation kinetics in hydrogenated silicon after annealing in the dark or under illumination. *Phys. Rev. B*, 43(5):4361–4372, 1991.

[52] Y. L. Huang, Y. Ma, R. Job, and A. G. Ulyashin. Hydrogen diffusion at moderate temperatures in p-type Czochralski silicon. *Journal of Applied Physics*, 96(12): 7080–7086, 2004.

[53] D. Mathiot. Modeling of hydrogen diffusion in n- and p-type silicon. *Physical Review B*, 40(8):5867–5870, 1989.

[54] V. V. Voronkov and R. Falster. Permanent deactivation of boron–oxygen recombination centres in silicon. *physica status solidi (b)*, 253(9):1721–1728, 2016.

[55] T. Trupke, M. A. Green, P. Würfel, P. P. Altermatt, A. Wang, J. Zhao, and R. Corkish. Temperature dependence of the radiative recombination coefficient of intrinsic crystalline silicon. *Journal of Applied Physics*, 94(8):4930–4937, 2003.

[56] P. P. Altermatt, F. Geelhaar, T. Trupke, X. Dai, A. Neisser, and E. Daub. Injection dependence of spontaneous radiative recombination in crystalline silicon: Experimental verification and theoretical analysis. *Applied Physics Letters*, 88 (26), 2006.

[57] A. Hangleiter and R. Häcker. Enhancement of band-to-band Auger recombination by electron-hole correlations. *Physical Review Letters*, 65(2):215–218, 1990.

[58] P. P. Altermatt, J. Schmidt, G. Heiser, and A. G. Aberle. Assessment and parameterisation of Coulomb-enhanced Auger recombination coefficients in lowly injected crystalline silicon. *Journal of Applied Physics*, 82(10):4938–4944, 1997.

[59] J. Schmidt, M. Kerr, and P. P. Altermatt. Coulomb-enhanced Auger recombination in crystalline silicon at intermediate and high injection densities. *Journal of Applied Physics*, 88(3):1494–1497, 2000.

[60] A. Richter, F. Werner, A. Cuevas, J. Schmidt, and S. W. Glunz. Improved parametrization of Auger recombination in silicon. *Energy Procedia*, 27(0):88–94, 2012.

[61] W. Shockley and W. T. Read. Statistics of the recombinations of holes and electrons. *Physical Review*, 87(5):835–842, 1952.

[62] R. N. Hall. Electron-hole recombination in germanium. *Physical Review*, 87(2): 387, 1952.

[63] J. D. Murphy, K. Bothe, R. Krain, V. V. Voronkov, and R. J. Falster. Parameterisation of injection-dependent lifetime measurements in semiconductors in terms of Shockley-Read-Hall statistics: An application to oxide precipitates in silicon. *Journal of Applied Physics*, 111(11):113709, 2012.

[64] A. B. Sproul. Dimensionless solution of the equation describing the effect of surface recombination on carrier decay in semiconductors. *Journal of Applied Physics*, 76 (5):2851–2854, 1994.

[65] K. Bothe. Oxygen-related trapping and recombination centres in boron-doped crystalline silicon. *PhD thesis, University of Hanover*, 2006.

[66] P. P. Altermatt, J. Schmidt, M. Kerr, G. Heiser, and A. G. Aberle. Exciton-enhanced Auger recombination in crystalline silicon under intermediate and high injection conditions. *Proceedings 16th EUPVSEC, Glasgow, UK*, pages 243–246, 2000.

[67] H. Nagel, C. Berge, and A. G. Aberle. Generalized analysis of quasi-steady-state and quasi-transient measurements of carrier lifetimes in semiconductors. *Journal of Applied Physics*, 86(11):6218, 1999.

[68] K. R. McIntosh and R. A. Sinton. Uncertainty in photoconductance lifetime measurements that use an inductive-coil detector. *Proceedings 23rd EUPVSEC, Valencia, Spain*, pages 77–82, 2008.

[69] B. Lim, K. Bothe, and J. Schmidt. Accelerated deactivation of the boron-oxygen-related recombination centre in crystalline silicon. *Semiconductor Science and Technology*, 26(9):095009, 2011.

[70] S. Herlufsen, J. Schmidt, D. Hinken, K. Bothe, and R. Brendel. Photoconductance-calibrated photoluminescence lifetime imaging of crystalline silicon. *physica status solidi (RRL) – Rapid Research Letters*, 2(6):245–247, 2008.

[71] S. Herlufsen, D. Hinken, M. Offer, J. Schmidt, and K. Bothe. Validity of calibrated photoluminescence lifetime measurements of crystalline silicon wafers for arbitrary lifetime and injection ranges. *IEEE Journal of Photovoltaics*, 3(1):381–386, 2013.

[72] A. Baghdadi, W. M. Bullis, M. C. Croarkin, Yue-zhen Li, R. I. Scace, R. W. Series, P. Stallhofer, and M. Watanabe. Interlaboratory determination of the calibration factor for the measurement of the interstitial oxygen content of silicon by infrared absorption. *Journal of The Electrochemical Society*, 136(7):2015–2024, 1989.

[73] M. Hasebe, Y. Takeoka, S. Shinoyama, and S. Naito. Formation process of stacking faults with ringlike distribution in Cz-Si wafers. *Japanese Journal of Applied Physics*, 28(11A):L1999, 1989.

[74] K. Bothe, J. Schmidt, and R. Hezel. Understanding and reducing the boron-oxygen-related performance degradation in Czochralski silicon solar cells. *Solid State Phenomena*, 95:223–228, 2003.

[75] V. V. Voronkov and R. Falster. Grown-in microdefects, residual vacancies and oxygen precipitation bands in Czochralski silicon. *Journal of Crystal Growth*, 204 (4):462–474, 1999.

[76] P. J. Cousins, D. D. Smith, H. C. Luan, J. Manning, T. D. Dennis, A. Waldhauer, K. E. Wilson, G. Harley, and W. P. Mulligan. Generation 3: Improved performance at lower cost. *Proceedings 35th IEEE PVSC, Honolulu, HI*, pages 275–278, 2010.

[77] W. Bergholz, M. J. Binns, G. R. Booker, J. C. Hutchison, S. H. Kinder, S. Messoloras, R. C. Newman, R. J. Stewart, and J. G. Wilkes. A study of oxygen precipitation in silicon using high-resolution transmission electron microscopy, small-angle neutron scattering and infrared absorption. *Philosophical Magazine Part B*, 59(5):499–522, 1989.

[78] J. Schmidt, B. Veith, and R. Brendel. Effective surface passivation of crystalline silicon using ultrathin Al_2O_3 films and Al_2O_3/SiN_x stacks. *physica status solidi (RRL) - Rapid Research Letters*, 3(9):287–289, 2009.

[79] F. Werner, B. Veith, V. Tiba, P. Poodt, F. Roozeboom, R. Brendel, and J. Schmidt. Very low surface recombination velocities on p- and n-type c-Si by ultrafast spatial atomic layer deposition of aluminum oxide. *Applied Physics Letters*, 97(16):162103, 2010.

[80] B. J. Hallam, P. G. Hamer, S. R. Wenham, M. D. Abbott, A. Sugianto, A. M. Wenham, C. E. Chan, G. Xu, J. Kraiem, J. Degoulange, and R. Einhaus. Advanced bulk defect passivation for silicon solar cells. *IEEE Journal of Photovoltaics*, 4(1): 88–95, 2014.

[81] A. Richter, S. W. Glunz, F. Werner, J. Schmidt, and A. Cuevas. Improved quantitative description of Auger recombination in crystalline silicon. *Physical Review B*, 86(16):165202, 2012.

[82] V. V. Voronkov, R. Falster, K. Bothe, and B. Lim. Light-induced lifetime degradation in boron-doped Czochralski silicon: Are oxygen dimers involved? *Energy Procedia*, 38:636–641, 2013.

[83] V. V. Voronkov, R. Falster, B. Lim, and J. Schmidt. Permanent recovery of electron lifetime in pre-annealed silicon samples: A model based on Ostwald ripening. *Journal of Applied Physics*, 112(11):113717, 2012.

[84] A. Herguth and G. Hahn. Kinetics of the boron-oxygen related defect in theory and experiment. *Journal of Applied Physics*, (108):114509, 2010.

[85] B. Lenkeit. Elektronische und strukturelle Eigenschaften von Plasma-Siliziumnitrid zur Oberflächenpassivierung von siebgedruckten, bifacialen Silizium-Solarzellen. *PhD thesis, University of Hanover*, 2002.

[86] B. Hoex, J. Schmidt, P. Pohl, M. C. M. van de Sanden, and W. M. M. Kessels. Silicon surface passivation by atomic layer deposited Al_2O_3. *Journal of Applied Physics*, 104(4):044903, 2008.

[87] K. R. McIntosh and S. C. Baker-Finch. Opal 2: Rapid optical simulation of silicon solar cells. *Proceedings 38th IEEE PVSC, Austin, Texas*, pages 265–271, 2012.

[88] S. Kleekajai, F. Jiang, Michael Stavola, V. Yelundur, K. Nakayashiki, A. Rohatgi, G. Hahn, S. Seren, and J. Kalejs. Concentration and penetration depth of H introduced into crystalline Si by hydrogenation methods used to fabricate solar cells. *Journal of Applied Physics*, 100(9):093517, 2006.

[89] A. Mogro-Campero. Drastic changes in the electrical resistance of gold-doped silicon produced by a hydrogen plasma. *Journal of The Electrochemical Society*, 132(8):2006, 1985.

[90] R. C. Newman, J. H. Tucker, A. R. Brown, and S. A. McQuaid. Hydrogen diffusion and the catalysis of enhanced oxygen diffusion in silicon at temperatures below 500 °C. *Journal of Applied Physics*, 70(6):3061, 1991.

[91] D. Zielke. Suppressing loss channels in the bulk and at the surface of crystalline silicon solar cells. *PhD thesis, University of Hanover*, 2016.

[92] J. Schmidt, V. Titova, and D. Zielke. Organic-silicon heterojunction solar cells: Open-circuit voltage potential and stability. *Applied Physics Letters*, 103(18): 183901, 2013.

[93] J. Schmidt, B. Lim, D. Walter, K. Bothe, S. Gatz, T. Dullweber, and Pietro P. Altermatt. Impurity-related limitations of next-generation industrial silicon solar cells. *IEEE Journal of Photovoltaics*, 3(1):114–118, 2013.

[94] A. Fell. A free and fast three-dimensional/two-dimensional solar cell simulator featuring conductive boundary and quasi-neutrality approximations. *IEEE Transactions on Electron Devices*, 60(2):733–738, 2013.

[95] R. Brendel. Modeling solar cells with the dopant-diffused layers treated as conductive boundaries. *Progress in Photovoltaics: Research and Applications*, 20(1): 31–43, 2012.

[96] T. Dullweber, S. Gatz, H. Hannebauer, T. Falcon, R. Hesse, J. Schmidt, and R. Brendel. Towards 20% efficient large-area screen-printed rear-passivated silicon solar cells. *Progress in Photovoltaics: Research and Applications*, 20(6):630–638, 2012.

[97] H. Hannebauer, T. Dullweber, U. Baumann, T. Falcon, and R. Brendel. 21.2%-efficient fineline-printed PERC solar cell with 5 busbar front grid. *physica status solidi (RRL) - Rapid Research Letters*, 8(8):675–679, 2014.

[98] B. Lim, T. Brendemühl, M. Berger, A. Christ, and T. Dullweber. n-PERT back junction solar cells: an option for the next industrial technology generation? *Proceedings 29th EUPVSEC, Amsterdam, the Netherlands*, pages 661–665, 2014.

[99] R. Brendel, S. Dreissigacker, N.-P. Harder, and P. P. Altermatt. Theory of analyzing free energy losses in solar cells. *Applied Physics Letters*, 93(17):173503, 2008.

[100] T. Dullweber, H. Hannebauer, S. Dorn, S. Schimanke, A. Merkle, C. Hampe, and R. Brendel. Emitter saturation current densities of 22 fA/cm^2 applied to industrial perc solar cells approaching 22% conversion efficiency. *Progress in Photovoltaics: Research and Applications*, pages n/a–n/a, 2016.

[101] H. Hannebauer, M. Sommerfeld, J. Müller, T. Dullweber, and R. Brendel. Analysis of the emitter saturation current density of industrial type silver screen-printed front contacts. *Proceedings 27th EUPVSEC, Frankfurt, Germany*, pages 1360–1363, 2012.

[102] H. Hannebauer, S. Schimanke, T. Falcon, P. P. Altermatt, and T. Dullweber. Optimized stencil print for low ag paste consumption and high conversion efficiencies. *Energy Procedia*, 67:108–115, 2015.

[103] C. Kranz, B. Lim, U. Baumann, and T. Dullweber. Determination of the contact resistivity of screen-printed al contacts formed by laser contact opening. *Energy Procedia*, 67:64–69, 2015.

[104] C. Kranz, S. Wyczanowski, S. Dorn, K. Weise, C. Klein, K. Bothe, T. Dullweber, and R. Brendel. Impact of the rear surface roughness on industrial-type PERC solar cells. *Proceedings 27th EUPVSEC, Frankfurt, Germany*, pages 557–560, 2012.

[105] A. W. Blakers, A. Wang, A. M. Milne, J. Zhao, and M. A. Green. 22.8% efficient silicon solar cell. *Applied Physics Letters*, 55(13):1363, 1989.

[106] S. Wilking, J. Engelhart, S. Ebert, C. Beckh, A. Herguth, and G. Hahn. High speed regeneration of BO-defects: Improving long-term solar cell performance within seconds. *Proceedings 29th EUPVSEC, Amsterdam, the Netherlands*, pages 366–372, 2014.

[107] J. Schmidt, A. Cuevas, S. Rein, and S. W. Glunz. Impact of light-induced defect centers on the current-voltage characteristics of Czochralski silicon solar cells. *Progress in Photovoltaics: Research and Applications*, 9(4):249–255, 2001.

[108] D. A. Clugston and P. A. Basore. PC1D version 5: 32-bit solar cell modelling on personal computers. *Proceedings 26th IEEE PVSC, Anaheim, CA*, pages 207–210, 1997.

[109] R. A. Sinton and A. Cuevas. Contactless determination of current–voltage characteristics and minority-carrier lifetimes in semiconductors from quasi-steady-state photoconductance data. *Applied Physics Letters*, 69(17):2510, 1996.

[110] J. Schmidt, M. Kerr, and A. Cuevas. Surface passivation of silicon solar cells using plasma-enhanced chemical-vapour-deposited SiN films and thin thermal SiO_2 /plasma SiN stacks. *Semiconductor Science and Technology*, 16(3):164–170, 2001.

List of Publications

Publications arising from the work in this thesis:

Peer-reviewed journal papers

1. J. Schmidt, B. Lim, D. Walter, K. Bothe, S. Gatz, T. Dullweber and P. Altermatt: *Impurity-related limitations of next-generation industrial silicon solar cells.* IEEE Journal of Photovoltaics **3** 114 (2013)
2. D. C. Walter, B. Lim, K. Bothe, V. V. Voronkov, R. Falster and J. Schmidt: *Effect of rapid thermal annealing on recombination centers in boron-doped Czochralski-grown silicon.* Journal of Applied Physics **104** 042111 (2014)
3. D. C. Walter, B. Lim, K. Bothe, R. Falster, V. V. Voronkov and J. Schmidt: *Lifetimes exceeding 1 ms in 1-Ω cm boron-doped Cz-silicon.* Solar Energy Materials and Solar Cells **131** 51 (2014)
4. D. C. Walter, B. Lim and J. Schmidt: *Realistic efficiency potential of next-generation industrial Czochralski-grown silicon solar cells after deactivation of the boron–oxygen-related defect center.* Progress in Photovoltaics: Research and Applications **24** 920 (2016)
5. D. C. Walter and J. Schmidt: *Impact of hydrogen on the permanent deactivation of the boron-oxygen-related recombination center in crystalline silicon.* Solar Energy Materials and Solar Cells *(accepted)*

Conference Proceedings

1. D. Walter, B. Lim, K. Bothe, R. Falster, V. Voronkov and J. Schmidt: *Impact of crystal growth on boron-oxygen defect formation.* Proceedings 27th European Photovoltaic Solar Energy Conference, Frankfurt, Germany, p. 775 (2012)

2. D. C. Walter, B. Lim, R. Falster, J. Binns and J. Schmidt: *Understanding lifetime degradation in Czochralski-grown n-type silicon after high temperature processing.* Proceedings 28th European Photovoltaic Solar Energy Conference, Paris, France, p. 699 (2013)
3. D. C. Walter, B. Lim, V. V. Voronkov, R. Falster and J. Schmidt: *Investigation of the lifetime stability after regeneration in boron-doped Cz silicon.* Proceedings 29th European Photovoltaic Solar Energy Conference, Amsterdam, the Netherlands, p. 555 (2014)
4. D. C. Walter, T. Pernau and J. Schmidt: *Ultrafast lifetime regeneration in an industrial belt-line furnace applying intense illumination at elevated temperatures.* Proceedings 32nd European Photovoltaic Solar Energy Conference, Munich, Germany, p. 469 (2016)

List of Awards

Received awards for results obtained in this thesis:

1. SiliconPV Award 2014
   For the contribution “Lifetimes exceeding 1 ms in 1-Ω cm boron-doped Cz-silicon.”
2. SiliconPV Award 2016
   For the contribution “Impact of hydrogen on the permanent deactivation of the boron-oxygen-related recombination center in crystalline silicon.”
3. EU PVSEC Student Award in the thematic area “Wafer-Based Silicon Solar Cell and Materials Technology” 2016
   For the presentation of “Ultrafast lifetime regeneration in an industrial belt-line furnace applying intense illumination at elevated temperatures.”

List of Figures

List of Tables

Abbreviations

B-NP	boron nano-precipitate
BSG	borosilicate glass
CAGR	compound annal growth rate
CCD	charge-coupled device
CVD	chemical vapour deposition
Cz-Si	Czochralski-grown silicon
e/h	electron / hole
FF	fill factor
FZ-Si	float-zone silicon
FTIR	Fourier transform infrared spectroscopy
FELA	free energy loss analysis
IC	integrated circuit
IDLS	injection-dependent lifetime spectroscopy
ISE	Fraunhofer Institut für solare Energiesysteme
ISFH	Institut für Solarenergieforschung Hameln
LID	light-induced degradation
LC	latent centre
OISF	oxygen induced stacking faults
PCD	photoconductance decay
PC-PLI	photoconductance-calibrated photoluminescence imaging
PECVD	plasma-enhanced chemical vapour deposition
PEDOT:PSS	poly(3,4-ethylenedioxythiophene):poly(styrenesulfonate)
PERC	passivated emitter and rear cell
PL	photoluminescence
plasma-ALD	plasma-assisted atomic layer deposition

PSG	phosphosilicate glass
PV	photovoltaic
QSSPC	quasi-steady-state photoconductance decay
RCA	Radio Corporation of America (clean)
RTA	rapid thermal annealing
rf	radio frequency
Si-PV	silicon-wafer-based PV
SRH	Shockley, Read and Hall
SRV	surface recombination velocity
TD	thermal donor
thermal-ALD	thermal atomic layer deposition

Symbols

Symbol	**Name**
γ	rate constant
Δn	excess carrier density
Δn_{avg}	average excess carrier density
$\Delta\sigma$	photoconductance
η	conversion efficiency
η_i	injection level
ϑ	temperature [°C]
ϑ_n	nucleation temperature
ϑ_{Peak}	peak temperature
ϑ_{recov}	recovery temperature
ϑ_{stab}	stability temperature
λ	wavelength
ξ	critical value for v/i-transition
ρ	resistivity
ρ_{n^+}, ρ_{p^+}	n^+ / p^+ sheet resistance
σ	conductance
σ_0	conductance in darkness
σ_n, σ_p	capture cross section of electrons / holes
τ	lifetime
τ_0	lifetime after complete BO defect annihilation
τ_{0p}	lifetime after permanent recovery
τ_{Auger}	lifetime of Auger recombination
τ_b	bulk lifetime
τ_d	lifetime after complete BO defect activation

τ_{eff}	effective lifetime
τ_{int}	intrinsic lifetime
τ_{n0}, τ_{p0}	capture time constant of electrons / holes
τ_{rad}	lifetime of radiative recombination
τ_{SRH}	lifetime of SRH recombination
Φ	photon flux
B	radiative recombination coefficient
B_{low}	radiative recombination coefficient at 300 K
B_{rel}	radiative recombination coefficient pre-factor: $B = B_{rel} \times B_{low}$
C	cluster concentration
C_n,C_p	Auger recombination coefficients for electrons / holes
C_{sol}	solubility
D	diffusion constant of excess carriers
D_i	diffusivity of interstitial boron
E_a	activation energy
E_b	binding energy
E_c	energy of the conduction band edge
E_g	silicon band gap
E_i	dissolution energy
E_t	energy of the recombination centre
E_v	energy of the valence band edge
G	generation rate
G_{th}	thermal generation rate
I_{PL}	intensity of the photoluminescence signal
I_{sc}	short-circuit current
J	current density
J_0	saturation current density
$J_{0,cont}$, $J_{0,met}$	saturation current density of contacted area
$J_{0,pass}$	saturation current density of passivated area
J_{sc}	short-circuit current density
k_b	Boltzmann constant
K^*	dissociation constant

n	electron concentration
n_0	electron concentration in darkness
n_1, p_1	SRH-densities
N_A	acceptor concentration
N_c, N_v	effective density of states in conductance/valence band
N_D	donator concentration
$N^*_{d,eq}$	maximum effective defect concentration in equilibrium
$N^*_{d,NORM}$	normalized maximum effective defect concentration
n_i	intrinsic carrier concentration
n_l	local ideality factor
N_p	density of B-NPs
n_r	refractive index
N_t	trap density
N^*_t	effective defect concentration
$N^*_{V_{oc}}$	effective defect concentration calculated from V_{oc} values
p	hole concentration
P	power
p_0	hole concentration in darkness
p_{front}, p_{rear}	front / rear contact width
$P_{ill,stab}$	illumination intensity during stability tests
P_{ill}	illumination intensity
q	cooling rate
q_e	elementary charge
r	cluster size
r_c	critical cluster size
R_{c,n^+}, R_{c,p^+}	contact resistance n^+ / p^+-region
R_{de}	defect deactivation rate constant
$R_{f,808\,\mathrm{nm}}$	reflectivity at 808 nm wavelength
R_{gen}	defect generation rate constant
R_p	radius of B-BPs
$R_{s,finger}$	series resistance of the metal finger
S	surface recombination velocity
t	time

T	absolute temperature [K]
U	net recombination rate
U_{Auger}	Auger net recombination rate
U_{int}	intrinsic net recombination rate
U_{rad}	radiative net recombination rate
U_{SRH}	net recombination rate according to SRH-theory
U_{tot}	total recombination rate
V	growth rate
v_{belt}	belt speed
V_{oc}	open-circuit voltage
v_{th}	thermal velocity
W	thickness
x_{n^+}, x_{p^+}	junction depth n^+ / p^+ diffused-region

Danksagung

Abschließend möchte ich mich bei allen bedanken, die zum Gelingen dieser Arbeit beigetragen haben:

Prof. Dr. Rolf Brendel für die Möglichkeit diese Dissertationsschrift am ISFH anzufertigen,

Prof. Dr. Jan Schmidt für die sehr gute und intensive wissenschaftliche Betreuung sowie die überaus lehrreichen Diskussionen und Hilfe beim Erstellen wissenschaftlicher Publikationen,

Prof. Dr. Herbert Pfnür und *Prof. Dr. Daniel Macdonald* für die bereitwillige Übernahme der Korreferate sowie

Prof. Dr. Holger Frahm für die Übernahme des Vorsitzes der Promotionskommission.

Ein besonderer Dank gilt außerdem *Dr. Bianca Lim* für unzählige, hilfreiche Diskussionen und Anregungen, sowohl für die Anfertigung von Veröffentlichungen als auch für das experimentelle Arbeiten.

Ebenso möchte ich mich bei *Dr. Vladimir Voronkov* und *Dr. Robert Falster* für den regen Ideenaustausch und die große Begeisterung für die experimentellen Ergebnisse bedanken.

Außerdem möchte ich mich bei allen Kolleginnen und Kollegen am ISFH bedanken, insbesondere der Gruppe “Materialforschung”, für die außergewöhnlichen und kollegialen Arbeitsbedingungen und für die Unterstützung beim experimentellen Arbeiten.

Nicht zuletzt gilt in besonderer Dank meiner Familie, ohne deren große Unterstützung bereits das Physikstudium und nun auch das Erstellen dieser Arbeit um einiges schwerer gefallen wäre.

Curriculum vitae

Persönliche Daten

Name	Dominic Christof Walter
Anschrift	Reherweg 137, 31787 Hameln
Geburtsdatum	29.12.1983
Nationalität	deutsch

Schulbildung

August 1990 - Juli 1994	Grundschule Neuenburg am Rhein
August 1994 - Juni 2003	Markgräfler Gymnasium Müllheim Abschluss der allgemeinen Hochschulreife

Freiwilliges soziales Jahr

Juli 2003 - September 2004	Voluntary Action Leicester, UK

Universitätsausbildung

Oktober 2004 - Januar 2011	**Albert-Ludwigs-Universität Freiburg** Studium der Physik

Anstellung

November 2008 - Juni 2009 und **August 2009 - Juli 2011**	**Fraunhofer Institut für solare Energiesysteme (ISE)** wissenschaftliche Hilfskraft
seit Oktober 2011	**Institut für Solarenergieforschung Hameln (ISFH)** wissenschaftlicher Mitarbeiter